UNIVERSITY OF SÃO PAULO

SÃO CARLOS SCHOOL OF ENGINEERING

JOAQUIM MANOEL JUSTINO NETTO

# Development of an innovative additive manufacturing equipment containing a co-rotating twin screw extrusion unit

São Carlos

2022

JOAQUIM MANOEL JUSTINO NETTO

# Development of an innovative additive manufacturing equipment containing a co-rotating twin screw extrusion unit

Corrected thesis

Thesis presented to the graduate program in Mechanical Engineering at the University of São Paulo, to obtain the title of Doctor of Science. Research area: Design, Materials and Manufacturing.

Supervisor: Prof. Dr. Zilda de Castro Silveira

Co-supervisor: Prof. Dr. Alessandra de Almeida Lucas

São Carlos

2022

Ficha catalográfica elaborada pela Biblioteca Prof. Dr. Sérgio Rodrigues Fontes da EESC/USP com os dados inseridos pelo(a) autor(a).

Justino-Netto, Joaquim Manoel
J96d Development of an innovative additive manufacturing equipment containing a co-rotating twin screw extrusion unit / Joaquim Manoel Justino-Netto; orientadora Zilda de Castro Silveira; coorientadora Alessandra de Almeida Lucas. São Carlos, 2022.

Tese (Doutorado) - Programa de Pós-Graduação em Engenharia Mecânica e Área de Concentração em Projeto, Materiais e Manufatura -- Escola de Engenharia de São Carlos da Universidade de São Paulo, 2022.

1. MEX. 2. Customized design. 3. Fused pellet fabrication. 4. Polymer blends. 5. Prototype. I. Título.

Eduardo Graziosi Silva - CRB - 8/8907

# FOLHA DE JULGAMENTO

Candidato: Engenheiro **JOAQUIM MANOEL JUSTINO NETTO.**

Título da tese: "Desenvolvimento de um sistema de manufatura aditiva contendo extrusora dupla rosca corrotativa".

Data da defesa: 28/11/2022.

| **Comissão Julgadora** | **Resultado** |
|---|---|
| Profa. Dra. **Zilda de Castro Silveira** **(Orientadora)** (Escola de Engenharia de São Carlos – EESC/USP) | Aprovado |
| Prof. Dr. **Franco Giuseppe Dedini** (Universidade Estadual de Campinas/UNICAMP) | Aprovado |
| Prof. Dr. **José António Colaço Gomes Covas** (Universidade do Minho/UMINHO) | Aprovado |
| Prof. Dr. **Fernando Jorge Lino Alves** (Universidade do Porto/UP) | Aprovado |
| Prof. Dr. **Marcos Antonio Sabino Gutierrez** (Universidad Simon Bolivar/USB - Venezuela) | Aprovado |

Coordenador do Programa de Pós-Graduação em Engenharia Mecânica:
Prof. Associado **Adriano Almeida Gonçalves Siqueira**

Presidente da Comissão de Pós-Graduação:
Prof. Titular **Murilo Araujo Romero**

**DEDICATION**

To my mother, Tereza, and my father, Aparecido (*in memoriam*).

You are forever in me.

## ACKNOWLEDGEMENTS

To my supervisor, Prof. Dr. Zilda de Castro Silveira for always believing in me even in the most troublesome times. To Prof. Dr. José António Covas (DEP, UMinho) and to Prof. Dr. Jorge Lino Alves (FEUP, UPorto) for the valuable contributions during the development of this work and for having welcomed me so well in Portugal.

To Prof. Dr. Marcelo Aparecido Chinelatto and the technicians Ricardo Gomes and Pedro Di Lorenzo from the Department of Materials Engineering (EESC, USP) for their all-time support whenever we needed it. To Prof. Dr. Alessandra de Almeida Lucas (DEMa, UFSCar), the technicians Lourival Varanda, Osvaldo de Souza Jr, Osvaldo Correa, and the research colleagues Gustavo Duarte and Andre Grando Santos. I am grateful for everything I learned from you.

To Dr. André L. J. Munhoz, Instituto Nacional de C&T em Biofabricação - Unicamp, and Prof. Dr. Julian Ávila, Faculdade de Engenharia Eletrônica e de Telecomunicações e Engenharia Aeronáutica - UNESP, for the assistance in manufacturing the rigid couplings. To the technician Sidney Rigo Jr., from the CDCC-USP, and for Larissa Lea da Silva and Vinicius Soares Steffen, from BASF, for having provided raw materials to the processing studies.

To the research colleagues Artur, Ismael, Frezzatto, Henrique, Leonardo and Davila for the help with materials acquisition and for the daily companionship. To the colleagues from Portugal Miguel, Bruno, Rita, Ana, Paulo, and Felipe. To the undergrad students Matheus Ito, for the initial support with the electronics, and Amir Sarout for being my right-hand in the final stretch of this project.

To the coordinator and secretariat of the postgraduate program PPGSEM (EESC, USP). To all professors from the São Carlos School of Engineering (USP), who were always available throughout the past twelve years and certainly made a difference in my life.

To the National Council for Scientific and Technological Development (CNPq) for the doctoral fellowship granted (process number 142348/2018-0) and to the Coordination for the Improvement of Higher Education Personnel (CAPES) for the sandwich fellowship granted (process number 88887.468329/2019-00).

To my family and friends for the unconditional support.

“*Et cum videris materiam tuam denigrari, gaude: quia principium est operis*”

Rosarium Philosophorum

## RESUMO

JUSTINO NETTO, J. M. **Desenvolvimento de um equipamento para manufatua aditiva com cabeçote de extrusão dupla rosca corrotativa**. 2022. 165p. Tese (Doutorado em Engenharia Mecânica) – Escola de Engenharia de São Carlos, Universidade de São Paulo, São Carlos, 2022.

Este trabalho aparesenta o desenvolvimento de uma impressora 3D baseada em extrusora dupla rosca corrotativa. A manufatura aditiva por extrusão (MAE) tem sido tradicionalmente implementada por impressoras 3D que utilizam filamentos com oferta comercial limitada de materiais. Desde os anos 2000, novas tecnologias MAE que aceitam material em pó ou *pellets* têm sido propostas. A solução típica, baseada em extrusão rosca simples, expande as opções de materiais aplicáveis, permite reduzir custos de impressão e aumentar as taxas de deposição, mas apresenta pouca flexibilidade de processo e baixa capacidade de mistura. O novo equipamento combina uma mini-extrusora dupla rosca corrotativa modular operada em regime de semipreenchimento com uma plataforma Cartesiana, e aceita material em pó ou micro-*pellets*. Similar às extrusoras dupla rosca industriais, a vazão e rotação das roscas podem ser definidas independentemente e sua capacidade de mistura pode ser ajustada de acordo com requisitos da manufatura. A MAE assistida por rosca foi investigada em uma revisão sistemática, revelando importantes vantagens e limitações de projeto, assim como o fluxo de desenvolvimento da tecnologia. O novo equipamento foi desenvolvido em três iterações, partindo da geometria das roscas até a simulação do processo de extrusão para verificar se o ambiente termomecânico apropriado seria criado pela mini-extrusora. Um protótipo funcional foi construído ao final da terceira iteração. Testes de extrusão foram realizados em diferentes condições de operação, utilizando polipropileno e uma blenda de polipropileno/poliestireno 90/10 (% em massa). Duas configurações de rosca foram testadas, com e sem elementos de malaxagem, para avaliar as características de fluxo e desempenho de mistura. Os resultados mostraram que os elementos de mistura determinam o início da fusão, os tempos médios de residência, e o nível de cisalhamento que, por sua vez, tem efeito sobre a qualidade da mistura. A configuração e velocidade de rotação das roscas não afetam a vazão, que depende apenas da taxa de alimentação. Testes preliminares de deposição foram realizados para determinar os parâmetros de impressão 3D. Um corpo-de-prova padrão, um *scaffold e* uma caixa multicolorida foram adequadamente impressos, validando o novo equipamento. As propriedades mecânicas dos corpos-de-prova apresentaram valores em conformidade com a literatura. Os corpos-de-prova

impressos com a blenda tiveram aumento no módulo de elasticidade e limite de resistência à tração (1417 ± 101 MPa e 32 ± 1 MPa, respectivamente), acompanhado por uma diminuição significativa no alongamento em ruptura (23 ± 6 %) em razão da presença da fase de PS. A impressora 3D projetada não apenas elimina a dependência de matéria-prima filamentosa, mas combina composição de polímeros e deposição em uma única rota de processamento. Isso representa um passo significativo para a disponibilidade de um equipamento mais versátil que pode ser personalizado de acordo com as tarefas de processamento específicas e/ou aplicação pretendida. As possibilidades de pesquisa futura incluem o uso da impressora para integrar em uma única etapa a fabricação e impressão de blendas poliméricas, biocompósitos e bionanocompósitos para aplicações médicas personalizadas.

Palavras-chave: Processo aditivo por extrusão. Projeto customizado. Fabricação com pellets fundidos. Blendas poliméricas. Protótipo.

## ABSTRACT

JUSTINO NETTO, J. M. **Development of an innovative additive manufacturing equipment containing a co-rotating twin screw extrusion unit**. 2022. 165p. Thesis (Doctorate in Mechanical Engineering) – São Carlos School of Engineering, University of São Paulo, 2022.

The development of an innovative 3D printer containing a co-rotating twin screw extrusion unit (Co-TSE) is presented in this work. Material extrusion additive manufacturing (MEX) has been traditionally implemented by filament-based 3D printers with narrow commercial offer of materials. Since the mid-2000s, research efforts have been applied to develop MEX technologies that accept pellets or powders as raw material. The typical solution, based on single screw extrusion, enabled expanding the range of applicable materials, reducing printing costs, and increasing the deposition rates, but have limited process flexibility and mixing capacity. The new design combines a miniaturized modular Co-TSE operated under starve-fed conditions with a benchtop Cartesian platform, and accepts material in powder or micro-pellet form. As with industrial Co-TSE machines, the output and screw rotation speed can be set independently, and its dispersive and distributive mixing capacity can be fine tuned according to a given manufacture. Screw-assisted MEX was investigated in a systematic literature review, revealing the main design advantages, limitations and technology development workflow. The new equipment was developed in three major iterations, starting from the determination of the screw geometry to the simulation of the extrusion process, to ascertain whether the appropriate thermomechanical environment for polymer processing could be created by the proposed design. A functional prototype was built at the end of the third iteration. Extrusion tests were performed under different operating conditions, using polypropylene and a 90/10 wt% polypropylene/polystyrene blend. Two screw configurations were used, with and without kneading discs, to assess the response of the extrusion unit in terms of flow characteristics and mixing performance. The results showed that the mixing elements determine the starting melt position, and the average residence times, as well as the shearing levels which, in turn, affect the homogenization effectiveness. The screw configuration and rotation speed do not affect the output, which depends only on the feed rate. Preliminary deposition tests were conducted to determine the feasible printing parameters. A standard tensile test specimen, a square scaffold and a multicolored rectangular box were successfully printed, validating the innovative design. The mechanical properties of printed test specimens were within the expected values. The blend specimens showed na increase in the Young's module and ultimate tensile strength (1417 ± 101

MPa and 32 ± 1 MPa, respectively), accompanied by a significant decrease in the elongation at break (23 ± 6 %) due to the presence of the PS phase. The Co-TSE AM system not only eliminates the dependency on filamentary feedstock but combines polymer compounding and 3D printing in a single processing route. This represents a significant step towards the availability of a more versatile equipment that can be customized according to the required processing tasks and/or intended application. Future research avenues include using this printer to integrate into a single step the manufacture and printing of polymer blends, bio-composites, and bio-nanocomposites for personalized medical applications.

Keywords: MEX. Customized design. Fused pellet fabrication. Polymer blends. Prototype.

# LIST OF FIGURES

# LIST OF TABLES

# LIST OF ABBREVIATIONS

| | | |
|---|---|---|
| 3D | – | Three dimensional |
| ABS | – | Acrylontrile butadiene styrene |
| AM | – | Additive manufacturing |
| ASTM | – | American Society for Testing and Materials |
| BAAM | – | Big area additive manufacturing |
| ASTM | – | American Society for Testing and Materials |
| CAD | – | Computer aided design |
| Co-TSE | – | Co-rotating twin screw extruder |
| CNC | – | Computer numerical control |
| DEP | – | Department of polymer engineering |
| DC | – | Direct current |
| DIY | – | Do-it-yourself |
| DMLS | – | Direct metal laser sintering |
| DSM | – | Dispersed solids melting |
| EDM | – | Electrical discharging machine |
| FDM | – | Fused deposition modelling |
| FEUP | – | Faculty of engineering of the university of Porto |
| FFF | – | Fused filament fabrication |
| HRC | – | Hardness Rockwell C |
| IM | – | Injection molding |
| IR | – | Infrared |
| KB | – | Kneading block |

| | | |
|---|---|---|
| LH | – | Left handed |
| MEX | – | Material extrusion |
| PAM | – | Pellet additive manufacturing |
| PP | – | Polypropylene |
| PS | – | Polystyrene |
| PTFE | – | Polytetrafluoretylene |
| RAMPS | – | RepRap Arduino Mega Pololu Shield |
| RH | – | Right handed |
| RRUPE | – | Rich Rap Universal Pellet Extruder |
| SA-MEX | – | Screw-assisted material extrusion |
| SEM | – | Scanning electron microscopy |
| SLM | – | Selective laser melting |
| STL | – | Standard tessellation language |
| TSE | – | Twin Screw extruder |
| UTS | – | Ultimate tensile strength |

# LIST OF SYMBOLS

| | |
|---|---|
| A | Centerline distance between the screws (mm) |
| $A_1$ | Inherent throughput |
| $A_c$ | Conveyor cross-section area ($mm^2$) |
| $A_{free}$ | Free cross-section area ($mm^2$) |
| $a_T$ | Viscosity shift factor |
| B | Channel width (mm) |
| C | Correction factor for the angle of the feeder |
| Ca | Capillary number |
| $Ca_{crit}$ | Critical capillary number |
| $C_p$ | Specific heat (J/kg) |
| CD | Center distance (mm) |
| D | Diameter (mm) |
| DA | External diameter of the offset profile (mm) |
| DE | External diameter of the self-wiping profile (mm) |
| DI | Internal diameter of the self-wiping profile (mm) |
| DK | Internal diameter of the offset profile (mm) |
| $d_f$ | Filament diameter (mm) |
| $dH_m$ | Enthalpy of fusion (J/g) |
| $d_i$ | Individual droplet diameter (μm) |
| $d_o$ | Nozzle diameter (mm) |
| $d_n$ | Number-average droplet diameter (μm) |
| $d_v$ | Volume-average droplet diameter (μm) |
| E | Modulus of elasticity (Pa) |
| $F_{max}$ | Maximum force in a steady simple flow field (N) |
| $F_R$ | Filament feed rate (mm/s) |
| f | Screw fill ratio |
| FW0 | Flank angle of the self-wiping profile (rad) |
| FW1 | Flank angle of the offset profile (rad) |
| h | Bead height (mm) |
| $h_c$ | Screw channel height (mm) |
| $K'$ | Die conductance ($m^3$) |
| k | Power law consistency factor ($Pa \cdot s^n$) |

| | |
|---|---|
| KB0 | Tip width of the self-wiping profile (mm) |
| KB1 | Tip width of the offset profile (mm) |
| KW0 | Tip angle of the self-wiping profile (rad) |
| KW1 | Tip angle of the offset profile (rad) |
| L | Length of the screw element (mm) |
| $L_n$ | Length of the nozzle (mm) |
| $L_p$ | Belt perimeter (mm) |
| L/D | Length to diameter ratio |
| $l_f$ | Filament length (mm) |
| $l_e$ | Length of filament entering the print head (mm) |
| $M_T$ | Torque (N·m) |
| m | Flow exponent |
| N | Screw rotation speed (rpm) |
| $N_f$ | Feeder speed (rpm) |
| NW | Root angle (rad) |
| n | Pseudoplasticity index |
| P | polydispersity |
| PD | Pitch diameter of the pulleys (mm) |
| $PD_G$ | Pitch diameter of the gears |
| p | Pressure (Pa) |
| Q | Feed rate (g/h) |
| q | Heat flux (J) |
| R | Radius of a circular tube (m) |
| $R_o$ | Larger radius of a cone (m) |
| $r_o$ | Smaller radius of a cone (m) |
| $r_n$ | Nozzle radius (mm) |
| s | Screw/screw clearance (mm) |
| T | Pitch (mm) |
| $T_c$ | Pitch of the conveyor screw (mm) |
| $T_i$ | Inlet temperature ( ºC) |
| $T_o$ | Outlet temperature ( ºC) |
| $\bar{t}_v$ | Mean residence time (s) |
| $\dot{V}$ | Volumetric flow rate ($mm^3/s$) |

| | |
|---|---|
| $\dot{V}_{max}$ | Maximum volumetric flow rate ($mm^3/s$) |
| $V_{free}$ | Free volume of the twin screw ($mm^3$) |
| v | Tangential velocity of the screw (mm) |
| $v_{in}$ | Linear velocity of the pintch rolers (mm |
| $v_d$ | Deposition speed (mm/s) |
| w | Bead width (mm) |
| Z | Number of flights |
| $\dot{\gamma}$ | Shear rate ($s^{-1}$) |
| γ | Shear strain |
| $\overline{\dot{\gamma}}$ | Global average shear rate ($s^{-1}$) |
| $\overline{\dot{\gamma}}_{yz}$ | Downchannel average shear rate ($s^{-1}$) |
| $\overline{\dot{\gamma}}_{xy}$ | Cross-channel average shear rate ($s^{-1}$) |
| Γ | Surface tension (N/m) |
| δ | Screw/barrel clearance (mm) |
| Δ | Variation |
| $\dot{\varepsilon}$ | Elongation rate ($s^{-1}$) |
| ε | Strain |
| η | Viscosity (Pa·s) |
| $\eta_0$ | Zero-shear-rate viscosity (Pa·s) |
| $\eta_\infty$ | Infinite-shear-rate viscosity (Pa·s) |
| $\eta_e$ | Elongational viscosity (Pa·s) |
| θ | Angular coordinate of the screw profile (rad) |
| λ | Time constant (s) |
| Λ | Kinematic parameter of flow |
| ρ | Density ($kg/m^3$) |
| $\sigma_{cr}$ | Critical filament compression stress (Pa) |
| φ | Flight angle (rad) |
| Φ | Fluidity factor $(Pa \cdot s^n)^{-1/n}$ |
| ψ | Loading efficiency of the conveyor section |

# CONTENTS

# 1 INTRODUCTION

Additive manufacturing (AM), also known as three-dimensional (3D) printing, embodies various processes by which accumulation of material is used to directly produce 3D parts [1]. According to the standard terminology, the material extrusion (MEX) AM technique is characterized by the selective dispensing of softened materials through a nozzle, which generates continuous strands or filaments that are usually deposited layer upon layer to build a 3D structure [2].

The vast majority of the MEX 3D printers are based on the Stratasys` FDM® (fused deposition modeling) patent, and require material in filament form. Due to its low implementation cost and easy operation [3,4], the filament-based 3D printing technique revolutionized the toolbox of available manufacturing technologies, boosting rapid prototyping and opening the possibility of manufacturing complex parts without the need of a mould [3,5].

Even though the filament 3D printers have become very robust and compatible with a range of polymers [3], the search for novel materials and applications, higher deposition speeds, and reduction of the costs associated with the feedstock lead to the development of alternative MEX systems containing piston- and screw-assisted extrusion units [4,6,7]. The first screw-assisted MEX 3D printers were put together using simplified vertical single-screw extruders, for direct printing from powders or pellets. With time, the extrusion units were further developed to enable new applications involving polymer recycling [8,9], biofabrication [10-14], low-cost metal and ceramic 3D printing [15-18], and personalised medicine [19-21]. Although single screw extruders offer an improved control over the plastication process and can reach higher deposition rates, their output is not solely dictated by the screw speed but also depends on the nozzle geometry and polymer rheology. Moreover, their mixing ability is limited [22].

Recently, the development of desktop 3D printers with counter-rotating twin screw extrusion (TSE) units has been reported. Bhattacharyya et al. [23] designed a partially intermeshing counter-rotating TSE with variable pitch and shallow channels, to print multi-component bioinks in a single platform. A proof-of-concept prototype was built and tested to assess the mixing quality of a cell-loaded nanocomposite gel at ambient temperature, as well as the cell viability after deposition. Bai et al. [24] designed a fully intermeshing counter-rotating TSE, but a working prototype was not presented.

It would be noted that counter-rotating TSE have good pressure generation capacity, but dispersive mixing is poor and the maximum attainable screw speeds must be very low in order to prevent premature screw and barrel wear [22]. Co-rotating twin screw extruders (Co-TSE), on the other hand, are very flexible machines that can be adapted in terms of number and type of its functionals zones, can be operated with high screw speeds and have good output capacity [25].

Despite of the advantageous characteristics of Co-TSE and its increasing popularity for compounding operations and extrusion cooking, these machines seem to have been largely ignored for additive manufacturing applications. Thus, the present work presents and discusses the complete design of an innovative 3D printer containing a co-rotating twin screw extrusion unit. The equipment, henceforth referred as Co-TSE AM system, aims not only to circumvent the dependency on filamentary materials but to allows small scale compounding studies and 3D printing in a single route. This work contributes, therefore, to the availability of more versatile 3D printers that can be customized to meet specific processing tasks or applications.

## 1.1 Objective

The purpose of this work is to investigate whether a miniaturized Co-TSE can be integrated to a 3D indexing platform so as to result in an innovative 3D printer. In terms of development process, the present work continues the project previously started by the author and focus on the system-level design stage, which was carried out in three main iterations. The main objective was achieved by addressing the following specific goals:

- Investigate the design configurations, advantages, limitations and development of screw-assisted 3D printers;
- Detail the main components of the system, prototype and test the system until it is considered apt to perform polymer compounding and 3D printing;
- Perform polymer compounding and 3D printing experiments to validate the new design in terms of the flow characteristcs and mixing performance of the extrusion unit, and in terms of its 3D deposition capacity and printing quality.

## 1.2 Thesis structure

Following the flowchart presented in Fig. 1, this thesis is divided into five chapters. **Chapter 1** corresponds to the introductory section; **Chapter 2** provides the theoretical

framework that supported the development of this work; **Chapter 3** brings a systematic literature review on screw-assisted MEX, which is based on a published paper entitled “Screw-assisted 3D printing with granulated materials: a systematic review”; **Chapter 4** documents the development process of the Co-TSE AM system; followed by its experimental validation in **Chapter 5**. Both chapters were based on two published papers entitled “Design of an Innovative Three-Dimensional Print Head Based on Twin-Screw Extrusion” and “Design and validation of an innovative 3D printer containing a co-rotating twin screw extrusion unit”. **Chapter 6** summarizes the general conclusions of the work and suggests further research opportunities.

*Figure 1. Flowchart of the thesis structure.*

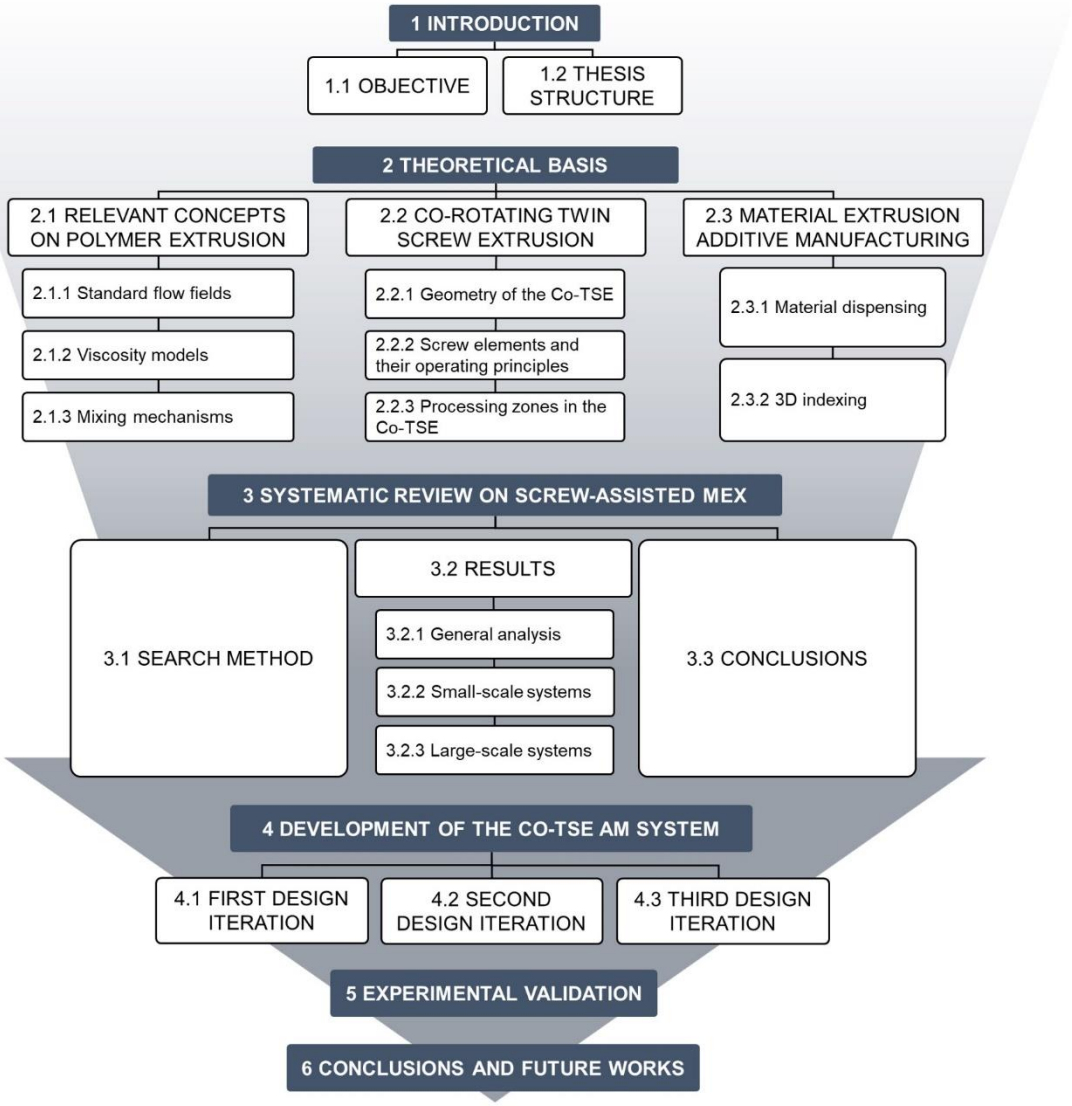


*Source: the author*

# 2 THEORETICAL BASIS

This chapter presents the theoretical basis for the development of the thesis. The first section recovers some background concepts related to polymer extrusion. In Secton 2.2, important aspects about the design and technology of Co-TSE are presented. The last section presents the main functional stages of MEX and how they are usually carried out in filament-fed 3D printers.

## 2.1 Relevant concepts on polymer extrusion

Polymer processing comprises a series of "operations carried out on polymeric materials or systems to increase their utility" [26]. Most thermoplastics are melt-processed so that they can flow and be formed, adopting very complex shapes. Melt processing is also used to achieve certain properties or expected performance [27,28]. From the variety of melt processing techniques available, screw extrusion can be deemed as almost universal. The vast majority of thermoplastics undergo at least one extrusion process along their lifecycle [29].

Due to their macromolecular structure, the flow behavior of molten polymers is quite different from that of Newtonian fluids [30]. In the next topics, concepts on some representative flow fields and polymer rheology are introduced, laying the foundations to understand the flow behavior developed in screw extrusion with special attention to the mechanisms for polymer mixing.

### 2.1.1 Standard flow fields

Since the flow fields created in processing equipment can become rather complex, the behavior of molten polymers is usually described in terms of some representative flow fields for Newtonian fluids. Figure 2 represents a flow field between two parallel plates with very small gap-to-width ratio. The fluid between the plates is forced to flow by drag (Fig. 2a), when the upper plate is moved in relation to the lower plater; or by pressure (Fig. 2b), when a pressure gradient is established along the length of the channel. A shear flow is developed in both situations [31].

*Figure 2. Shear flows fields created by a) drag, and b) a pressure gradient.*

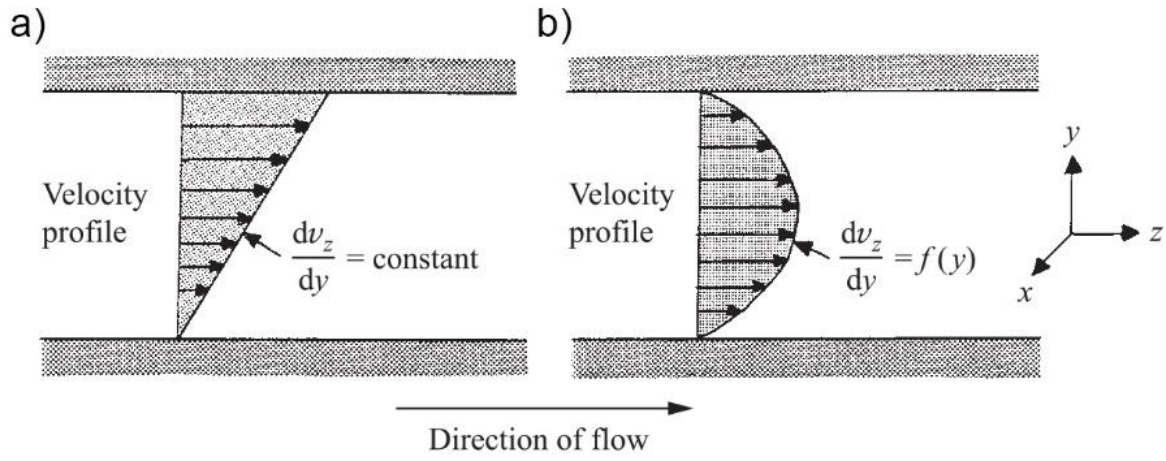


*Source: [31]*

Shear flows are characterized by a velocity gradient perpendicular to the flow direction. In the case of the drag induced flow, the velocity profile is linear with respect to the channel height and the shear flow field is considered uniform. On the other hand, the velocity profile along the channel height for the pressure-driven flow is parabolic and, thus, the shear flow is considered non-uniform. The shear rate ($\dot{\gamma}$), defined as the variation of shear strain ($\gamma$) with time (t), is expressed by Eq. 1 [32].

$$\dot{\gamma} = \frac{d\gamma}{dt} \tag{1}$$

In the extruder, shear flows occur near the equipment walls due to the relative movement between screw and barrel surfaces, as well as in fully filled regions due to pressure build-up [22]. The shear flows tend to distort the fluid elements, increasing their length and reducing their width, ultimately causing (re)orientation to the flow direction [33].

Elongational flows are characterized by a velocity gradient aligned to the flow direction. The elongation rate ($\dot{\varepsilon}$) is calculated by Eq. 2 in terms of the variation of strain ($\varepsilon$) with time (t) [22,32,34].

$$\dot{\varepsilon} = \frac{d\varepsilon}{dt} \tag{2}$$

Uniaxial elongational flows can be identified in free surfaces, when the polymer is stretched after leaving the die (*e.g.* through a 3D printing nozzle or in fiber drawing processes, Fig 3a). The flow describes a three-dimensional pattern, represented in Fig. 3b, with intense stretching in the flow direction, and contraction in the other two directions. Elongational flows

can be also observed within geometries defined by converging solid boundaries, where they are often accompanied by shear flows. The situation is represented in Fig. 3c [22,32,34].

*Figure 3. Representations of elongational flows: (a) in fiber spinning, (b) velocity fields in uniaxial elongational flow, (c) elongational flow in a converging channel.*

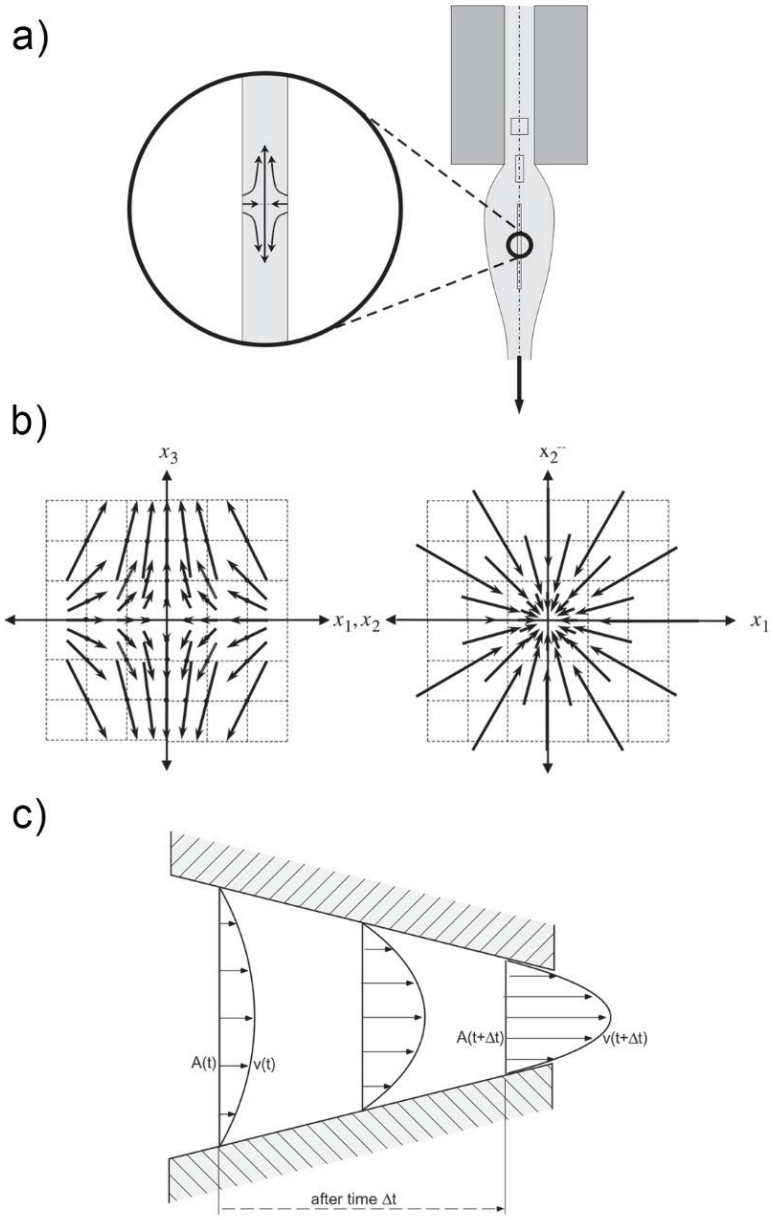


*Source: (a) and (b) adapted from [32], (c) adapted from [22]*

In general, elongational flows can only be developed inside the extruder when specific screw geometries are used. These are associated with narrow cross-sections or tapered channels, where the fluid elements are compressed and extended. Due to its importance to the mixing quality, elongational flows are much sought after in compounding operations [34,35]. Its role on dispersive mixing will be examined after the next topic.

### 2.1.2 Viscosity models

Different from the elastic solids, a liquid tends to deform continuously upon stress application, and cannot return to its undeformed state after stress removal. Because the stiffness or modulus varies with time, it cannot be used to define a material property. However, for a liquid under constant stress, the rate of deformation is not time-dependent but actually proportional to the applied stress. The constant of proportionality between stress and strain rate is the viscosity [34].

As a rule, the shear viscosity of molten polymers is constant only at low shear rates. Beyond a critical shear rate value, the viscosity tends to decrease due to the progressive molecular orientation, characterizing the so-called pseudoplastic behaviour. At higher shear rates, the Newtonian behavior (*i.e.* constant viscosity) can be observed again [31,32]. It should be noted that the same does not necessarily apply to the extensional viscosity. However, the flow behavior of molten polymers is rarely described in terms of their properties in extension. This is because pure elongational flows are not simple to achieve, and extentional rheometry is a field still in development [32].

The typical behavior of the shear viscosity for molten polymers is represented in Fig. 4, which evidences the intermediary pseudoplastic region, as well as the Newtonian plateaus for low and high shear rates [32]. The symbols ($\eta_0$) and ($\eta_\infty$) represent the zero-shear-rate viscosity and the infinite-shear-rate viscosity, respectively [22].

*Figure 4. Typical behavior of the viscosity of molten polymers.*

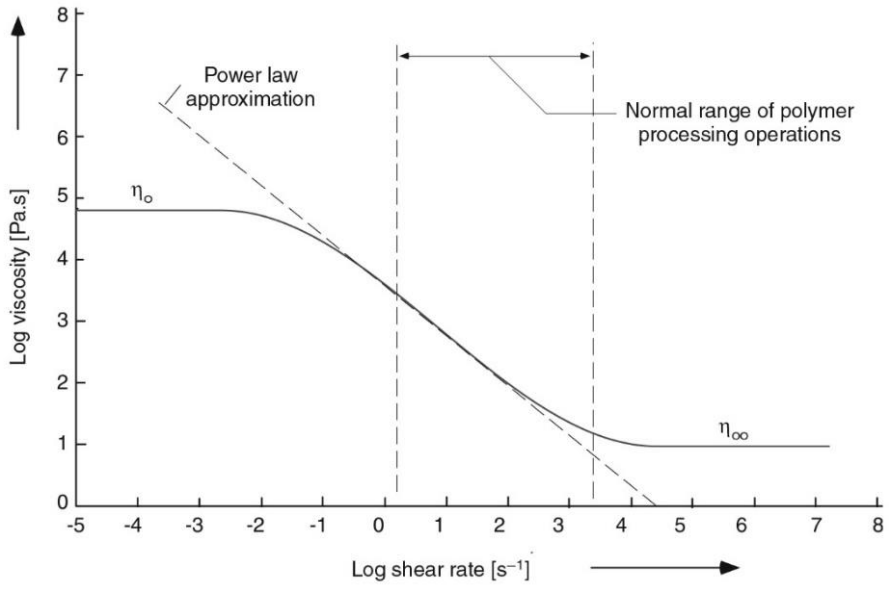


*Source: [22]*

The variation of viscosity (η) with the shear rate ($\dot{\gamma}$) can be described by the power-law model, expressed in Eq. 3, in which k is called the consistency index, and n is the pseudoplasticity index. The pseudoplasticity index ranges from 1 to 0, with the smaller values indicating a steeper viscosity decrease with increasing shear rate [22,32,34].

$$\eta(\dot{\gamma}) = k\dot{\gamma}^{n-1} \tag{3}$$

The power-law model is simple but does not describe the complete shape of experimentally measured flow curves [31,32].

Alternatively, the shear viscosity can be calculated for the entire range of shear rates with the Carreau-Yasuda model, expressed in Eq. 4. The model includes parameters for the zero-shear-rate viscosity ($\eta_0$), infinite-shear-rate viscosity ($\eta_\infty$), a time constant (λ), a dimensionless constant (a), and the power-law index (n). The constant λ determines the shear rate at which the first transition from the Newtonian plateau to the power-law-like portion occurs, and *a* affects the shape of the transition between these regions [32,36].

$$\frac{\eta - \eta_0}{\eta_0 - \eta_\infty} = [1 + (\lambda\dot{\gamma})^a]^{(n-1)/a} \tag{4}$$

For a semicrystalline polymer above the melting point and at a fixed shear rate in the pseudoplastic region, an Arrhenius relation can be used to describe the temperature effect on the viscosity. The temperature dependence is expressed in Eq. 5, where A is a preexponential constant, E is the activation energy for flow, R is the gas constant, and T is the absolute temperature [31,34].

$$\eta = Aexp(E/RT) \tag{5}$$

A shift factor ($a_t$) can be defined, representing the ratio between the viscosities at two reference temperatures. As expressed in Eq. 6, the manipulation eliminates the preexponential constant [31].

$$a_t = \frac{\eta_0(T)}{\eta_0(T_o)} = exp\left[\frac{E}{R}\left(\frac{1}{T} - \frac{1}{T_0}\right)\right] \tag{6}$$

When the infinite-shear-rate viscosity can be neglected, the Carreau-Yasuda equation can be modified to a three-parameter model. The modified model (Eq. 7) can also include the temperature dependent term $a_t$ [36].

$$\eta(\dot{\gamma}, \mathrm{T}) = \eta_0 a_T[1 + (\lambda a_T\dot{\gamma})^a]^{(n-1)/a} \tag{7}$$

The modified Carreau-Yasuda model is particularly useful to calculate the viscosity of polymers in extrusion processes, in which the shear rates developed are low or moderated.

### 2.1.3 Mixing mechanisms

The general aim of the mixing operations is to reduce compositional non-uniformity in a given volume [22,37]. Mixing with high viscosity materials, such as with polymer systems, occurs mainly by mechanisms attained in laminar flow. A flow regime is considered laminar when its fluid elements move in straight lines, in the absence of eddies. The condition is often reffered in terms of a low Reynolds number (Re), which represents the ratio between the inertial and viscous forces in the fluid [22,29].

Distributive or extensive mixing occurs when the components to be mixed do not exhibit a yield point [22]. Spatial redistribution due to flow partition, as well as shear and extensional deformation leads to an increase in the interfacial area, indicating that mixing has taken place. Thus, the number of flow divisions and the extent of deformation are the main factors for improved distribution [33]. The mechanisms associated with distributive mixing are illustrated in Fig. 5.

*Figure 5. Distributive mixing mechanisms: (a) slicing and rotation, (b) strain and shearing deformation.*

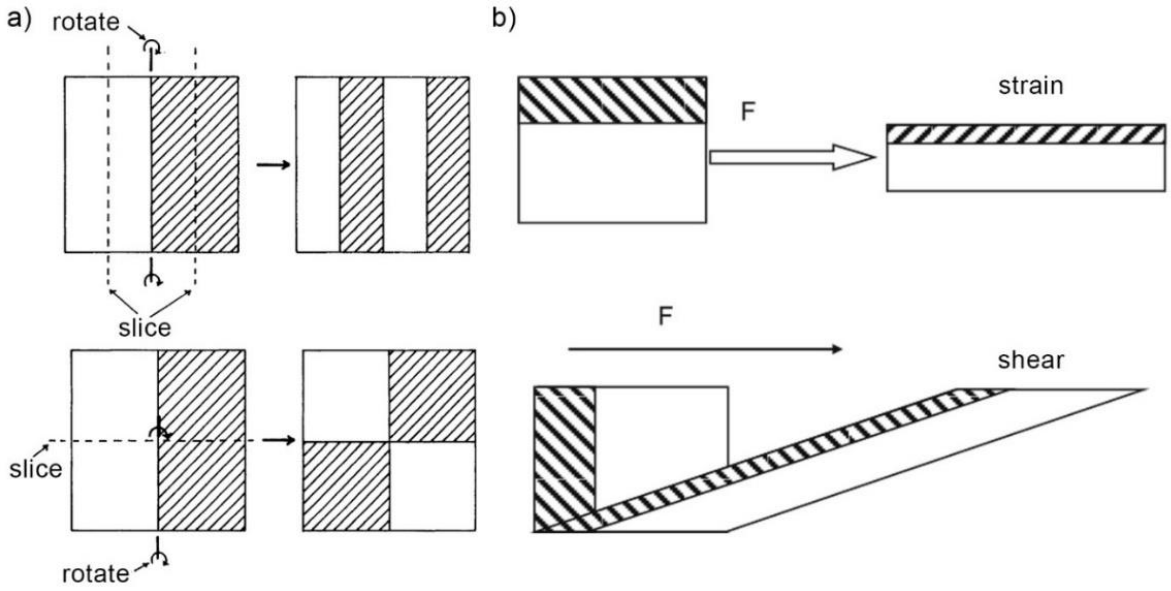


*Source: (a) adapted from [33], (b) adapted from [38]*

It is important to note that for laminar shear mixing the fluid elements must be perpendicular to the flow field, otherwise there will be no mixing effect. That is why fluid

redistribution is so important. In addition, it has been demonstrated that extentional deformation, particularly at large strains, is more effective to generate new surface areas [33].

Dispersive or intensive mixing involves disaggregating solid particles, liquid droplets, or gas bubbles. Dispersion is achieved only when the yield stress of the minor component is exceeded, which in turn depends on the characteristics of the agglomerate, flow field and rheological properties of the fluid(s) [22,37].

The simplified analysis of dispersion in solid-liquid systems models the agglomerates as rigid dumbbells in a homogeneous flow field. The applied force depends on the viscous drag acting on each sphere and on the orientation of the dumbbell. Provided the dumbbell is oriented at 45º angle in relation to the flow direction, the maximum force ($F_{max}$) developed in a steady simple flow field is calculated by Eq. 8 [22].

$$F_{max} = 3\pi\eta_s\dot{\gamma}r_1r_2 \quad (8)$$

Where $\eta_s$ is the viscosity of the fluid in shear, ($\dot{\gamma}$) is the shear rate, and $r_1$ and $r_2$ are the radii of the contacting spheres forming the dumbbell. The force is proportional to the shear stress and to the product of the size of the spheres. Thus, the force generated by the same flow field is progressively reduced with the comminution of the particles. At some point, the flow conditions will be unable to generate the required breakdown force and further dispersion will not occur [22].

The maximum force developed in a steady elongational flow, achieved when the dumbbell is aligned to the flow direction, is expressed by Eq. 9 in function of the elongational viscosity ($\eta_e$), elongation rate ($\dot{\varepsilon}$), and the radii of the spheres ($r_1$ and $r_2$). Again, the achievable force decreases as the size of the particles is reduced [22].

$$F_{max} = 6\pi\eta_e\dot{\varepsilon}r_1r_2 \quad (9)$$

From the previous equations, it can be inferred that the forces achieved in elongational flow are two times larger than in simple shear (considering similar deformation rates and viscosity). The analysis however assumed a Newtonian fluid. In practice, the elongational viscosity of molten polymers is usually much higher than the shear viscosity and, therefore, dispersive mixing is often more efficient under elongation flow. Another aspect revealed by the analysis is that, since the breakdown force is proportional to the fluid viscosity, dispersion in high-viscosity melts is facilitated [22].

Besides the stress intensity, exposure time also plays an important role in dispersion. In fact, it has been demonstrated that (within limits) long residence times can compensate low shear stresses and vice versa [22,37].

For liquid-liquid systems, *e.g.* when mixing two or more immiscible polymers, dispersion is analysed with respect to ratio between the forces trying to deform the phase domains of the minor component to the forces trying to hold it together. The ratio is called the Capillary number (Ca), and is expressed in Eq. 10 in function of the viscosity of the continuous phase (*i.e.* matrix) (η), shear rate ($\dot{\gamma}$), surface tension (Γ), and radius (r) of the dispersed phase, which is assumed to form droplets [22,37].

$$Ca = \frac{\eta\dot{\gamma}}{\Gamma/r} \tag{10}$$

When the viscous stress dominates the interfacial stress, the drops are stretched until eventually break-up occurs. Breakdown occurs only when the Capillary number is larger than a critical value ($Ca_{crit}$), which in turn depends on the viscosity ratio between the dispersed and continuous phase and the flow conditions. Figure 6 plots the $Ca_{crit}$ determined for a range of viscosity ratios under simple shear and 2-D elongation flows [22].

*Figure 6. Critical capillary number vs. the viscosity ratio in simple shear and 2-D elongation.*

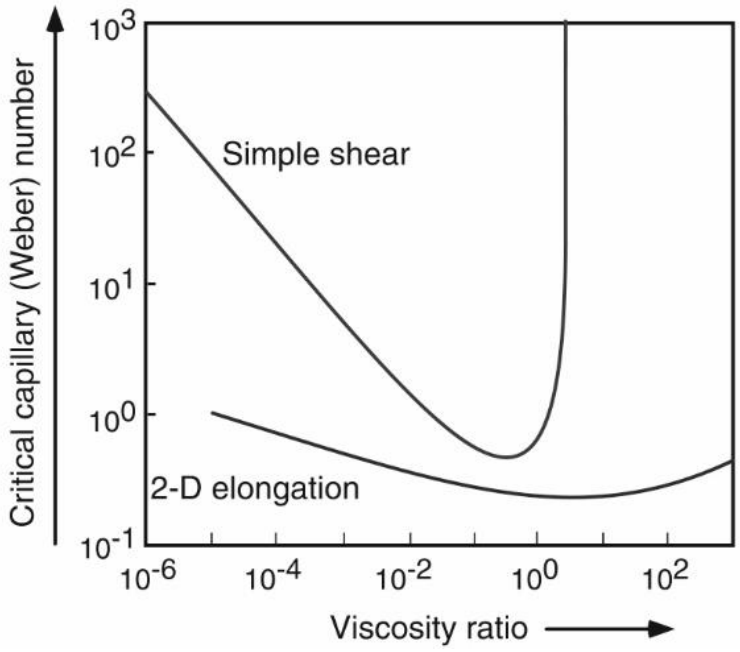


*Source: [22]*

Once again, the efficiency of the elongational flows against shear flows should be noted. The $Ca_{crit}$ in simple shear is generally larger than in 2-D elongation. Moreover, $Ca_{crit}$ goes to

infinity when the disperse phase is considerably more viscous than the matrix (usually from viscosity ratios above 3.5) [22,37].

Different droplet break-up mechanisms have been observed in dispersion experiments with molten polymers, their occurrence depending on the Capillary number and viscosity ratio. In general, at moderate values of Ca the original droplets are divided into two smaller ones, in a mechanism termed necking. If the flow is subject to sudden changes, the droplets are transformed into dumbbells, and smaller drops eventually are torn off from their extremities. This mechanism is called end pinching. At high values of Ca, the droplets elongate in thin fibrils and interfacial instabilities become important. Depending on the viscosity ratio, the fibrils can break into multiple smaller droplets, characterizing the Rayleigh breakup mechanism. The tip streaming mechanism, associated with the release of fine droplets form the fibrils, can be observed in systems with low viscosity ratios. For systems wth high viscosity ratios, *i.e.* when the viscosity of the droplet is much higher than the matrix, no initial deformation was observed. Instead, the original droplets are eroded. The described mechanisms are represented in Fig. 7 [39].

*Figure 7. Droplet break-up mechanisms observed with molten polymer blends.*

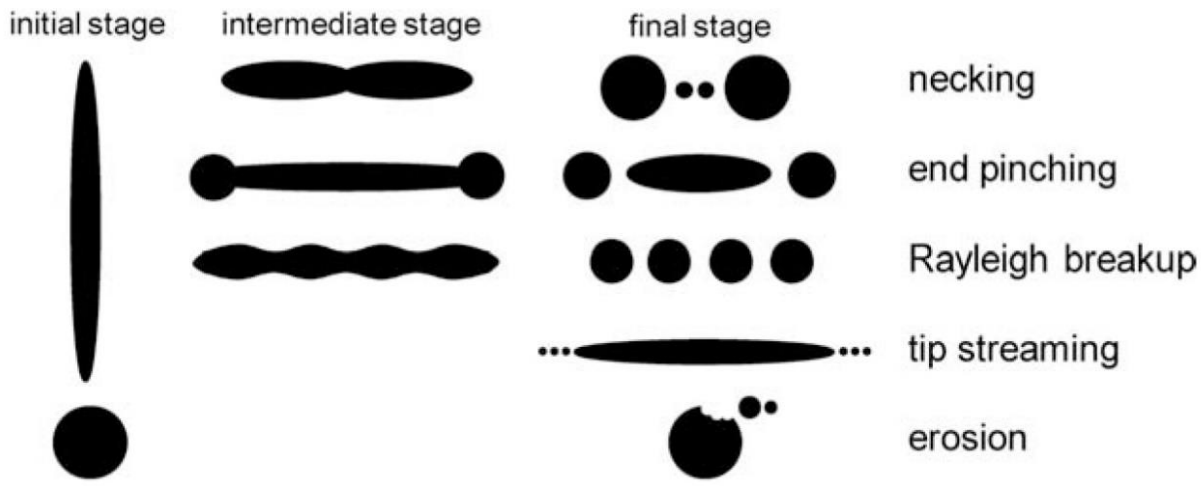


*Source: [39]*

## 2.2 Co-rotating twin screw extrusion

Polymer extrusion is a major industrial processing technology. While single screw extruders are generally adopted to yield continuous products with a constant cross-section (*e.g.*, pipes and tubing, profiles, film & sheet, wire insulation, filaments and fibers), co-rotating twin screw extruders are increasingly used in compounding operations, *i.e.*, polymerization,

homogenization, devolatilization, additivation, blending, modification or polymer reinforcement, followed by pelletization [22].

In general, the co-rotating twin screw extruders used in polymer compounding are

> [...] extruders with two parallel-axis screws of identical geometry, which rotate in the same direction and with the same angular velocity. As a rule, both screws possess the same outside diameter over the entire length of the screw and each point on the surface of one screw is scraped by the other screw [40].

The terminology varies according to the author: the terms tightly intermeshing [40], closely self-wiping [22], and closely intermeshing [35], amongst others, are all used to refer to the same machine with the so-called self-wiping twin screw.

In the following topics the geometry of these machines, henceforth referred to as co-rotating twin screw extruders (Co-TSE), are detailed. The characteristics and functions of the standard screw elements are described. The last topic provides an overview on the polymer behavior in the individual processing zones along the extruder.

### 2.2.1 Geometry of the Co-TSE

A crucial difference between the closely self-wiping co-rotating twin screw extruders and the ordinary intermeshing (non-self-wiping) co-rotating extruders relates to the open areas in the intermeshing region. As shown in Fig. 8, the open areas of the non-self-wiping type tend to be smaller, hindering material flow between the adjacent screw channels and promoting some positive conveying to the extruder [22].

*Figure 8. Comparison between the open areas of the a) non-self-wiping and b) self-wiping co-rotating twin screw extruders.*

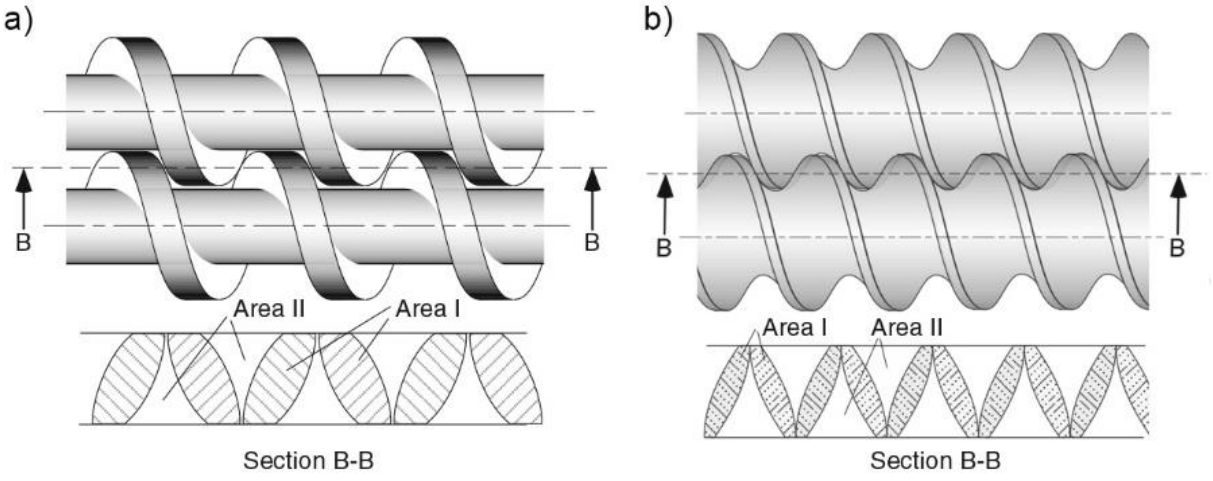


*Source: adapted from [22]*

The reduced space available for the material in the intermeshing region of the non-self-wiping extruders, as well as the change in flow direction, cause local pressure peaks that lead to lateral forces trying to separate the screws. On the other hand, the considerable openness of the Co-TSE facilitates material flow between the screws, preventing pressure build-up in the intermeshing region. Although this leads to less positive conveying characteristics, the self-wiping screws can be designed with small clearances and the machine is able to operate at higher speeds, as required for compounding operations [22].

The mathematically precise self-wiping profile depends only on three variables: the external diameter (DE), the centerline distance (A), and the number of threads (Z). For a given number of threads, small values of the A/DE ratio result in higher free cross-sectional area available to transport material. However, if the ratio is too small, proper screw intermeshing cannot be achieved. That condition is expressed by the Ineq. 11 [35]:

$$\frac{A}{DE} \geq \cos\left(\frac{\pi}{2Z}\right) \tag{11}$$

Figure 9 shows the self-wiping profile for double-flighted screws, evidencing the external diameter (DE), centerline distance (A), maximum channel depth ($h_{max}$), and the intermeshing angle (Ω).

*Figure 9. Self-wiping profile of the double-flighted twin screw*

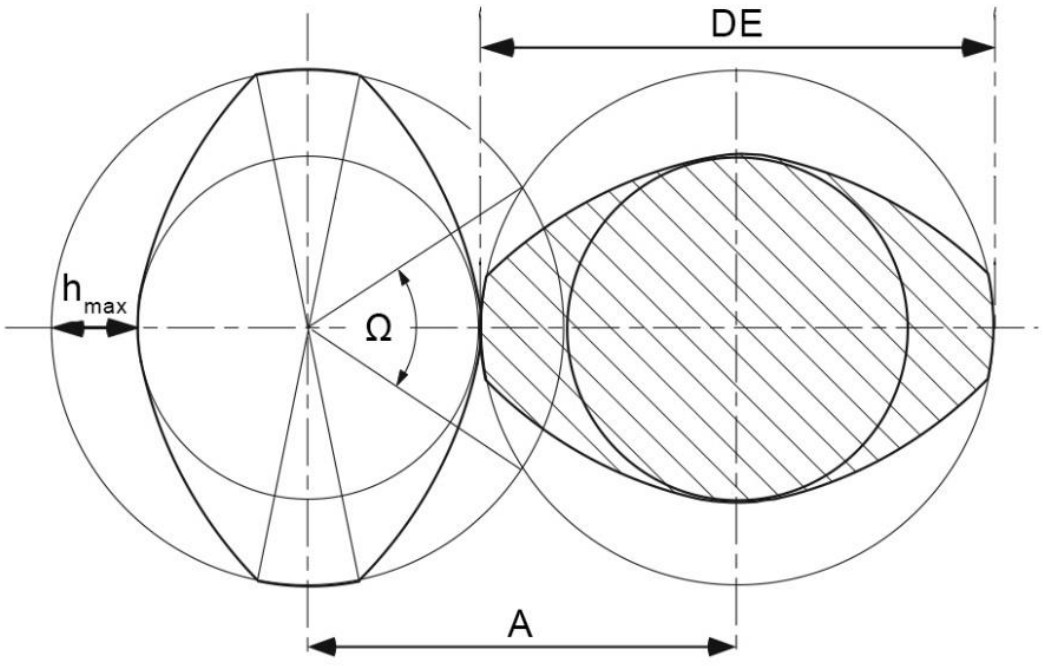


*Source: adapted from [37]*

The channel depth (h) can be calculated by Eq. 12, as a function of the angular coordinate θ. The equation is valid in the range $0 \leq \theta \leq \Omega$, with the intermeshing angle (Ω) expressed by Eq. 13, in radians [35,40].

$$h(\theta) = \frac{DE}{2}(1 + \cos\theta) - \sqrt{A^2 - \left(\frac{\mathrm{DE}}{2}\right)^2 \sin^2\theta} \tag{12}$$

$$\Omega = 2\cos^{-1}\left(\frac{A}{DE}\right) \tag{13}$$

The internal diameter (DI) of the screw is calculated by Eq. 14 [35]:

$$DI = 2A - DE \tag{14}$$

A simple method to draw the self-wiping profile for a double-flighted screw is schematized in Fig. 10.

*Figure 10. Sequence of steps to draw the self-wiping profile for a double-flighted screw.*

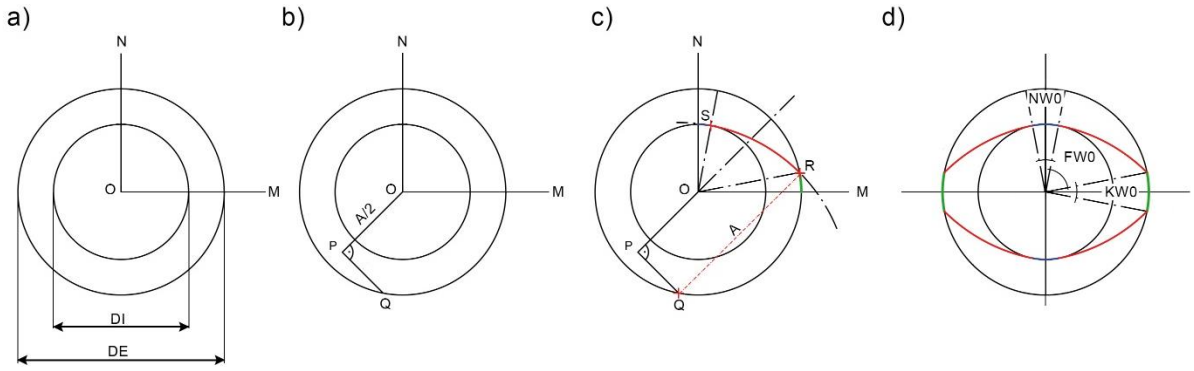


*Source: adapted from [37]*

In the first step (Fig. 10a), it is necessary to draw two circles with center O: one with the external diameter DE, and other with the internal diameter DI. The symmetry lines OM and ON and drawn. Then (Fig. 10b), the angle-bisecting line OP between the symmetry lines is drawn. The length of this line is equal to half the centerline distance (A/2). Another line PQ, perpendicular to OP, is drawn intersecting the external circle. Next (Fig. 10c), and arc centered in Q, and with radius equal to the centerline distance (A) is described. The arc intersects the circle with diameter DE at the point R, and is tangent to the circle with diameter DI at the point S. The arc secgments in green, red and blue correspond respectively to the tip, flank and root of the screw profile. In the final step (Fig. 10d), the screw segments can be mirrored with respect to the symmetry lines resulting in the completed self-wiping profile. The tip, flank and root angles (KW0, FW0, and NW, respectively) are shown in the drawing.

The exact free cross-section area ($A_{free}$) of the self-wiping profile can be calculated from the difference between the barrel area and the area of the screw profiles. The equations are described in Potente et al. [40] and depend ultimately on the three main design variables (A, DE, and Z). Alternatively, $A_{free}$ can be estimated with respect to the squared screw diameter ($DE^2$) in function of the A/DE ratio. The relationship is plotted in Fig. 11, for screws with one to four flights. Besides the influence of A/DE, the graph shows that $A_{free}$ tends to increase with the number of flights.

*Figure 11. Relationship between $A_{free}/DE^2$ and A/DE for different numbers of threads.*

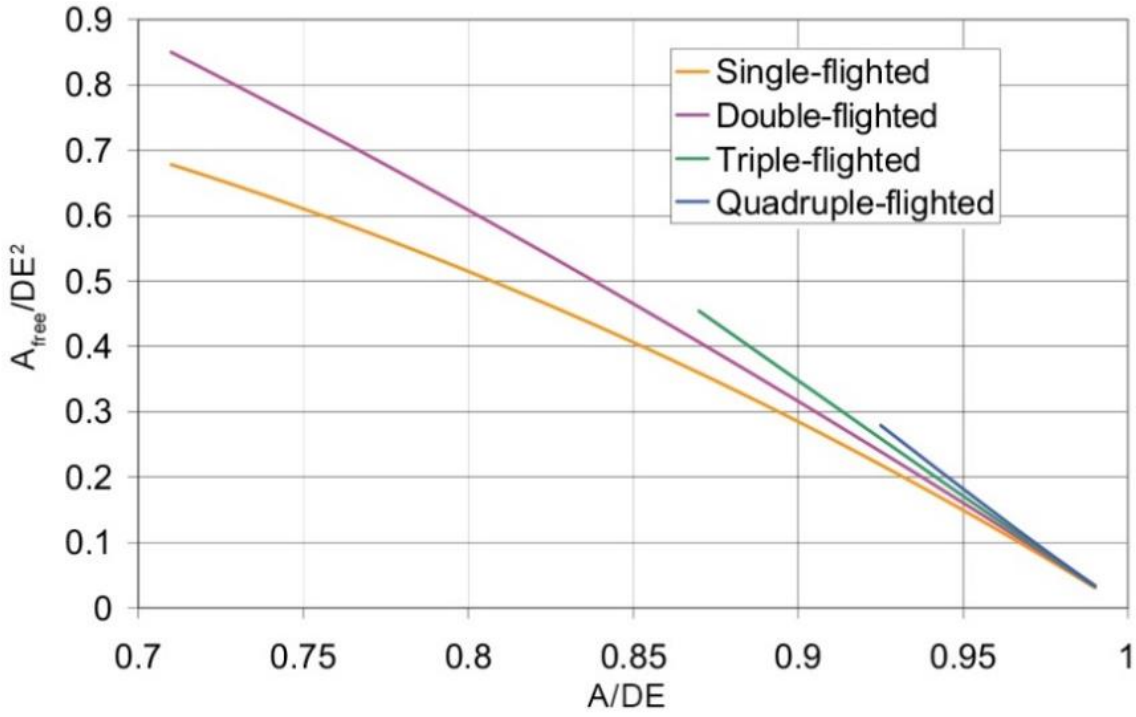


*Source: [37]*

When it comes to the practical twin screw geometry, the self-wiping profile must be reduced by the required clearances to compensate for manufacturing tolerances, prevent metallic erosion and avoid product overheating. Although the clearances between the screws can be created simply by enlarging the centerline distance, the resulting gap in the longitudinal section is not constant. That way, the screws might collide during operation [35,40].

As discussed by Kohlgrüber [35], the perfectly constant clearance at the flanks would be created by offsetting the geometry of the screws through a spatial curve. Given the complexity of that approach, the so-called planar offset is the strategy of choice that results in a fairly uniform longitudinal gap. In short, the planar offset method shifts the fully wiped profile inwards by half the clearance between the screws (s). The procedure is schematized in Fig. 12.

*Figure 12. Longitudal cross-section of a double-flighted screw showing the difference between the self-wiping profile (external contour, in green) and the offset profile (internal contour, in red).*

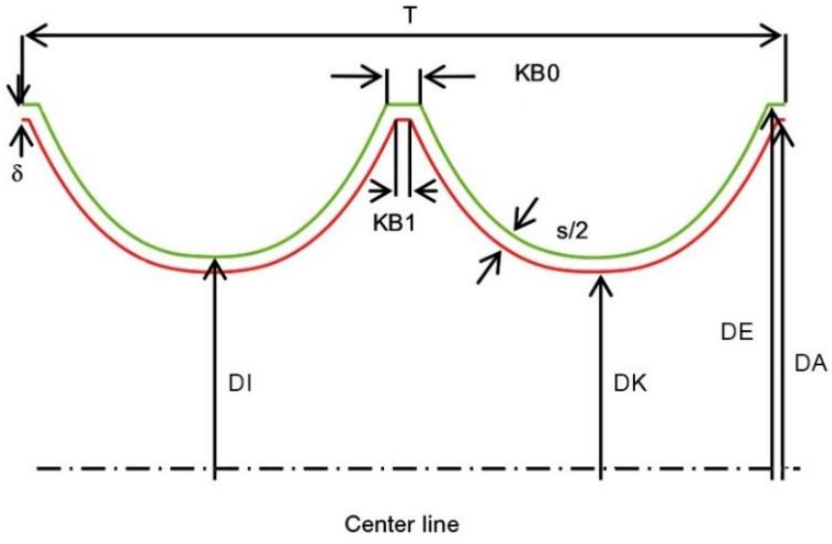


*Source: adapted from [37]*

The first step is to draw the longitudinal section of the self-wiping profile. The coordinates (x, y) are calculated by Eq. 15 in which the x-values are defined according to different regions of the screw (root, flank and tip, respectively) [35].

$$y = \begin{cases} DI/2, & 0 < x \leq \dfrac{KB0}{2} \\ f(x), & \dfrac{KB0}{2} < x \leq \dfrac{T}{2Z} - \dfrac{KB0}{2} \\ \mathrm{DE}/2, & \dfrac{T}{2Z} - \dfrac{KB0}{2} < x \leq \dfrac{T}{2Z} \end{cases} \tag{15}$$

Where KB0 is the tip width, and T is the pitch. KB0 is calculated according to Eq. 16 [35]:

$$KB0 = \mathrm{T}\left[\frac{1}{2Z} - \frac{\cos^{-1}(A/DE)}{\pi}\right] \tag{16}$$

The flank curve of the self-wiping profile is described by the function f(x), expressed by Eq. 17 [35].

$$f(x) = -\frac{\mathrm{DE}}{2}\cos\left(2\pi\frac{x - KB0/2}{T}\right) + \sqrt{A^2 - \left(\frac{\mathrm{DE}}{2}\right)^2}\sin\left(2\pi\frac{x - KB0/2}{T}\right) \tag{17}$$

Once the longitudinal profile has been drawn, the coordinates ($x_a$, $y_a$) of the offset profile can be determined. The root diameter of the actual screw (DK) is found reducing the original diameter by the clearance between the screw/screw clearance (s). The external diameter of the actual screw (DA) is found subtracting the barrel diameter by two times the screw/barrel wall

clearance (δ). The coordinates of the offset flank curve are calculated with reference to the derivative of f(x), as in Eq. 18 [35]:

$$f'(x) = \frac{2\pi\frac{\mathrm{DE}}{2}\sin\left(\frac{2\pi\left(x-\frac{KB0}{2}\right)}{T}\right)}{T} - \frac{\pi\left(\frac{\mathrm{DE}}{2}\right)^2\cos\left(\frac{2\pi\left(x-\frac{KB0}{2}\right)}{T}\right)}{T\sqrt{A^2-\left(\frac{DE}{2}\right)^2\sin\left(\frac{2\pi\left(x-\frac{KB0}{2}\right)}{T}\right)}} \tag{18}$$

The calculations for the actual profile coordinates ($x_a$, $y_a$) are expressed in Eq. 19, according to the region of the screw. KB1 is the tip width of the screw to be fabricated, which will be smaller than the tip width of the screw with self-wiping profile [35].

$$(x_a, y_a) = \begin{cases} (x, DK/2), & 0 < x \le \frac{KB1}{2} \\ \left(x + \frac{s}{2}\frac{f'(x)}{\sqrt{f'(x)^2+1}}, f(x) - \frac{s}{2}\frac{1}{\sqrt{f'(x)^2+1}}\right), & \frac{KB1}{2} < x \le \frac{T}{2\mathrm{Z}} - \frac{KB1}{2} \\ (x, DA/2)\ , & \frac{T}{2\mathrm{Z}} - \frac{KB1}{2} < x \le \frac{T}{2\mathrm{Z}} \end{cases} \tag{19}$$

The final coordinates ($x_{a,k}$, $y_{a,k}$) of the tip of the screw are found at the intersection with the flank curve. Since the $y_{a,k}$ value is known (DA/2), it can be used to determine the point in the self-wiping profile (x, y) that will lead to the intersection between the tip and flank of the offset curve. This is mathematically expressed by Eq. 20, and can be determined iteratively [35]:

$$DA/2 = f(x) - \frac{s}{2}\frac{1}{\sqrt{f'(x)^2+1}} \tag{20}$$

Once that point is known, its x-coordinate can be used to calculate the actual position ($x_{a,k}$) of the offset tip of the screw according to Eq. 21 [35].

$$x_{a,k} = x + \frac{s}{2}\frac{f'(x)}{\sqrt{f'(x)^2+1}} \tag{21}$$

The actual tip width, and tip angle (KB1, and KW1, respectively) can be determined by Eq. 22 and Eq. 23 [35].

$$KB1 = \frac{T}{Z} - 2x_{a,k} \tag{22}$$

$$KW1 = \frac{2\pi KB1}{T} \tag{23}$$

The previous equations show the dependence of the tip angle on the pitch. The effect is shown in Fig. 13. Strictly, the planar offset method should be applied to generate a new profile each time the pitch is varied. This can cause slight differences in the contact of elements with different pitches. On the other hand, using identical screw profiles results in congruent cross-section contours but leads to slightly varying flank clearances [35].

*Figure 13. Comparison between the self-wiping profile (external contour, in red) and two offset profiles with different pitch values: T/DE = 2 (middle contour, in blue), and T/DE = 0.4 (internal contour, in greed). In all cases, A/DE = 0.82, s/DE = 0.01, and δ/DE = 0.01*

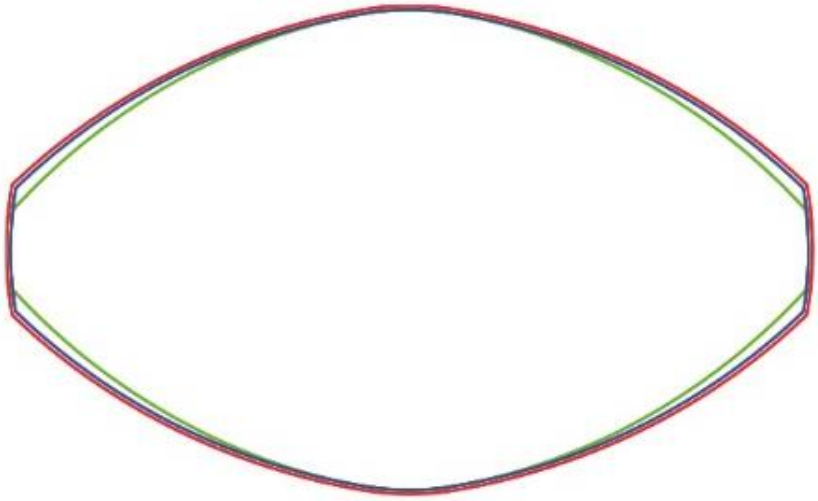

*Source: adapted from [37]*

### 2.2.2 Screw elements and their operating principles

Conveying elements and kneading blocks are the standard screw modules used in Co-TSE. Despite differing in shape and function, both element types share the same cross-section described previously [35].

Conveying elements (see Fig. 14) are continuous screw segments that draw the material into the extruder, transport it downstream (*i.e.* towards the die) or upstream (*i.e* backward), and compress it as needed. The conveying elements are defined by the number of flights, pitch, length, and thread direction. The nomenclature usually indicates respectively their pitch and total length, such as in 60/120. The thread direction can be right-handed (RH) or left-handed (LH) and is sometimes indicated [35].

*Figure 14. Forward and backward conveying elements.*

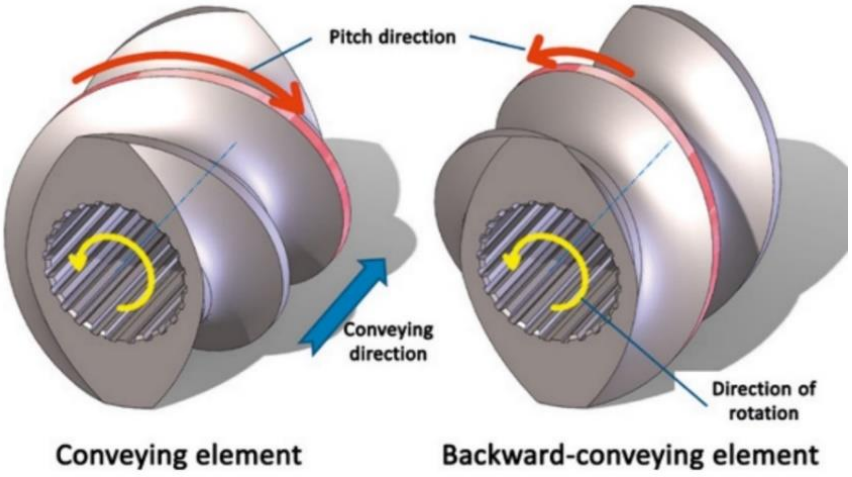


*Source: adapted from [35]*

Figure 15a shows the trajectory of the material in the conveying elements, which can be described as an open figure-eight pattern along the axis. At the intermeshing region, material is transferred from one screw to the other. Axial conveying occurs when the material is displaced between the screw tips, and tends to be less effective with double-flighted screws (Fig. 15b) compared to wide-tipped single-flighted profiles (Fig. 15c). As the material is conveyed, it is split into partial pools. The number of pools depends on the number of flights, which in turn affects the degree of material (re)distribution. The partial melt pools are represented in Fig. 15d [35,37,41].

*Figure 15. Flow trajectory along conveying elements: a) representation of the figure-eight pattern along the screw axis, b) and c) material displacement between double-flighted and single-flighted, d) partial flows created according to the number of flights.*

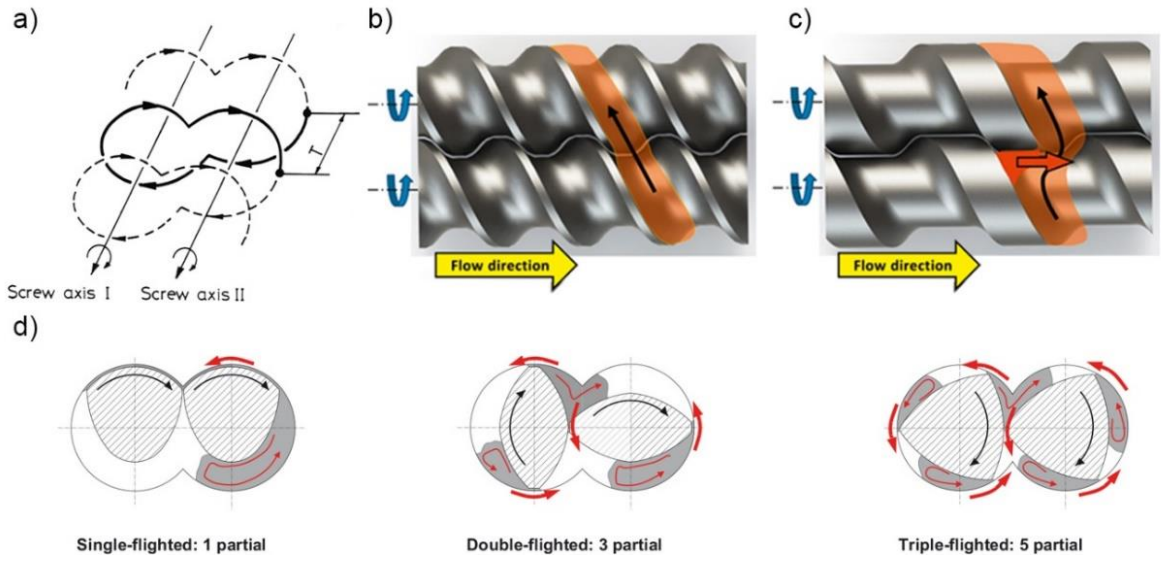


*Source: (a) adapted from [42], (b) and (c) adapted from [35], (d) adapted from [37]*

Although the free cross-section area and the free volume of the screw channels are independent of the pitch of the element, the pumping efficiency passes trough a maximum with increasing pitch. This happens because with small pitch values the width of the screw channels decrease and the transport routes become longer. In turn, with excessively large pitch values the helix angle tends to 90º and no conveying is possible for double-flighted screws. The pitch, thus, determines the degree of filling at a prescribed product throughput and screw speed [35].

To simplify installation and avoid discontinuities, the length of the conveying elements is often equal to a whole pitch or half a pitch. The modules are made symmetrical and congruent, so that it does not matter which end face enters the screw shafts first or which shaft their are installed [35].

Kneading blocks (see Fig. 16) comprise of prismatic discs that are offset with respect to one another, and are predominantly used for melting, distributive and/or dispersive mixing. The kneading blocks are defined by the staggering angle, number and width of discs, and total length [35].

*Figure 16. Representation of a kneading block.*

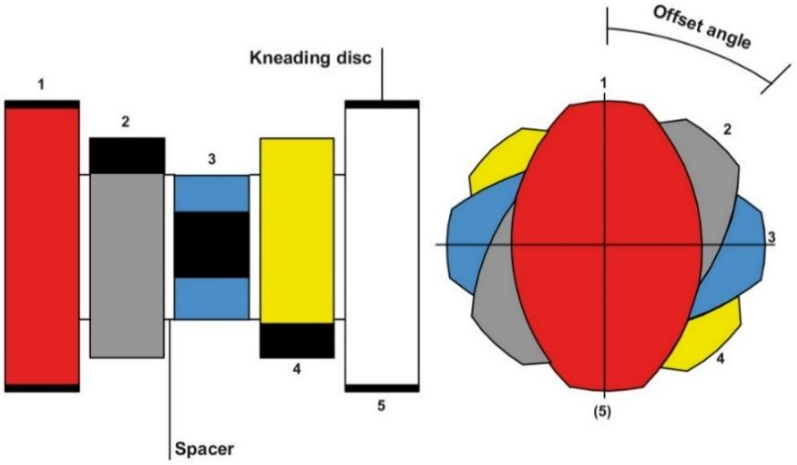


*Source: [37]*

As represented in Fig. 17, the kneading blocks present two flow channels. The melt can flow along the main conveying direction, between the tip of the discs, or through the tip of the discs, in which case kneading effectively takes place. The kneading blocks become more axially open with increasing staggering angles, thus resulting in reduced pumping efficiency. For double-flighted screws, neutral kneading blocks are created with the discs staggered by 90º. The width of the discs determines the chance of a flow element being forced in the kneading gap. Therefore, wide discs have a higher dispersive effect, while narrow discs induce distributive mixing [35].

*Figure 17. Flow channels developed in the kneading blocks.*

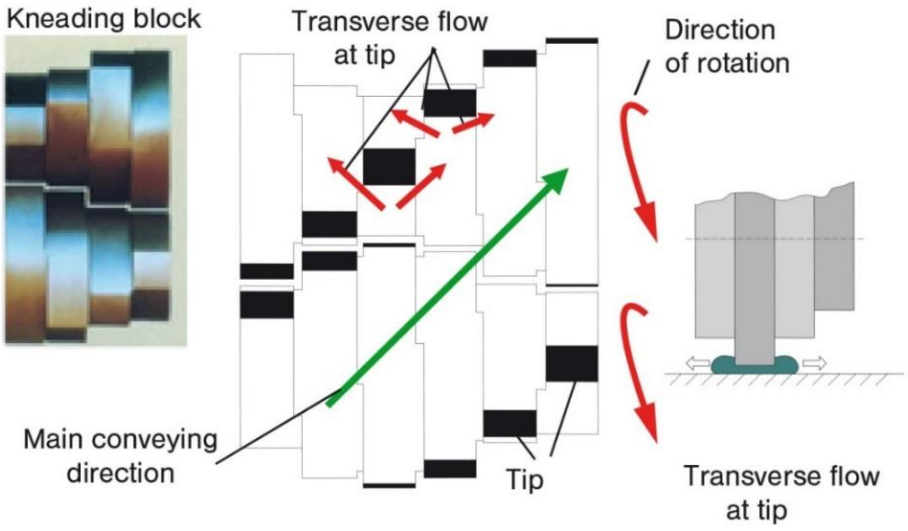


*Source: adapted from [37]*

Kneading blocks (KB) sometimes present spacers between the discs to guarantee the necessary clearance for operation [35]. The modules are usually named after their staggering angle, number of discs and total length, respectively, such as in KB 45/5/45. Reverse conveying kneading blocks can be indicated by negative staggering angles of by using the acronym LH [41,43].

A variety of special screw elements, such as blister rings, sealing discs, and gear mixers, to name a few, are available to provide specialized processing capabilities. Sometimes, the desired flow characteristcs are created at the cost of the self-wiping property. More information about these special elements can be found in Giles et al. [41] and in Kohlgrüber [35].

### 2.2.3 Processing zones in the Co-TSE

In Co-TSE, different functional zones can be created depending on the screw configuration, processing conditions, and material properties. The screws are often formed by individual segments that can be arranged into different combinations. Besides the barrel temperature profile, the processing conditions include the screw rotation speed, and the feed rate, *i.e.* the rate at which the material is metered into the extruder. As a rule, the Co-TSE operates under starve feeding conditions so that most of the screw is only partially filled [22,25].

The degree of starvation, as well as the type, number, and location of the functional zones can be controlled by changing the feed rate, screw rotation speed, and screw configuration. Thus, the Co-TSE offers remarkable operational flexibility allowing for adjustments of the manufacture line according to the specific product requirements [25,43].

Despite the virtually unlimited variety of extruder configurations, most machines used for polymer compounding will have at least five basic zones. Figure 18 illustrates a typical Co-TSE with intake or feeding zone, plasticating zone, melt conveying zone, mixing zone, and metering zone [41,35].

*Figure 18. Typical Co-TSE with two restrictive zones.*

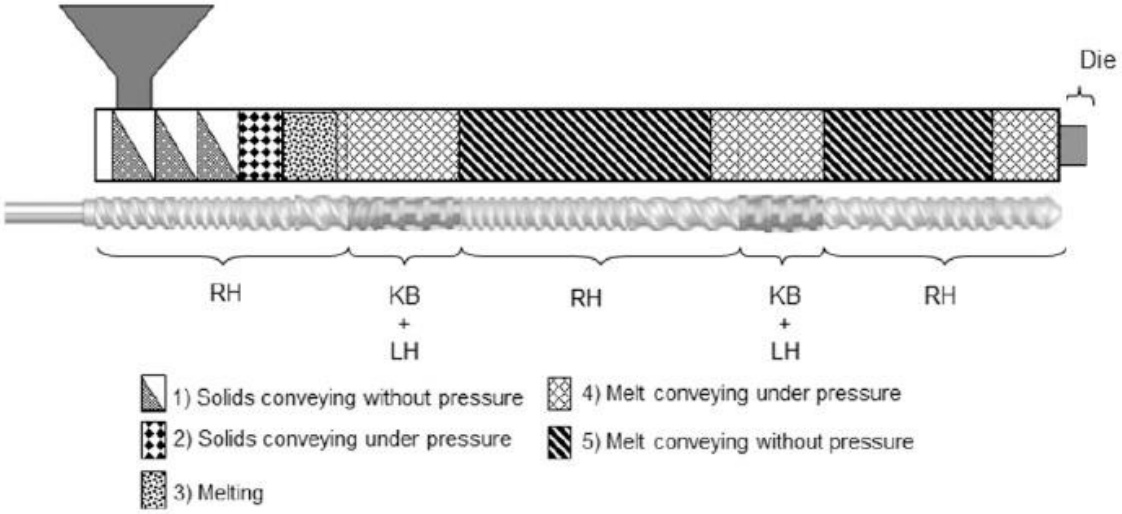


*Source: adapted from [25]*

At the intake zone, the solid particles of material are conveyed under starve feeding conditions. Starvation is achieved with the aid of a feeder, when the feed rate is smaller than the conveying capacity of the screw elements. As a result, the screw channels are partially filled. The flow depends on the geometry of the screw elements, as well as on the friction between the material and the barrel wall [22,35].

The length of the intake zone often varies from 4 to 6 diameters (DE), and the pitch of the first conveying elements is usually large, equal to 1.5 to 2 DE [35,41]. Short low-pitch conveying elements are sometimes used upstream to the actual feeding port, to prevent the material from flowing towards the screw seals [41].

The plasticating zone generally starts upstream the first restrictive elements with the formation of a melt film on the barrel wall, screw surface, or in the bulk. The local for melting initiation depends on the material properties and operating conditions [44]. A plastication mechanism similar to the one proposed by Tadmor for single screw extruders, *i.e.* with the progressive melting of a solid plug and formation of a melt pool, has been initially observed. However, bed instabilities ultimately cause the solid particles to become suspended in a melt matrix and their size reduces as melting advances [25]. This melting mechanism, represented in Fig. 19, is referred to as dispersed solids melting (DSM) [22].

*Figure 19. Dispersed solids melting mechanicsm.*

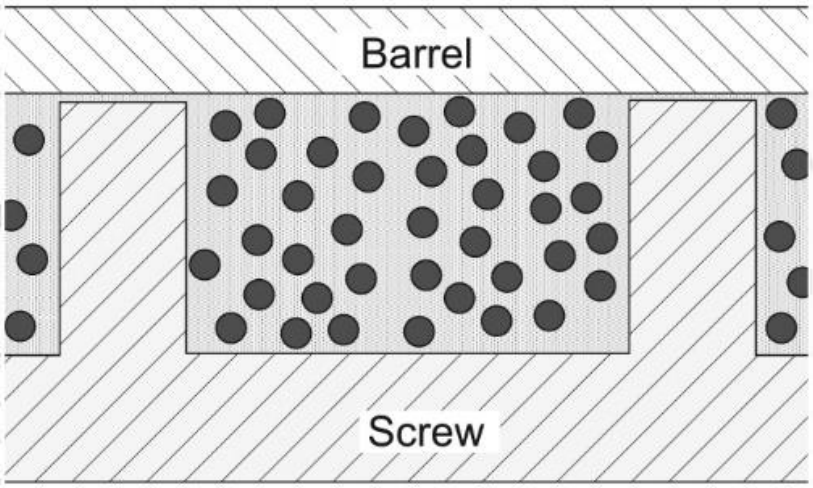


*Source: [22]*

Since the depth of the screw channels is constant, restrictive elements must be used to develop pressure and promote the formation of the melt film [25]. Reverse conveying or neutral kneading blocks are generally used for this purpose. The level of pressure build-up is defined by the pumping efficiency of these elements [35]. Reverse conveying screw segments are sometimes used to create a melt seal that prevent any air passing downstream the plasticating zone [41].

The DSM mechanism is activated when the volume fraction of the melt is about 40% or 50%. Melting in completed very quickly, often after a length corresponding to two or three times the screw diameter [22,25]. After the plasticating zone, the melt is conveyed forward first by fully filled kneading blocks and then in partially filled screw segments [35]. The intermediary conveying elements are also important to reduce/control the melt temperature, which might rise in the plastication zone due to the high shear generated by the restrictive elements [41].

Figure 20 shows the leakage flows over the screw tips, which can have a slight mixing effect and contribute to homogenize the melt at the melt conveying zone [35,41]. Conveying elements with pitch equal to 1 DE (referred to as square-pitched) are often used to minimize shear and reduce the pressure on the melt [35,41]. The melt conveying zone can also be used to feed additional materials directly to the melt, in which case elements with larger pitch should be used to increase the feed capacity [35].

*Figure 20. Simplified representation of the distributive mixing effect created by the leakage flows.*

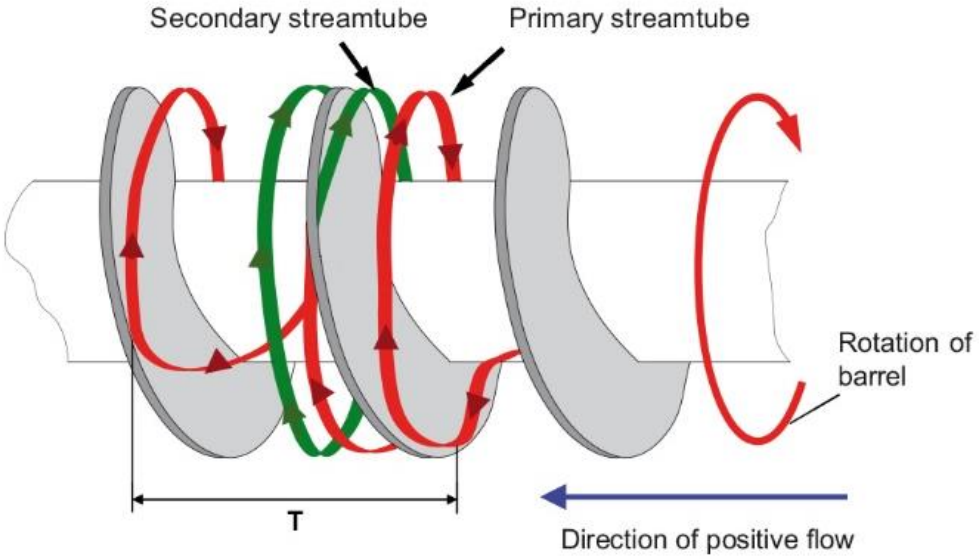


*Source: adapted from [37]*

The mixing zone can be made purely distributive or mostly dispersive [25]. Besides splitting the flow into multiple streams over the kneading discs and reorienting the flow in the intermeshing zone, the restrictive nature of the kneading blocks is crucial to subject the melt to repeated deformation cycles, exerting a distributive effect [35]. When dispersive mixing is required, the kneading discs shall be wider (see Fig. 21a ), so that more material is forced over the flights where it is subject to high shear and extension rates (Fig. 21b) [37,41].

*Figure 21. Mixing with kneading discs: (a) effect of the disc width, (b) locations where the shear and extensional flows are developed.*

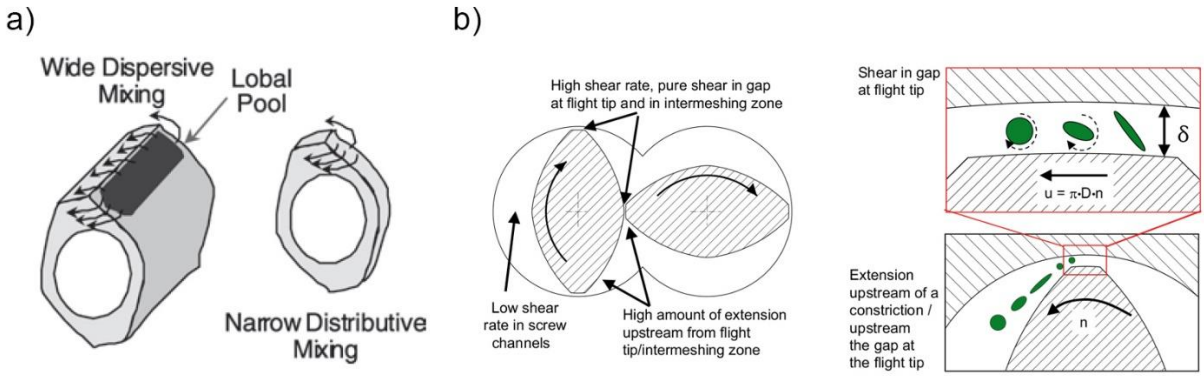


*Source: (a) [41], (b) [37]*

The mixing quality is often related to the kinematic parameter of flow, a dimensionless indicator of the operational status of the screw elements. The kinematic parameter of flow (Λ) is expressed by Eq. 24, in function of the volumetric flow rate ($\dot{V}$), the inherent throughput ($A_1$), screw rotation speed (N), and screw diameter (D) [35].

$$\Lambda = \frac{\dot{V}}{A_1 N D^3} \tag{24}$$

When Λ > 1, the screw is overrun, meaning that the output (determined by the feed rate) is higher than the conveying capacity of the screw element. In this condition, the material is pushed through the screw channels by a pressure gradient. When Λ = 0, there is no flow and, thefore, the local residence time is infinite. Negative values of Λ are possible with left-handed elements, when the melt is conveyed backward. The relationship between the kinematic parameter of flow and the quality of distributive and dispersive mixing is shown in the graphs from Fig. 22 [35,37].

*Figure 22. a) Influence of the kinematic parameter of flow (Λ) on the degree of distribution, and b) influence of Λ and viscosity on the dispersion degree*

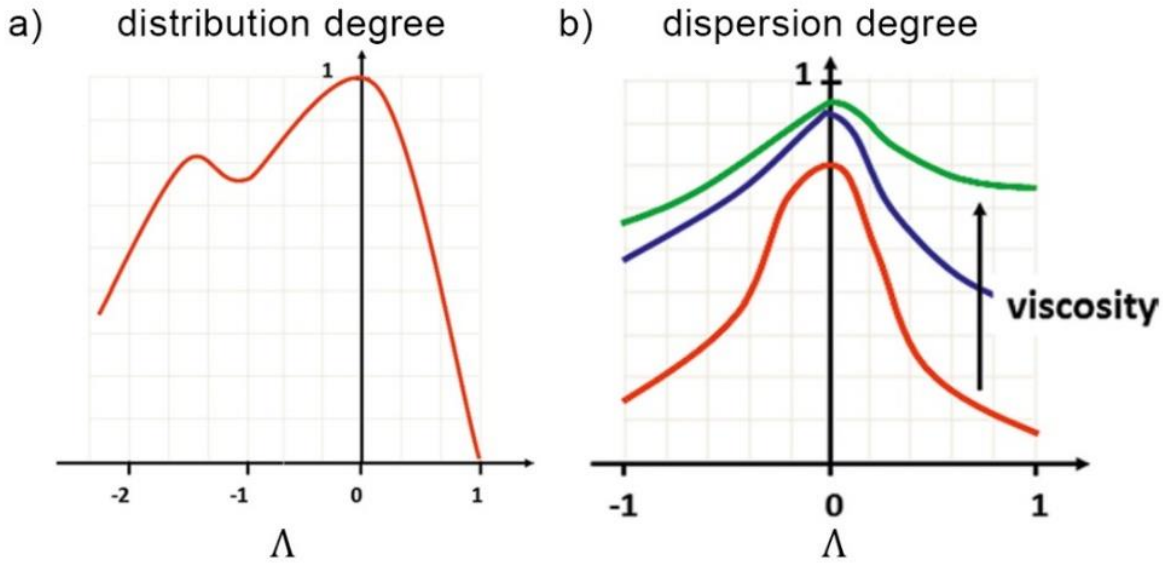


*Source: adapted from [35]*

As shown in Fig. 22a, the quality of distributive mixing declines markedly as Λ increases. Homogenization is theoretically complete for Λ = 0, since the number of flow reorientation cycles tends to infinity. It is also evident that distributive mixing is favoured for values of Λ < 0, *i.e.* under back conveying conditions. The relation between Λ and the quality of dispersive mixing (Fig. 22b) follows the same general trend, although the improvement of the dispersion degree under backwards conveying conditions is less pronounced. Again, the best condition is achieved at Λ = 0, since the duration of the loads is theoretically infinite. The effect of the matrix viscosity is also considered, showing that dispersion is enhanced under higher viscosity levels [35]

At the metering zone, sometimes referred to as discharge zone, the pressure consumed by the die exit has to be generated. The pressure build-up capacity is again related to the pitch of the conveying element. Low-pitch screw segments are often used in this zone to generate the required pressure consuming less energy in a shorter length [35,41]. At least part of the metering zone may operate fully filled, resulting in additional mixing due to the leakage flows over the screw tips. Since the extruder is operated under starve feeding conditions, the resulting output depends only on the selected feed rate [35].

## 2.3 Material extrusion additive manufacturing

Material extrusion (MEX) is defined as the "additive manufacturing process in which material is selectively dispensed through a nozzle or orifice" [2]. Similar to other AM techniques, MEX encompasses a series of stages. These generally include the convertion of a virtual computer-aided design (CAD) description file to a standard tessellation language (STL) file, which is then digitally sliced and transformed into computer numerical control (CNC) codes according to the printing settings defined by the user. The CNC codes are used in the actual building stage, which is often followed by post-processing operations [5,45].

In the building stage, the volumetric primitives (*i.e.* extrudates or roads) are generated and deposited onto the build surface. Material dispensing involves continuous feeding, melting, and flow control, while the dispenser itself and the build platform move in relation to each other at least in three axes [3,5]. Although both functions are fully integrated during the 3D printing process, each one is performed by independent units. The next topics describe how material dispensing and 3D deposition are typically implemented in filament-fed MEX systems.

### 2.3.1 Material dispensing

The first dispensing solution for MEX was disclosed in the Stratasys' FDM® (fused deposition modelling) patent, filed in 1989. As shown in Fig. 23, the FDM® print head consisted of a heated reservoir into which a thermoplastic filament was continuously fed with the aid of counter-rotating pinch rollers. The polymer was readily melted in the reservoir and then pressurized against the deposition nozzle by the incoming solid filament [46].

*Figure 23. Elevation view of the material dispensing apparatus utilizing a flexible strand as supply material.*

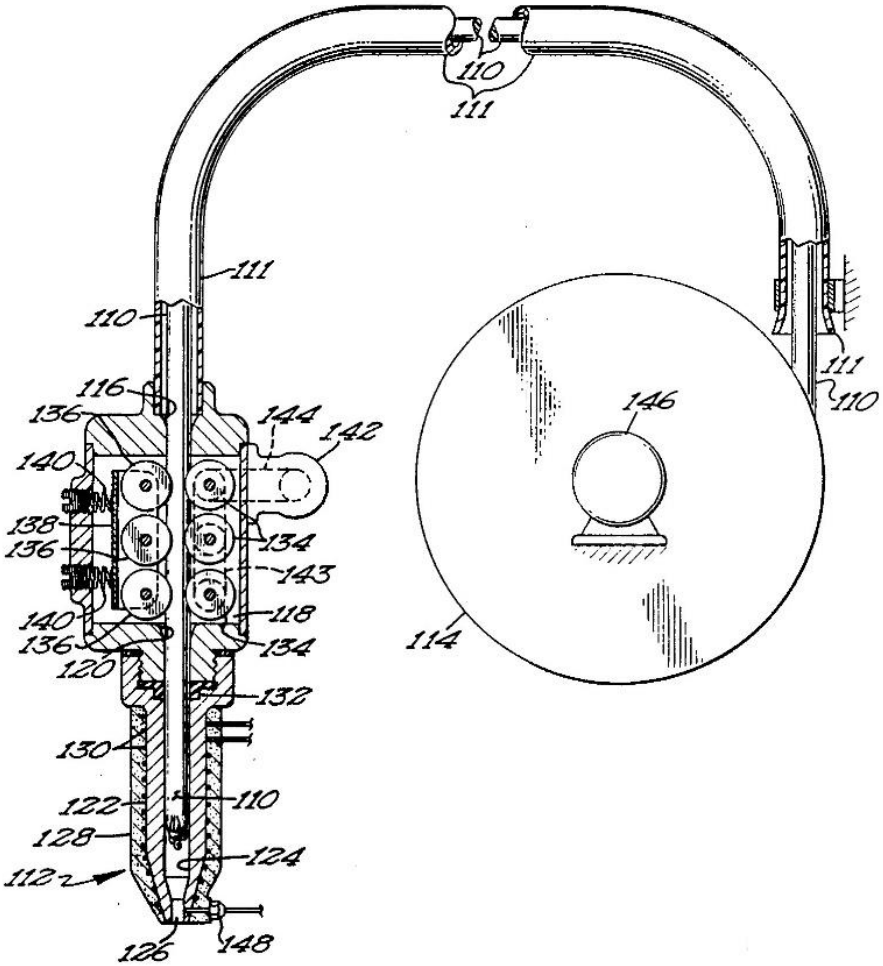


*Source: adapted from [46]*

The FDM® print head was, therefore, analogous to a simplified piston-based extruder, with feedstock and dispenser design adapted to provide continuous extrusion as long as the thermoplastic filament could be supplied. Considered an entry-level technology to the AM world, filament-based 3D printing became increasingly accessible under the generic term FFF (fused filament fabrication) with little modifications after the original patent expired in 2009 [3].

Firstly, adequate feeding is key for material dispensing. The filament diameter is usually 1.75 mm and must be as constant and possible so that the pinch rollers can effectively pull it. As illustrated in Fig. 24, the feeding mechanism can be positioned directly over the heated reservoir (referred to as direct drive); or it can be fixed to the 3D printer structure, in which case a polytetrafluorethylene (PTFE) tube is used to guide the filament (referred to as Bowden extruder) [47].

*Figure 24. Schematics of a FFF 3D printer with a) direct drive and b) Bowden extruder feeding mechanism*

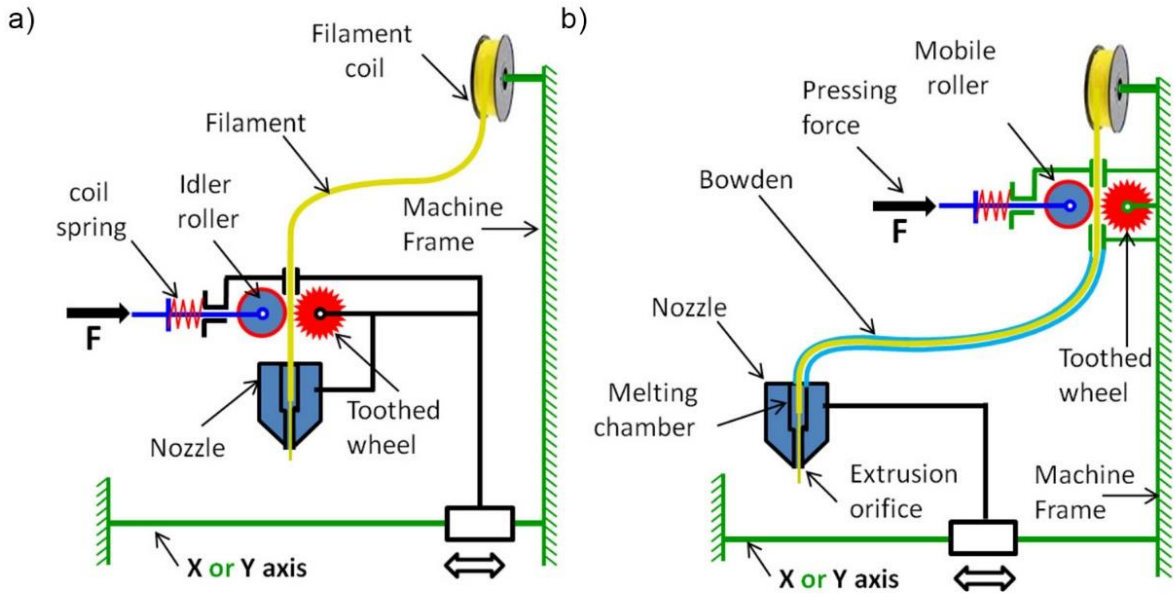


*Source: adapted from [47]*

Filament buckling can be expected as the feedstock is compressed inside the print head. The critical compression stress ($\sigma_{cr}$), expressed by Eq. 25, is a function of the elastic modulus (E) of the material, filament diameter ($d_f$), and filament length ($l_f$) measured from the pinch-rollers to the entry of the heated reservoir [48].

$$\sigma_{cr} = \frac{\pi^2 E d_f^2}{16 l_f^2} \tag{25}$$

The feeding mechanism is also responsible to generate the required extrusion pressure ($\Delta p$), which can be estimated by Eq. 26 in terms of the apparent melt viscosity ($\eta$), volumetric flow rate ($\dot{V}$), length ($L_n$) and radius ($r_n$) of the nozzle [48,49].

$$\Delta p = \frac{8\eta \dot{V} L_n}{\pi r_n^4} \tag{26}$$

Since the extrusion pressure should be smaller than the critical blucking stress, a fundamental printability criterion with reference to the elastic and rheological properties of the material can be suggested. As expressed by Ineq. 27, if the rigidity is too low or the viscosity is too high [6], the necessary extrusion pressure cannot be achieved before the filament buckles or breaks at the entrance of the heated chamber [48].

$$\frac{E}{\eta} > \frac{8\dot{V}L\left(\frac{l_f}{d_f/2}\right)^2}{\pi^3 r_n^4} \quad (27)$$

Filament bucking and/or rupture, particularly when printing with elastomeric materials [50] or highly filled polymers [6], are more common with the direct extruder design. With the Bowden extruder, the filament might curl around the pinch rollers or be ground in contact with their grooved surfaces.

Material dispensing also depends on the melting or plastication capacity of the print head. A detailed representation of the so-called hotend (where melting takes place) is shown in Fig. 25. Usually, a cartridge heater and a thermistor are inserted into the aluminum block placed around the brass nozzle [51].

*Figure 25. Representation of the FFF hotend.*

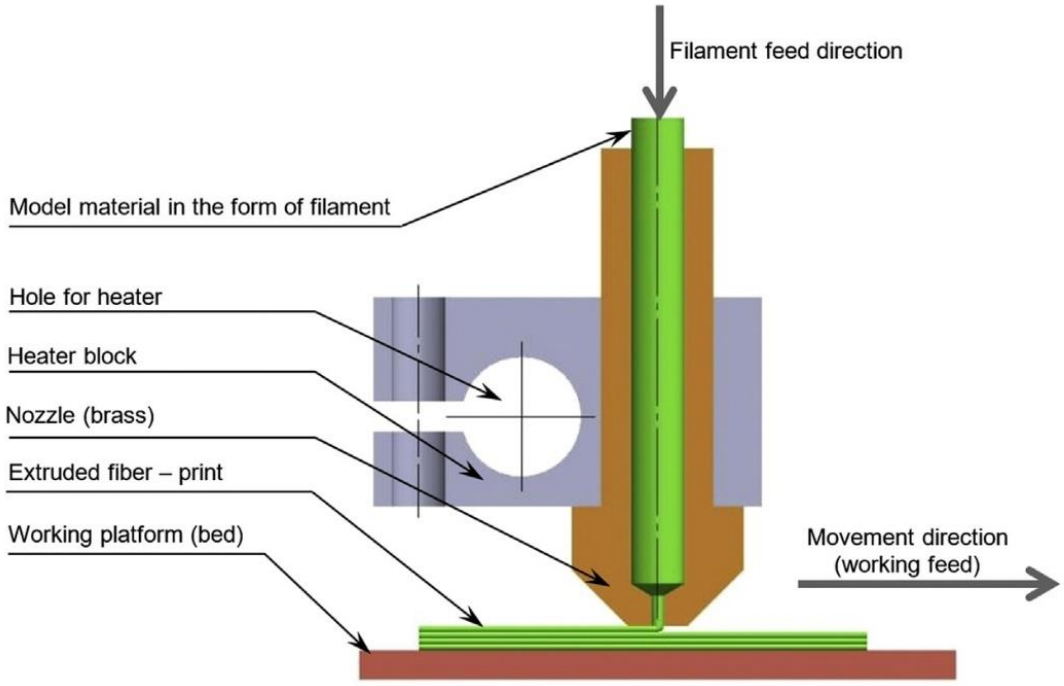


*Source: [51]*

Polymer melting is completely performed by the heat transfer from the heating element through the aluminum block and nozzle. The required heat flux (q) can be estimated by Eq. 28, in function of the material density (ρ), volumetric flow rate ($\dot{V}$), specific heat capacity of the material ($C_p$), the inlet and outlet temperatures ($T_i$ and $T_0$, respectively), and the enthalpy change ($dH_m$) in the case of a semicrystalline polymer [48].

$$q = \rho\dot{V}C_p(T_0 - T_i) + (dH)_m \quad (28)$$

The available heating power is generally around 40 W, meaning that the feasible feed rate and the maximum temperature that can be achieved are limited. Again, insufficient heating will result in feeding problems due to the excessively high viscosity. Thus, high temperature polymers or composites are often problematic to print [6].

The final aspect of material dispensing relates to the flow control. In the FFF machines, the volumetric extrusion rate ($\dot{V}$) is simply determined by the feed rate ($F_R$) and filament diameter ($d_f$), as expressed in Eq. 29 [48].

$$\dot{V} = \frac{F_R \pi d_f^2}{4} \tag{29}$$

In practice, the dispenser is treated as an additional motion axis and, for a given filament diameter, the volumetric flow rate is calculated by the slicer application in terms of the linear velocity of the pinch rolers ($v_{in}$) and length of filament ($l_e$) entering the print head [52]. The relationship is expressed by Eq. 30.

$$\dot{V} = v_{in} l_e \tag{30}$$

As exposed, the main characteristics of the FFF print head (*e.g.* reduced dimensions, low weight, and components simplicity) make it very easy to operate. Besides, since the feedstock itself generates the extrusion pressure, prompt control over the material flow can be achieved. In fact, the filament is often retracted to interrupt material dispensing, an important feature to achieve high precision when printing more complex shapes.

### 2.3.2 3D indexing

As the molten thermoplastic is deposited (see Fig. 26), the cylindrical extrudate must be redirected by 90º from the vertical dispenser to the build surface [48,49], where is expected to spread and assume an oblong cross-section geometry.

*Figure 26. Deposition parameters for typical MEX platforms.*

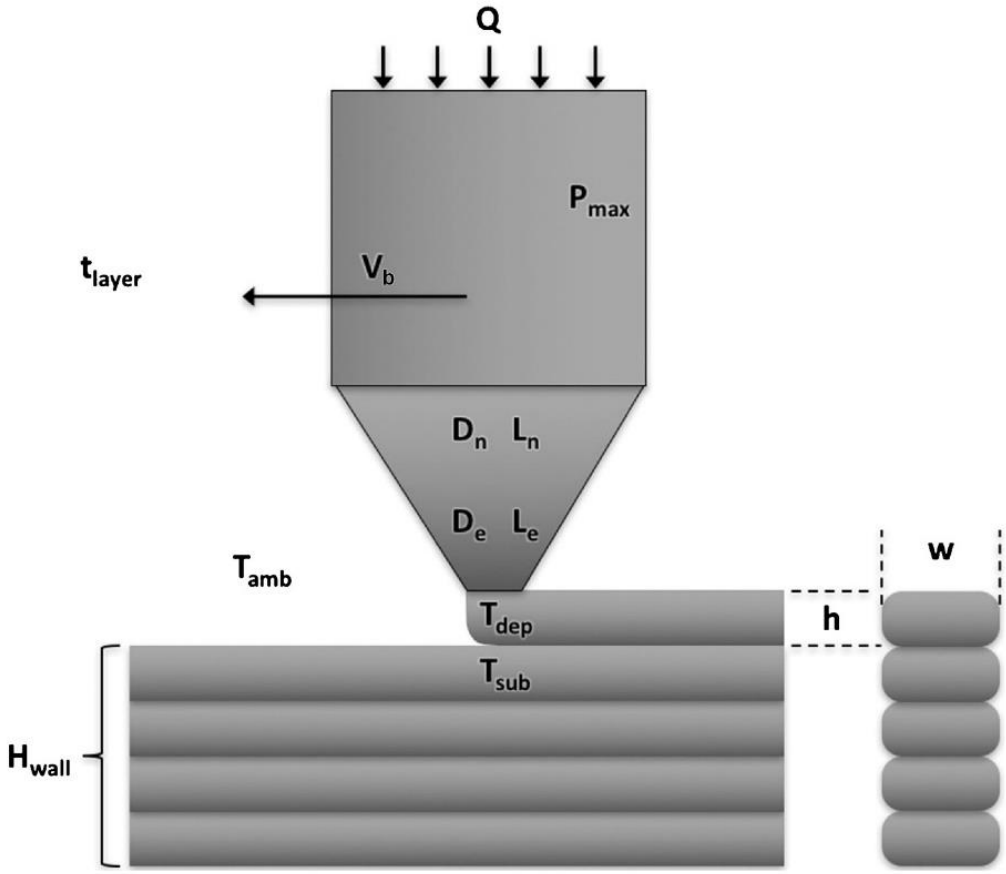


*Source: adapted from [49]*

The volumetric flow is controlled in relation to the user-specified deposition speed ($v_d$), as well as the expected road width (w) and height (h) [48,49]. Usually, the optimum layer height is less then or equal 75% the nozzle diameter ($h \leq 0.75\ d_o$) [53]. The slicer adjusts the velocity and length of the filament being fed to the print head ($v_{in}$ and $l_e$, respectively) based on a simplified rectangular bead cross-secton [54]. The relashionship between the variables is expressed by Eq. 31.

$$v_d w h = v_{in} l_e \tag{31}$$

The deposition trajectory, called toolpath, consists of a series of coordinate locations that describe the contour and filling patten for a given layer of the part under construction. The toolpath is generated according to user-specified slicing parameters typically following a contour-and-raster strategy, so that the external features of the part can be preserved [3,5]. The multiple toolpaths generated with a common rectilinear filling pattern are illustrated in Fig. 27.

*Figure 27. Toolpaths necessary to fill a circular geometry with a rectilinear pattern.*

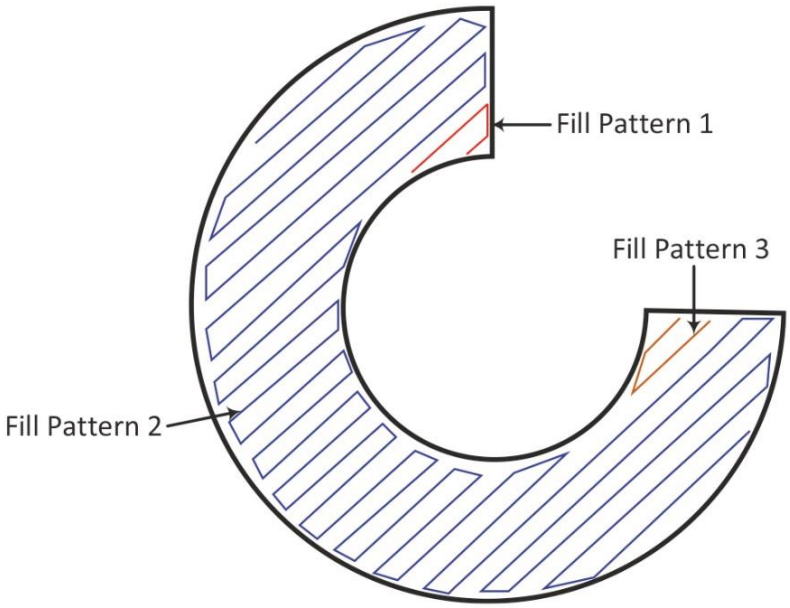


*Source: [5]*

From a closer look, the toolpath corresponds to the trajectory of the center of the circular nozzle. The specific area to be filled is discretized with relation to the nozzle diameter and, as a result, unfilled gaps are created between the deposited roads, weakening the printed parts. The size of the voids can be reduced by allowing the roads to overlap each other, at expense of precision as illustrated in Fig. 28 [3,5].

*Figure 28. Infill patterns to a) maximize precision and b) maximize strength*

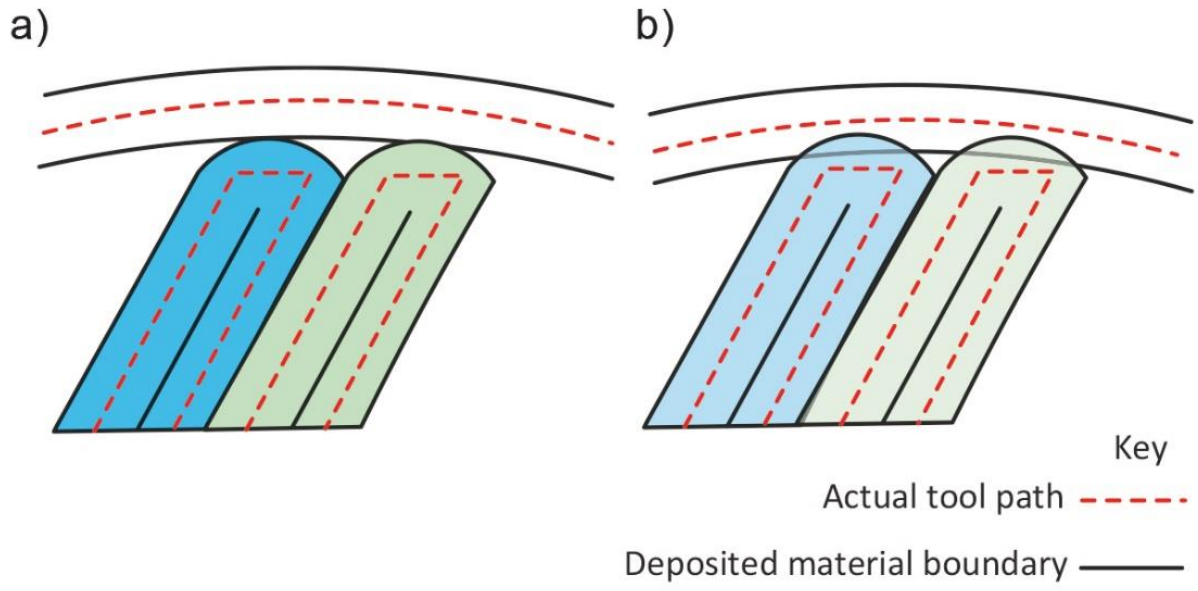


*Source: adapted from [5]*

Although the deposition direction can be identical for every layer, it is often preferred to use weaving patterns such as in composite materials to achieve the best mechanical properties [5]. The weaving pattern is defined by the raster angle set up for each layer. Besides the geometry of the roads (which define the raster width and layer height) and raster angle, other basic printing parameters involved in the toolpath generation include the contour thickness, and raster gap [55]. The mentioned parameters are schematized in Fig. 29.

*Figure 29. Typical MEX 3D printing parameters.*

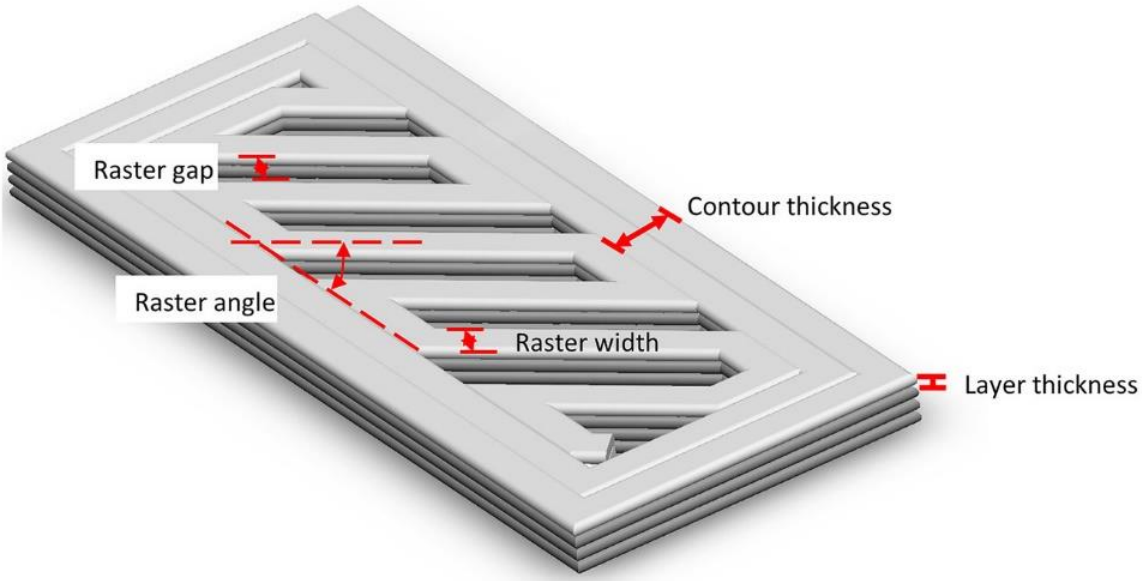


*Source: adapted from [55]*

After the paths for every layer have been created, they are translated into g-code, which can be considered the standard CNC programming language used in FFF [56,57]. The g-code, therefore, encompasses the information about the amount of material to be deposited, infill pattern, movement speeds (printing, and travel), and the temperatures (extrusion, and build platform) [52].

With respect to the hardware, 3D deposition is enabled by a positioning system integrated to the machine structure. Most filament-based 3D printers adopt a 3-axis Cartesian positioning system, with the print head scanning the horizontal plane and the build platform moving in the vertical direction [5]. Alternative implementations based on the polar coordinate system (polar 3D printers), 3- or 6-axis with parallel kinematics (delta 3D printers), and three or more axes with serial kinematics (robot arms) are also available. The mentioned positioning systems are illustrated in Fig. 30 [58].

*Figure 30. Available designs for the positioning system of MEX 3D printers.*

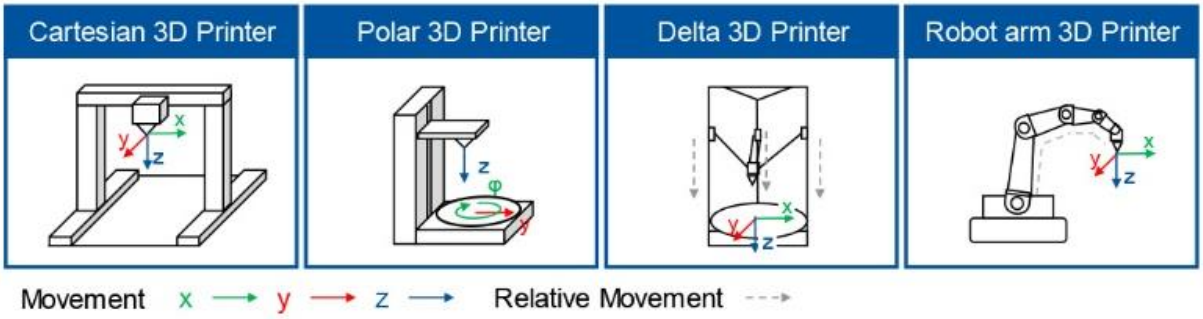


*Source: [58]*

The connection between the g-code generated by the slicing software and the electromechanical components of the 3D printer is mediated by a controller board. With the consolidation of the RepRap movement, Arduino® has become the microcontroller of choice for most applications. A customized electronic board (RepRap Arduino Mega Pololu Shield, or RAMPS family) is available to be integrated to the Arduino Mega 2560. The microcontroller is often loaded with the Marlin firmware, which interprets the g-code to control the motors and heaters, and process the signals coming from the different sensors [59].

# 3 SYSTEMATIC REVIEW ON SCREW-ASSISTED MEX

Screw-assisted material extrusion additive manufacturing (SA-MEX) first appeared in the mid-2000s. The main objective was to enable 3D deposition directly from pellets or granules, widening the range of materials that could be processed face the limited variety of filamentary feedstock available in the market. With time, the SA-MEX systems started to be customized for different objectives, including improved control over the extrusion process, higher deposition speed, and to enable large-scale 3D printing at reasonable costs.

Although the single screw extrusion technology is currently well developed, its adoption in the context of MEX is not straightforward. The extruders used in the polymer industry typically present diameter larger than 40 mm, length-to-diameter ratio (L/D) greater than 18, and usually operate with screw speeds above 100 rpm. Besides, heat transfer efficiency is substantially altered by the extruder's area-to-volume ratio [60]. These factors can represent advantages but also bring challenges to the implementation of SA-MEX.

In this chapter, the evolution of SA-MEX is investigated in a narrative review following the guidelines presented by Siddaway et al. [61]. The search method is presented in the first section, followed by the description and analysis of the results in the second section. The chapter ends with a discussion about the generalities of the research performed with SA-MEX systems as well as a brief commentary on the differences between the miniaturized extruders and the single screw extruders typically used for polymer processing.

## 3.1 Search method

The systematic review covered only original research articles published between the years 2000 and 2020, in journals indexed in the Science Direct, Scopus, and Web of Knowledge databases. Although paste-like materials and inks have been processed in screw-assisted print heads, the scope of the review was narrowed to the systems that could be fed with particulate solids. The search strings are presented in Table 1.

*Table 1. Search strings used according to the electronic database.*

| | STRING 1 | STRING 2 |
|---|---|---|
| Science Direct | (ALL: (Additive Manufacturing) AND TITLE, ABSTRACT, KEYWORDS: ((3D Print) AND Extrusion AND Screw) | (ALL: (Material Extrusion Additive Manufacturing) AND TITLE, ABSTRACT, KEYWORDS: ((3D Print) AND (Pellet OR Powder OR Granule OR Particle)) |
| Scopus | (ALL: (Additive Manufacturing) AND TITLE, ABSTRACT, KEYWORDS: ((3D Print*) AND Extrusion AND Screw)) | (ALL: (Material Extrusion Additive Manufacturing) AND TITLE, ABSTRACT, KEYWORDS: ((3D Print) AND (Pellet OR Powder OR Granule OR Particle)) |
| Web of Knowledge | (TOPIC: (Additive Manufacturing) AND TOPIC: (3D Print) AND Extrusion AND Screw) | (TOPIC: (Material Extrusion Additive Manufacturing) AND TOPIC: ((3D Print) AND (Pellet OR Powder OR Granule OR Particle)) |

*Source: the author*

The search results were stored and the duplicates eliminated using an online reference manager (Endnote®, Clarivate Analytics). Three initial screening criteria were considered when reading the articles' title, abstract, and keywords: (1) the additive manufacturing process should be based on MEX; (2) material conveying, melting, and pressurization should be performed in the print head; (3) the print head should be fed directly with solid particles. The pre-selected articles were then read thoroughly, and only those which presented functional equipment (*i.e.* used in actual processing/deposition experiments) were qualified. Further articles meeting the selection criteria that were cited in the qualified documents or that were previously known but still uncovered by the search results were added to the repository.

The flowchart from Fig. 31 represents the search process and shows the resulting number of documents after each step.

*Figure 31. Flowchart of the systematic search, showing the resulting number of articles after each step.*

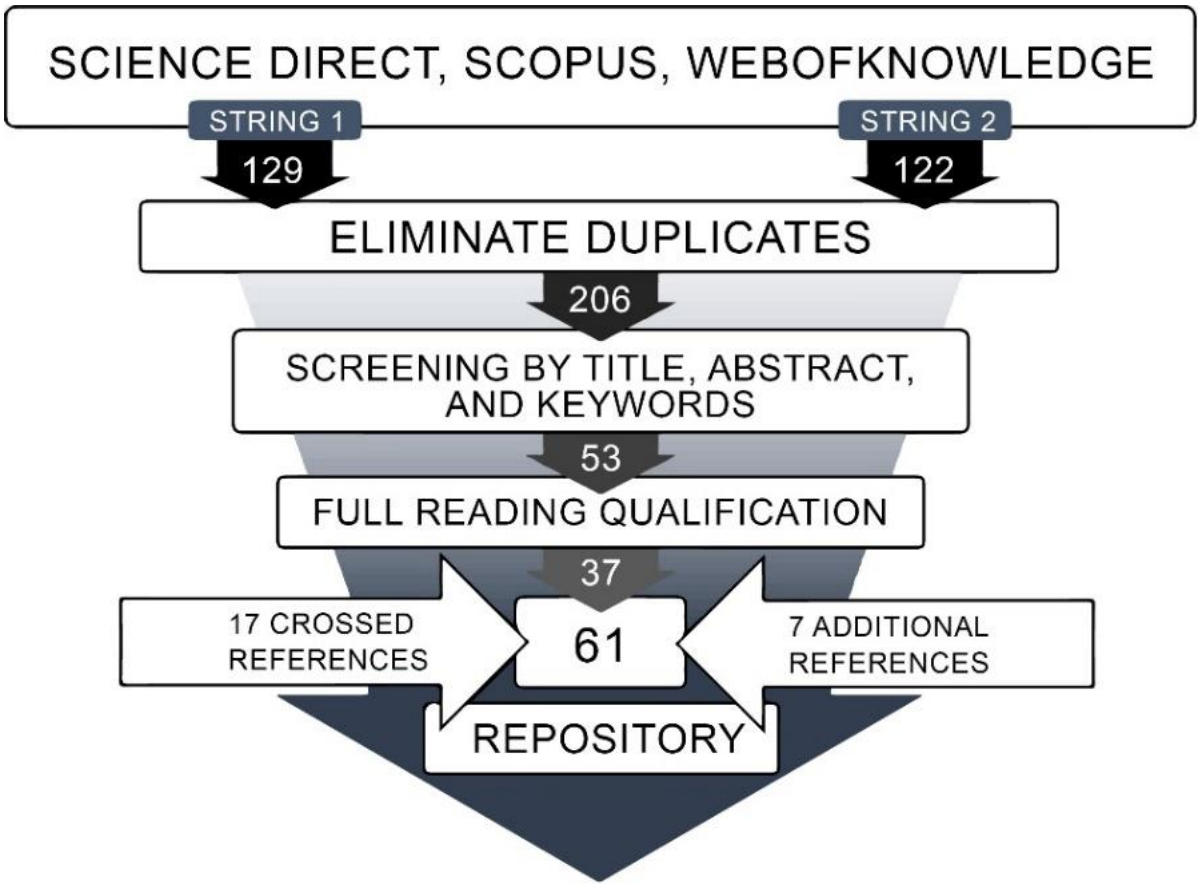


*Source: the author*

## 3.2 Results

Table 2 and 3 lists the small-scale and large-scale SA-MEX systems identified in the search. The experimental equipment is referred by the name of the first author, while commercial systems are denoted by the models' name. The numbers in brackets indicates the publications related to each table entry. The data used to classify the application scale include design details (nozzle diameter, maximum printing volume, and screw diameter), and the values used for the main process parameters (screw rotation speed, and deposition speed). In general, the nozzle from small-scale systems was smaller than 1 mm, the printing volume reached up to 300 × 300 × 300 mm, and the screw diameter was not larger than 17.5 mm. The deposition speed ranged from 1 to 30 mm/s. For large-scale systems, the nozzle ranged from 0.8 to 10.1 mm, with printing volume starting at 800 × 600 × 600 mm, and screw diameters up to 25 mm. The deposition speed was often higher than 20 mm/s, reaching up to 279 mm/s.

*Table 2. Selected information about the small-scale SA-MEX systems.*

| Denomination | Nozzle diameter (mm) | Screw diameter (mm) | Maximum printing volume (mm) | Screw rotation speed (rpm) | Deposition speed (mm/s) |
|---|---|---|---|---|---|
| Bellini [62-64] | 0.25, 0.3, 0.4 | n/i | n/i | n/i | 20 |
| Reddy et al. [65] | 0.55 | n/i | n/i | n/i | n/i |
| Lam et al. [66] | n/i | n/i | n/i | n/i | n/i |
| Silveira et al. [67,68] | 0.4 | 7 | n/i | 7.5 | 12 |
| Annoni et al. [69] | 0.6, 0.9, 1 | n/i | n/i | n/i | n/i |
| Canessa et al. [70] | n/i | n/i | n/i | n/i | n/i |
| Liu et al. [71-75] | 0.33, 0.5 | n/i | n/i | 2.5, 5, 10, 11, 12, 15 | 2.4, 2.6, 2.8, 20 |
| Jackson et al. [76] | 2.5 | 17.5 | n/i | 5-10 | 1 |
| Kumar et al. [50, 77-82] | 0.8 | n/i | 210 x 210 x 288 | 50-75 | 24 |
| Singamneni et al. [83,84] | 0.5, 1, 1.5, 2 | 14 | n/i | 1300 | 9-18 |
| Tseng et al. [85] | 0.4 | 14 | n/i | 30 | 370 |
| Whyman et al. [86,87] | 0.8, 1.5 | 15 | n/i | 7.3 | 10 |
| Zhou et al. [88] | n/i | 12 | n/i | 70 | n/i |
| Boyle et al. [89] | 0.4 | n/i | n/i | n/i | n/i |
| Leng et al. [90] | 0.4 | n/i | n/i | 20 | 70 |
| Khondoker, Sameoto [91] | 0.35, 0.5, 1 | 15.5 | n/i | 3-6 | 30 |
| Alexandre et al. [92] | 0.8 | 8 | 220 x 220 x 180 | n/i | 40 |
| Kim, Lee [16] | n/i | n/i | n/i | n/i | 30 |
| Liu et al. [93] | n/i | 8 | n/i | 8 | 3.3-6.7 |
| Wang et al. [10] | 0.25 | n/i | n/i | 5.6-16.8 | 5 |
| 3D Discovery® [11,12, 94-96] | 0.33 | n/i | 130 x 90 x 6 [50] | 22 | 20 |
| PAM® [97] | 0.4, 1 | n/i | Ø300 x 300 [52] | 100, 250 | 20-30 |
| M3DIMAKER® [19] | 0.8 | n/i | n/i | n/i | 90 |
| Exam255® [15] | 0.3 | n/i | 255 x 255 x 255 [55] | n/i | n/i |

*Source: the author*

*Table 3. Selected information about the large-scale SA-MEX systems.*

| Denomination | Nozze diameter (mm) | Screw diameter (mm) | Maximum printing volume (mm) | Screw rotation speed (rpm) | Deposition speed (mm/s) |
|---|---|---|---|---|---|
| Hertle et al. [98,99] | 2 | 16 | n/i | n/i | 36-40 |
| Brooks et al. [100] | 0.8, 1.2, 3.2 | n/i | n/i | 2.5, 4, 11 | n/i |
| Liu et al. [101] | 4 | 25 | 800 x 600 x 600 | 0-30 | 20-30 |
| Magnoni et al. [102,103] | 2 | n/i | n/i | 400, 650, 900 | 15, 20, 25 |
| Schmidt et al. [104] | 3 | 14 | n/i | 10-100 | 20 |
| BAAM® [56,105-110] | 5.1, 7.6, 10.1 | 25 | 6000 x 2400 x 1800 | 50 | 85-279 |
| Gigabot X® [9,111-113] | 1.75 | n/i | 580 x 600 x 470 [74] | n/i | 5-30 |
| Super Discovery® [114] | 5 | n/i | 1300 x 2500 x 1000 [76] | n/i | 50 |

*Source: the author*

In the next topics, a general analysis of the publications is provided, followed by a detailed description of the small- and large-scale SA-MEX systems identified by the search. The equipment are presented according to the year of their respective publications. Information about the extruder design, market availability (*i.e.* experimental or commercial), and main results presented in each publication is provided.

### 3.2.1 General analysis

Figure 32 presents the evolution of the number of publications throughout the years, according to the application scale and market availability. The initial publications described only experimental small-scale systems [63-66]. The first commercial system intended for small-scale applications was described in two publications from 2016 [94,95], the same year when an experimental system for potential large-scale application was introduced [56]. The first commercial large-scale system was described a year later, in two articles from 2017 [105,106]. Many new experimental systems for small and large-scale applications appeared in the period from 2014 to 2018 [67-80,83,85,86,88], reflected by the number of publications in the same period. Although the scientific production in the last 2 years decreased, a crescent share of the

research was carried out with commercial systems [9,11,12,15,19,97, 107-110,112,113,114], indicating the consolidation of SA-MEX in the market.

*Figure 32. Number of publications per year according to the application scale and type of system described.*

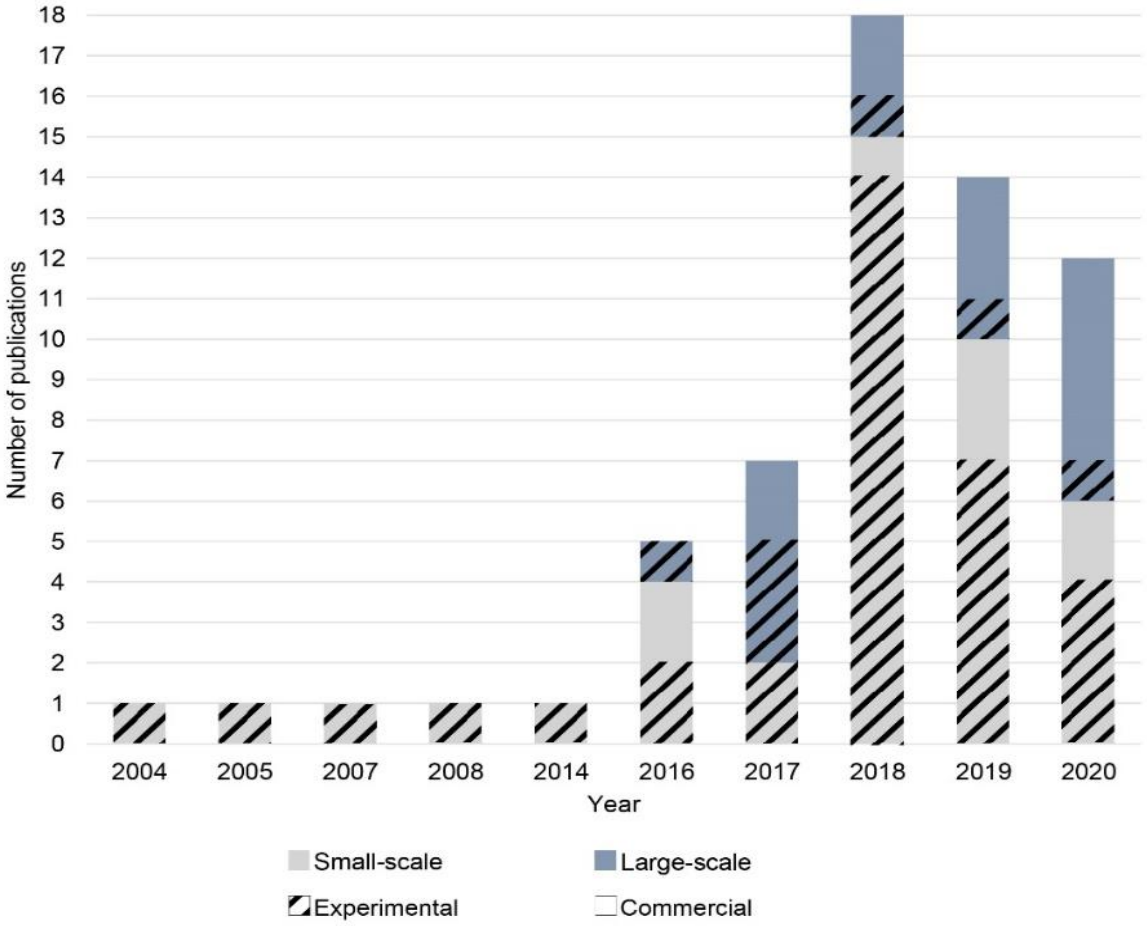


*Source: the author*

The co-occurrence of keywords was analysed with aid of the VOSviewer software, after correcting spelling differences and merging synonyms. In addition, abbreviated terms were replaced by their corresponding full equivalents. Figure 33 shows the resulting network, in which the size of the circles is proportional to the frequency of each keyword; while the width of the links indicate how often two keywords were used together. The keywords appearing together in a publication are positioned close to each other in the map.

*Figure 33. Network map of the co-occurrence of keywords.*

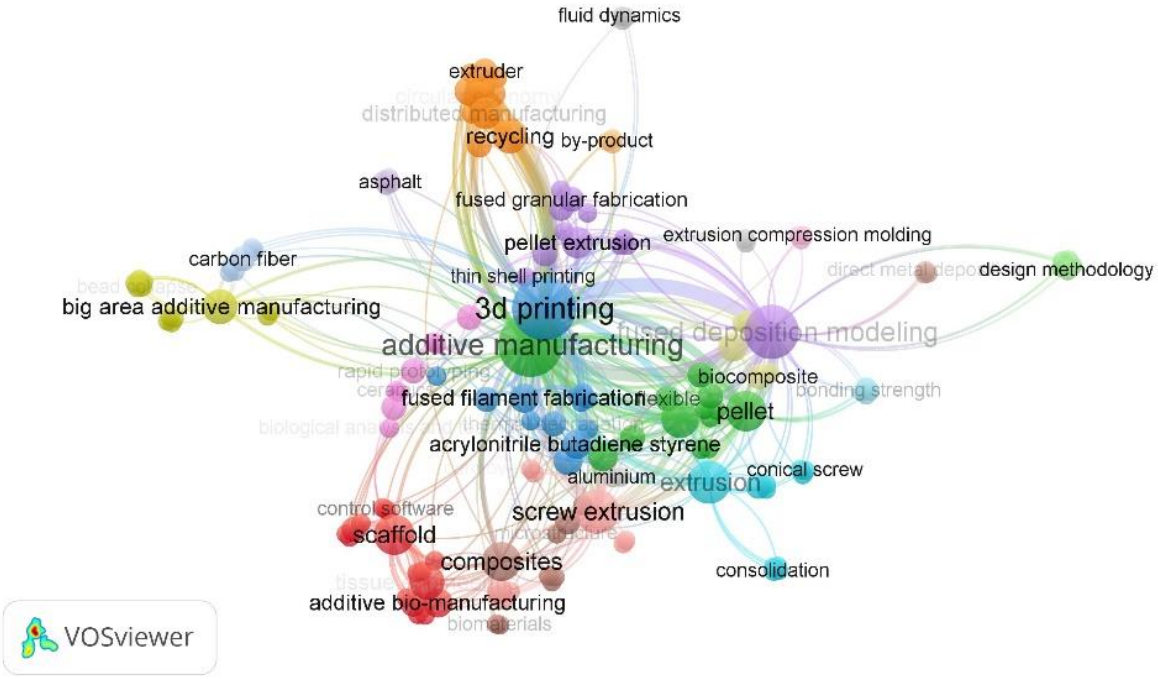


*Source: the author*

The most frequent keywords were "additive manufacturing" and "3D printing," both occurring 29 times, followed by "fused deposition modeling," occurring 18 times. The clusters in red, yellow, and orange, in which the most frequent keywords were respectively "scaffold" (occurring 8 times), "big area additive manufacturing" (occurring 5 times), and "recycling" (occurring 5 times), relate to the three main topics of interest (*i.e.*, bio-AM[1], large-scale AM, and recycling AM). Other prominent clusters revolve around the terms "screw extrusion" (10 times), "extrusion" (9 times), "pellet" (8 times), and "composites" (7 times).

The technological evolution of SA-MEX is shown in a timeline that organizes the various experimental print heads and commercial systems according to the year when they were first described in the literature (Fig. 34). The notation is the same as used in the tables 2 and 3.

[1] Additive bio-manufacturing, *i.e.* "*3D printing for medical purposes or non-therapeutic 'human enhancement', whether they involve the production of biological material or not*" [115]

*Figure 34. Timeline of the development of the screw-assisted MEX systems.*

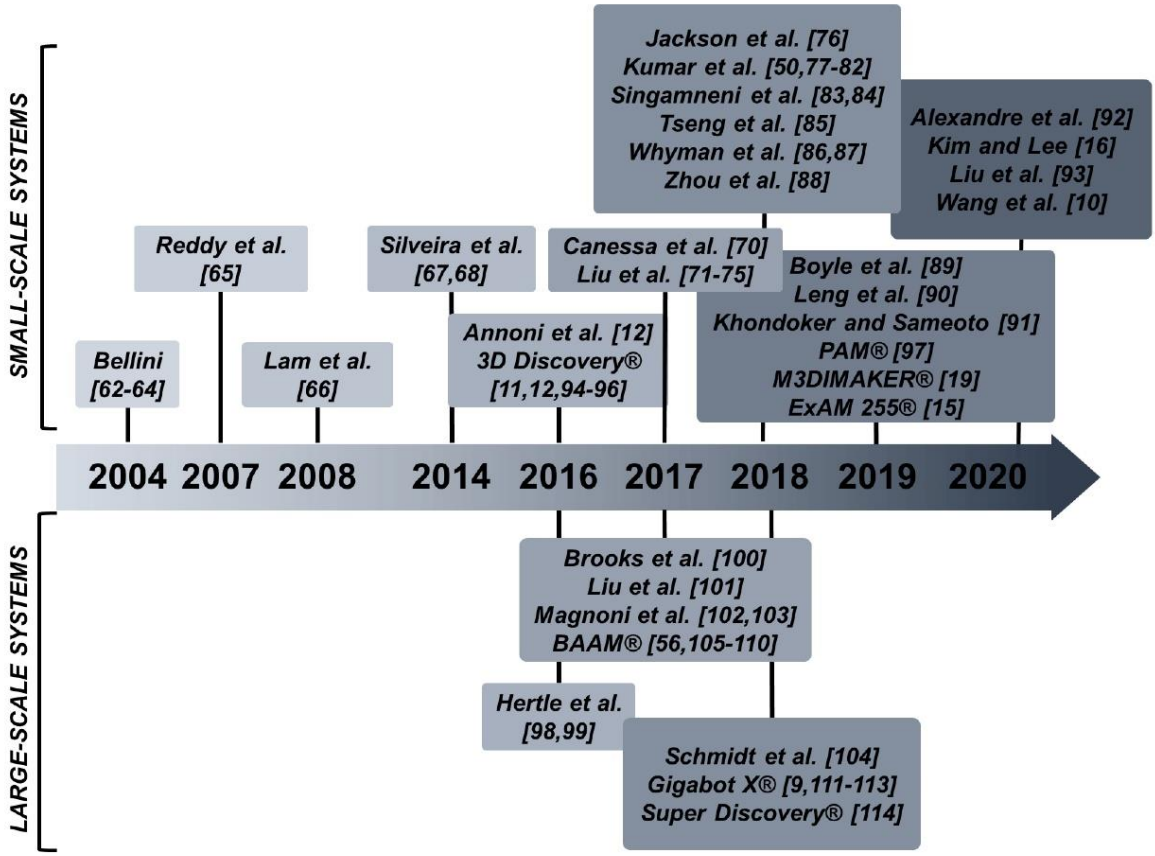


*Source: the author*

As indicated by the timeline, the first SA-MEX systems appeared in the years from 2002 to 2008 [62-66], coinciding with the decade when low-cost filament-fed desktop machines and alternative syringe-based print heads were developed [116]. Although the first systems were mostly used for bio-AM applications [63,66], the concept was further developed from 2014 to 2019 to different purposes [69,70,88,90,91]. An expressive equipment variety for small-scale applications could be observed in that period, including four commercial systems (3D Discovery® [94,95], PAM® [97], M3DIMAKER® [19], ExAM 255® [15]). Besides the description of the first do-it-yourself (DIY) kit for a screw-assisted print head [92], no significant innovations were introduced in 2020.

Large-scale SA-MEX started timidly only by 2016, with experimental setups adapting benchtop-sized industrial extruders to different positioning systems. Positioning systems based on robotic arms have been considered in 2017 [100,102], due to their higher degree-of-freedom and potentially larger printing volume. The most innovative system incorporated a first plasticating stage followed by a reciprocating screw used to control the extrusion flow [101].

The first commercial system (BAAM® [105]) was introduced in the same period. New large-scale systems were last introduced in 2018, with two commercial machines (Gigabot X® [111], Super Discovery® [114]) with no significant modifications in terms of extruder design.

### 3.2.1 Small-scale systems

Figure 35 shows the general design of the pioneering print heads developed by Bellini [62], and Reddy et al. [65].

*Figure 35. Schematic illustrations of the pioneering screw-assisted print heads: a) developed by Bellini [62], and b) developed by Reddy et al. [65].*

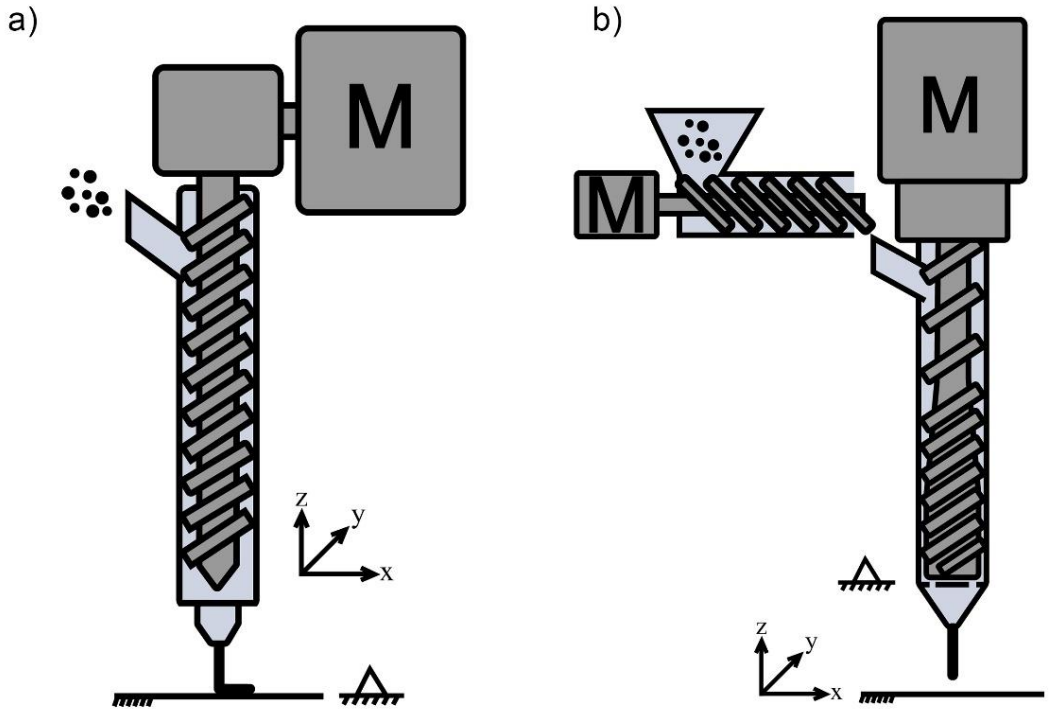


*Source: the author*

Bellini's print head established the vertical layout of the extruder, which would become standard for a variety of equipment to come [62]. The material was fed manually into an inclined port, and a screw without compression profile (*i.e.* constant pitch or channel depth) was used. The barrel was heated in its intermediary portion and closer to the interchangeable nozzle. The print head moved in the three directions thanks to a custom-made desktop positioning system, while the build platform was fixed [64]. The system`s performance was initially assessed with relation to the processing temperature, nozzle geometry, and deposition velocity using ceramic materials. According to the authors, some level of agglomeration as well as air entrapment were observed within the deposited structures [64]. The equipment was later used to fabricate biopolymer-based scaffolds [63].

To overcome the feeding problems described by Bellini et al. [64], the print head developed by Reddy et al. [65] included a separate feeder and an extrusion screw with compression profile. A support similar to a breaker plate was also included to avoid screw deflection due to uneven radial pressure. The resulting print head was fixed, while the build platform moved in the three directions. Test specimens were fabricated directly from polymer pellets under different processing conditions.

Another early development was found in Lam et al. [66], which developed a print head to process biocomposites and 3D print scaffolds. Multi-material mixing followed by 3D deposition in a single processing route was reported for the first time. However, no details about the extruder layout and screw design were provided.

The basic design of the print heads developed by Bellini [62] and Reddy et al. [65] was further explored by Silveira et al. [67], Jackson et al. [76], Singamneni et al. [83,84], Tseng et al. [85], Zhou et al. [88], Leng et al. [90], Alexandre et al. [92], and Wang et al. [10]. Except for the print head developed by Jackson et al. [76], all equipment adopted a screw with compression profile. Silveira et al. [67], Jackson et al. [76], and Alexandre et al. [92] integrated their extrusion units to low-cost desktop 3D printers. In contrast, Tseng et al. [85], Singamneni et al. [83], and Wang et al. [10] constructed their own positioning systems.

The smallest screw diameter (7 mm) was found in the extrusion unit developed by Silveira et al. [67], which was used to process waste laser sintering powders and biocomposites, the latter use to print tissue engineering scaffolds [68]. Biocomposites were also explored by Singamneni et al. [83,84], but in this case, the materials were previously mixed and pelletized. Nozzles with increased diameter were used to avoid material clogging. Tseng et al. [85] designed their print head to process pellets of highly viscous polymers, and added infrared (IR) heaters over the build platform to prevent delamination and warping. The largest screw diameter (17.5 mm) was used in the print head developed Jackson et al. [76], to process crude petroleum pellets. Both the screw and housing could be fabricated in acrylic resin by a stereolithography process, since the extrusion temperature was relatively low. Alexandre et al. [92] replaced the FFF print head from a low-cost 3D printer with a DIY screw-extruder kit, marketed by a recently founded company. The equipment was tested with virgin and recycled polymer pellets, as well as shredded plastic waste. Wang et al. [10] did not detail their print head, which apparently had no significant innovations. Their positioning system included a mechanism to

rotate the build platform around the x-axis, so that biopolymer-based cardiovascular stents could be fabricated.

Figure 36 shows three print heads with slight modifications from the basic extruder design described so far. Instead of a typical extrusion screw, Kumar et al. [50] appropriated from a drill bit attached to the spindle head of a CNC milling machine, devising a straightforward solution to the complex problem of screw design and fabrication. Zhou et al. [88] used a screw without compression profile, but included four feeding ports at different heights along the barrel to allow multi-material feeding and better control over the process residence time. In turn, Leng et al. [90] designed a conical screw to achieve improved plastication and better material homogenization over a shorter length.

*Figure 36. Schematic illustrations of the most significant modifications to the basic design of the vertical extrusion units proposed by a) Kumar et al. [50], b) Zhou et al. [88], and c) Leng et al. [90].*

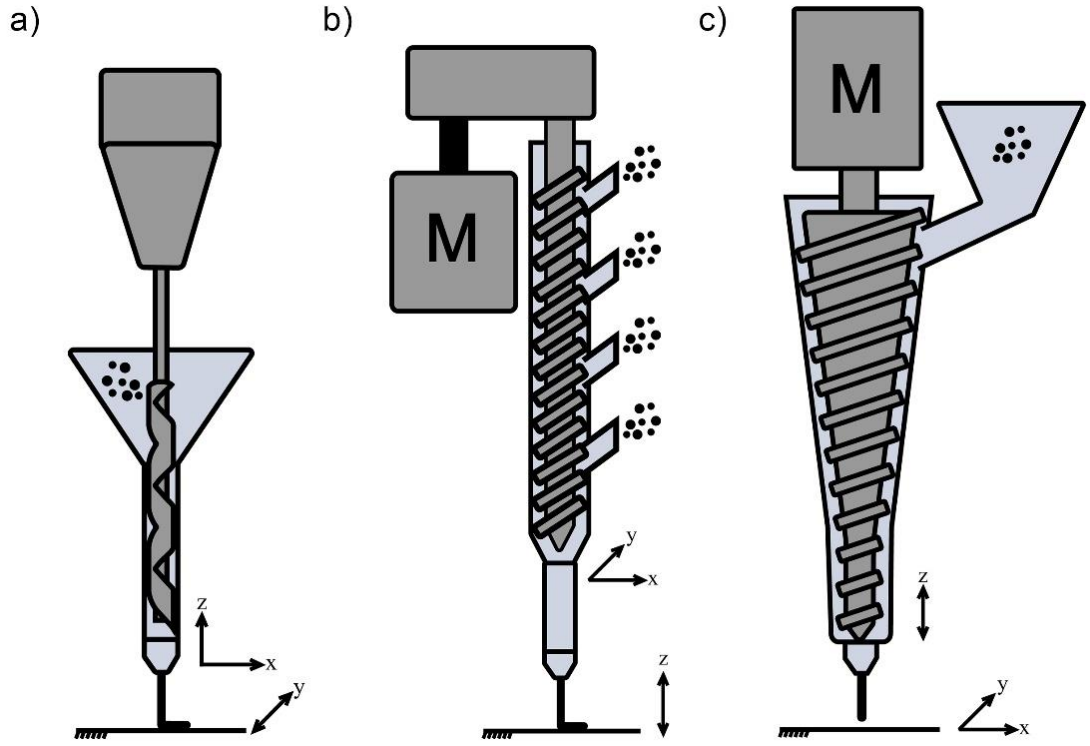


*Source: the author*

Many articles describing the feasibility of the extrusion unit developed by Kumar et al. [50] were published. Pellets of various materials, including neat polymers and composites were processed [77-82]. The idea of using a drill bit was also explored by Whyman et al. [86], which included a separate pellet feeder to prevent the drill from stalling. The print head was integrated into a custom-built positioning system. Pellets of a biopolymer and of a polymer blend were processed [87]. Boyle et al. [89] used a drill bit to construct the open-source Rich Rap Universal

Pellet Extruder (RRUPE), intended to recycle defective polymers parts. Although 3D printed parts could be produced, Whyman et al. [86], and Boyle et al. [89] reported material clogging in the drill and inconsistent feeding during the calibration experiments, respectively. A similar print head using a drill bit was developed by Kim, Lee [16], which was then integrated into a low-cost 3D printer. Pellets made of ceramic materials and polymer binders were used to fabricate test specimens and porous green parts (*i.e.* parts that require debinding and sintering to achieve their final properties) [117].

The print head developed by Zhou et al. [88] was integrated into a 3D Touch® (BitsFromBytes, Bristol, UK) printer. The screw was fabricated by a powder bed fusion AM process, followed by manual polishing. Pellets of heat-sensitive material were processed to determine the adequate screw rotation speed with relation to the printing parameters. Using the downstream feeding port, the material could be extruded with no significant thermal degradation. A benchmarking model was 3D printed to assess the dimensional accuracy provided by the equipment. Multi-material printing was also explored by adding fluorescent particles to the melt.

Leng et al. [90] exposed the theory behind the advantages of the conical screw with relation to plastication capacity. However, the dimensions of the extruder components were not provided. A self-developed positioning system was used. Test specimens could be fabricated from polymer pellets under different conditions while keeping fixed the screw rotation speed. The capacity to 3D print geometries of different levels of complexity was also demonstrated.

Figure 37 shows the most alternative print head designs found by the systematic search, which involve more than one mechanism. Annoni et al. [69] appropriated from a small injection molding machine, composed of an inclined plasticating screw and a vertical piston-assisted injection unity. Canessa et al. [70] added a progressive cavity pump (a.k.a. Moineau pump) downstream the extrusion screw, to achieve improved control over the material flow. Liu et al. [71] integrated an auxiliary liquefying chamber to their screw-assisted print head, to pump the molten material to the extrusion screw. Khondoker, Sameoto [91] developed a two-stage print head, which consisted of a fixed horizontal screw extruder that was connected to a typical FFF head.

*Figure 37. Schematic illustrations of the alternative small-scale screw-assisted print head designs developed by a) Annoni et al. [69], b) Canessa et al. [70], c) Liu et al. [71], and d) Khondoker, Sameoto [91].*

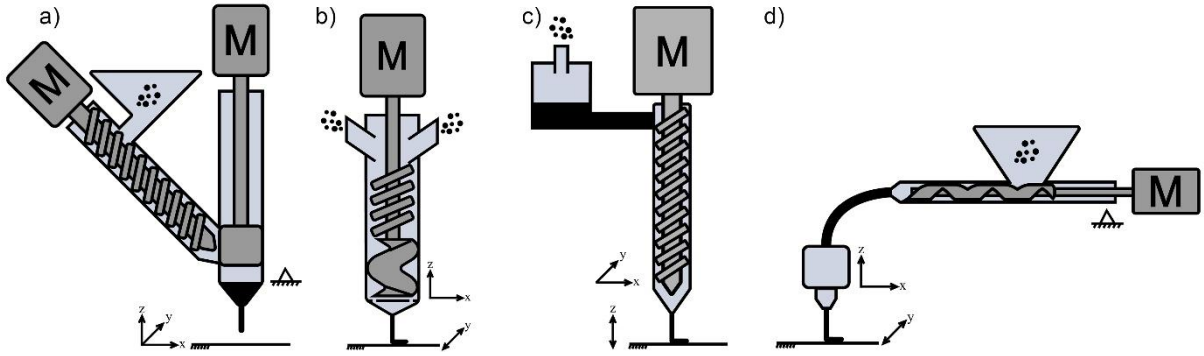


*Source: the author*

Annoni et al. [69] explored direct MEX of metals and ceramics from injection molding (IM) feedstocks. The pellets had expressive contents of solid particles and, therefore, required an extrusion unit capable to generate high pressure. Due to its weight, the extruder was fixed and a custom-made delta positioning system was used. The build platform could move in 3 directions, as well as rotating around 2 axes. Although extrudability tests were performed to investigate the influence of the binder percentage and geometry of the nozzle, no actual 3D part was built.

Canessa et al. [70] did not provide much information about the design of the extrusion screw, since their focus was on the design of the Moineau pump to achieve precise control over the material flow rate. The concept would circumvent the need for retraction strategies, allowing intermittent deposition even with continuous material feeding. The print head was integrated into a RepRap 3D printer, and validated with different materials.

The 3D printer developed by Liu et al. [71] included a multi-technological deposition tool that presented two piston-driven dispensing unities, a screw extruder, and a plasma jetting unity. No information about the screw design was provided. Each print head was indexed by rotational movement, and the whole assembly was integrated into a custom-made Cartesian positioning system. The equipment was used to fabricate scaffolds from pellets of neat polymer [72-75] and biocomposites [72,75], the latter being previously prepared by manual mixing processes.

In contrast to the previous print heads, the alternative design proposed by Khondoker, Sameoto [91] decouples the inherent limitations imposed by the weight and inertia of the screw extruder from the speed and resolution requirements of the deposition head. The extrusion unit consisted of a DIY kit (Filastruder®, Snellville, USA), which used a drill bit as screw. The FFF

head was connected to the screw extruder using a heated hose, and the assembly was integrated into a low-cost 3D printer. Printing feasibility was demonstrated with pellets of elastomeric materials. A similar system was described by Liu et al. [93], employing a custom-made extruder. A screw with compression profile was used. In addition, an impregnation mold was coupled to the die of the extruder, to generate a pre-impregnated filament that could be fed to the FFF head. The print head was mounted on a custom-made Cartesian system. 3D printing with continuous fiber-reinforced composites was demonstrated.

As shown in Fig. 38, four commercial small-scale SA-MEX systems were found by the systematic search. The 3D Discovery® machine, marketed by RegenHU (Villaz-St-Pierre, Switzerland), is a multi-technological biofabrication platform that incorporates up to six print heads, including a piston unity and a screw extruder. The Pellet Additive Manufacturing® (PAM) system is marketed by Pollen AM (Ivry-sur-Seine, France), and presents four pellet-fed screw extruders. The M3DIMAKER® pharmaceutical 3D printer, marketed by FabRx (London, UK), can print from filaments or powders, in which case the screw extruder is used. The ExAM 255® 3D Printer, marketed by AIM3D GmbH (Rostock, Germany), presents two screw extruders that can print from highly-filled pellets.

*Figure 38. The four commercial small-scale 3D printer with screw-assisted printheads found in the systematic search: a) 3D Discovery®, b) PAM® Series P, c) M3DIMAKER®, and d) Exam255®.*

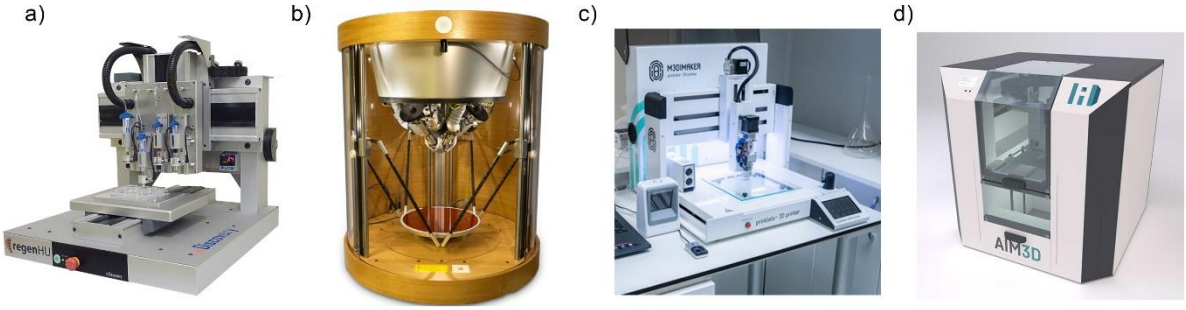


*Source: (a) [118] , (b) [119], (c) [120], (d) [121]*

The print heads from the 3D Discovery® are mounted on a Cartesian positioning system and move on the XZ plane while the deposition surface moves on the y-axis. The screw-assisted extrusion unity is very similar to the one described by Liu et al. [71], in which the pellets are first melted in a heated chamber and then air-pumped to the screw channels. The 3D Discovery® was used to fabricate scaffolds from different biocomposites [11,12,94-96]. In all cases, the biocomposites were previously prepared by manual melt mixing and then pelletized. According to the authors, screw processing was essential to further distribute the solid particles in the molten polymer [11,12,94-96].

The PAM® Series P machine has the extruders fixed to the structure, while the build platform is mounted on a delta positioning system. Geoffroy et al. [97] used the PAM® machine to print from pellets of neat and flame-retarded polymers. Polymer compounding and pelletizing were previously carried by Co-TSE. The dispersion degree of the additives was characterized by x-ray mapping, and the flame-retardancy performance achieved with the 3D printing process was compared to the results obtained from thermocompression. The screw-assisted deposition process influenced the resulting size of the additive particles, which affected the fire behavior.

The M3DIMAKER® presents a print head integrated to a Cartesian positioning system, and moves in three directions. Its build platform is fixed. Goyanes et al. [19] used the M3DIMAKER® machine to produce printlets (3D printed tablets) from drug-loaded polymer powders. The extrusion temperature and other process parameters were kept fixed, to evaluate the performance of the printlets produced with different grades of the polymer matrix. The printlets were fabricated in a single-step process from small amounts of material. According to the authors, the machine can prevent thermal degradation of the drugs, expedite pre-clinical tests, and enable the production of dose-personalised medicines using a much broader range of excipients.

The Exam255® uses a Cartesian positioning system with the print heads moving in the XY plane, while the build platform moves in the z-axis. The machine frame is encapsulated. Lengauer et al. [15] used the ExAM 255® to directly 3D print hardmetal combined with polymeric binders used in the IM industry. After 3D printing, the green parts were subject to thermal debinding and sintering. The printing quality achieved with the screw-assisted system was compared to the results from a low-cost desktop FFF 3D printer, using self-fabricated hardmetal filaments. As discussed by the authors, the smaller nozzle diameter generated higher extrusion pressure that was beneficial to the quality of the printed parts.

### 3.2.2 Large-scale systems

Most experimental screw-assisted print heads that were specifically developed (or could be applied) for large-scale 3D printing share the same general design described in the previous topic. Some systems appropriated from commercially available extruders [98, 99, 102], while others presented custom-made extrusion units with conveying screws [100]. Typical extrusion screws with a compression profile have also been used [101,104]. The use of robotic arms in

experimental systems [100-102, 104] was more frequent than the Cartesian positioning systems [98, 101].

Hertle et al. [98] adapted a screw-driven welding extruder to a gantry structure, with the build platform moving in two directions. The equipment could be fed with polymer pellets and was initially used to assess material adhesion in shear test specimens. In a later publication, a similar welding extruder was mounted on a six axes robot arm. Material deposition was performed onto electrochemically treated aluminum sheets to assess once again the shear strength of test specimens [99].

Magnoni et al. [102] attached a benchtop-sized screw extruder to a robotic arm that could move on six axes to perform large-scale 3D printing directly from polymer pellets. The focus of their work was determining the influence of the process parameters on the resulting height and width of the deposited material. An online control routine was implemented to correct the positions of the robotic arm based on the data acquired during material deposition. In a subsequent work, an online re-slicing algorithm was developed to compensate the variations in height during 3D printing, so that the original part size could be preserved [103].

Brooks et al. [100] have also described a screw-assisted extrusion unit that could be used for large-scale 3D printing, but it was explored in the manufacture of thin-shelled parts without the need for supports. Instead of a moveable print head, a convex deposition platform was attached to a robotic arm. The convex surface could be moved with six degrees-of-freedom. Pellets of fibre-reinforced polymer were processed. The focus of their paper was on the algorithm developed to generate the printing trajectory of 2D geometries projected to the build platform.

The machine described by Schmidt et al. [104] had a fixed print head, with the build platform attached to a robotic arm that could move on six axes. The custom-made print head included a screw with compression profile. Calibration experiments were performed in function of the material type, processing and 3D printing conditions. Test specimens were cut from single-walled cylinders built under a continuous extrusion mode.

Figure 39 presents the alternative solution proposed by Liu et al. [101] for a screw-assisted print head with application in large-scale 3D printing. In a first processing stage, a screw with compression profile was responsible for conveying and melting the polymer pellets. A conveying screw was used to control the extrusion rate in the second stage. Both screws could

be driven independently, and the vertical screw could rotate backwards to retract the material during the 3D printing process. The extruder was integrated to a milling machine and could be moved on the y-z plane, while the build platform moved on the x-axis. Tests were performed with composite pellets to understand the influence of the pressure generated in the first stage and the rotation speed of the conveying screw on the resulting flow rate. Tensile specimens were cut from 3D printed plates. The capacity to print more complex parts was also demonstrated, however, melt flow instabilities were reported [101].

*Figure 39. Schematic illustration of the alternative design for large-scale screw-assisted 3D printing developed by Liu et al. [101].*

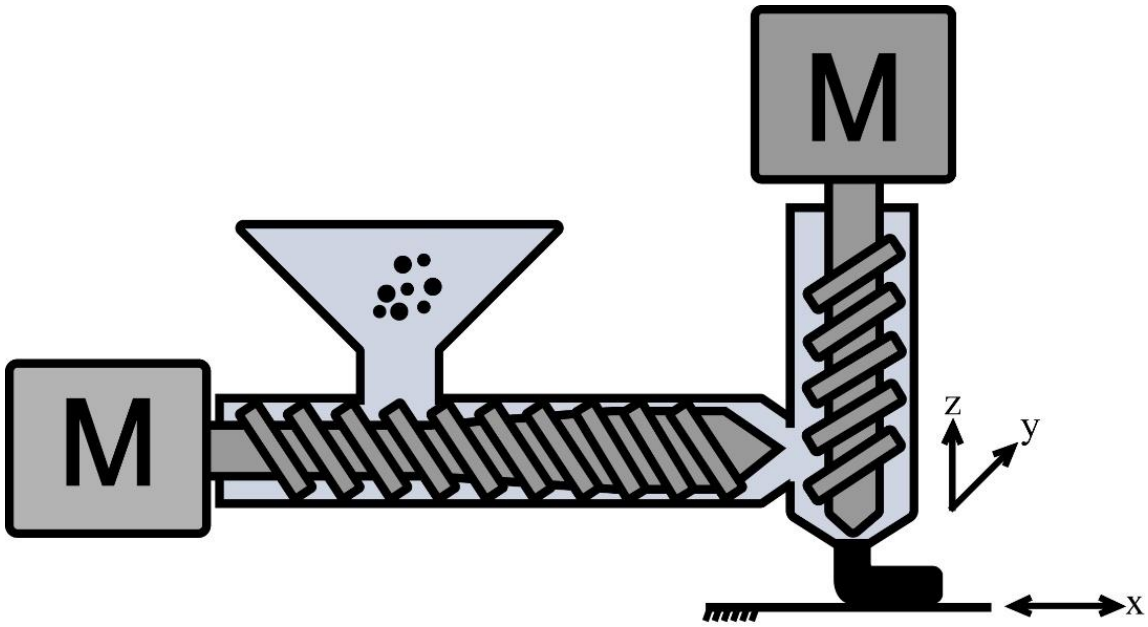


*Source: the author*

Three commercially available SA-MEX systems for large-scale applications were found by the systematic search, as shown in Fig. 40. The BAAM® (Big Area Additive Manufacturing) 3D printer, marketed by Cincinnati Inc. (Harrison, USA), the Gigabot X® 3D printer, marketed by re:3D (Houston, USA), and the Super Discovery 3D Printer®, market by CNC Barcenas (Valdepeñas, Spain). All three systems are composed by benchtop-sized screw extruders mounted on gantry structures. The print head from the BAAM® system moves on the x-axis, and the build platform moves on the y-z plane. The print heads from the Super Discovery 3D Printer® and Gigabot X® move on the x-y plane, and the build platform on the z-axis.

*Figure 40. The large-scale screw-assisted systems found in the systematic search: a) the BAAM® machine, b) the Gigabot X® machine, and c) the Super Discovery® 3D printer.*

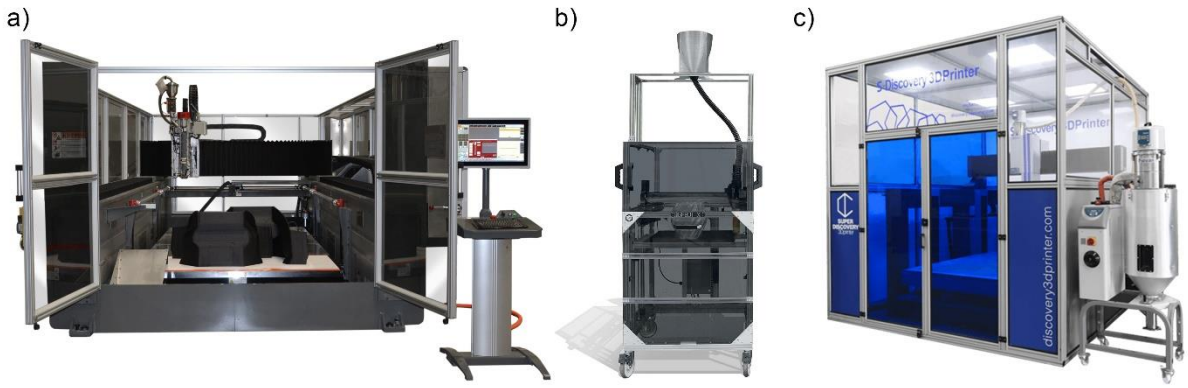


*Source: (a) [122], (b) adapted from [113] , (c) [123]*

Duty et al. [105] reported the development of the BAAM® technology. The extrusion unit originally appropriated from the screw of a welding extruder, which was later replaced by a longer screw version to avoid intra-bead porosity and increase the material output. Besides, a reciprocating z-tamping attachment was added to the print head to further reduce porosity and improve interlayer adhesion. Process feasibility was first demonstrated using pellets of neat polymers but due to the expressive distortion and warping fibre-reinforced materials became preferred. The BAAM® machine was explored in several publications, using diverse materials, including composites based on high-temperature thermoplastics [107, 108-110]. Due to the significant difference between large- and small-scale MEX, the BAAM® process was investigated with the aid of thermomechanical modelling [106]. Based on the BAAM® process, specific design guidelines for large-scale 3D printing were developed by Roschli et al. [56].

Woern et al. [111] first tested the Gigabot X® 3D printer with a variety of particulate materials, including pellets of virgin polymers and recycled polymers. An experimental matrix was proposed to determine the optimum printing parameters for each material in function of the temperature and deposition speed. The adequate deposition speed was mostly dependent on the shape of the feedstock (*e.g.* pellets, shreds, or flakes). Tensile specimens were fabricated and the properties achieved with the recycled materials were found to be comparable to the virgin polymers. Later publications described recycling tests with other materials [9,112,113], obtained from shredded plastic parts. Besides the calibration experiments and the fabrication of test specimens, complex parts were 3D printed to demonstrate the technical and economic feasibility [9,113]. The 3D printing tests with composite particles made of hard and flexible polymers performed by Dertinger et al. [112] were unsuccessful due to feeding difficulties.

Later, Little et al. [73] added a feeder to avoid melt flow inconsistencies due to the irregular shape and size of the shredded feedstock.

The Super Discovery 3D Printer® was tested by Moreno Nieto [114], to demonstrate its applicability on the naval industry. The print head was equipped with an articulated arm, where different tools, such as a video surveillance device, could be fitted. That way, the process could be remotely supervised. Pellets of different polymers were processed, in some cases with manual addition of reinforcing fibres. Expressive thermal distortion was observed with some of the neat polymers, while poor printability with the fibre-reinforced composites was reported.

## 3.3 Conclusions

The research conducted with the SA-MEX systems described in the previous sections is very diverse. Some publications are more dedicated to the design of the extrusion units and its influence on the MEX process [9,65,67,70,85,86,89,90,100,101,105], others try to enable and characterize 3D printing with certain materials [19,15,63,64,66,68,69,76-85,87,91-93,97,98,99,102-104,106-114], and others seek to achieve specific properties or performance with the 3D printed parts [11,12,66,68,71-75,93-96].

From the publications with focus on the design of the print heads, most contributions were made to solve thermal-related issues which usually lead to premature melting and material agglomeration at the feeding zone [9,86,88,89,100]. Some works addressed screw design [65,67,85,90,104,105] or other modifications to the extrusion principle [70,101] to improve the melting efficiency and/or achieve better control over the flow rate.

Besides allowing small- and large-scale 3D printing with otherwise hard-to-print or unavailable materials, including neat polymers (*e.g.* biopolymers [10,63], elastomers [50, 77,78,80,82,91,97], and composites [16,66,68,81,83,84,93,97,106-110,114]), the potential of SA-MEX was explored for indirect 3D printing of ceramics [16,15, 64,69], and metals [69], as well as a key enabling technology for distributed recycling [9,92,111-113], and personalised medicine [19].

When the main objective was not the development of the screw-assisted print head itself or exploring SA-MEX with different materials, the overall research purpose was to produce adequate structures for cellular growth [11,12,66,68,71-75,94-96]. Pointed in Section 3.2.1 as one of the most prominent application fields for SA-MEX, bio-AM benefits from the capacity to taylor the material composition and microstructure of the individual deposited roads (*i.e.*

material properties), as well as the ability to control the spatial arrangement of the individual roads that compose the printed scaffolds (*i.e.* mesostructure).

The review has also shown that the SA-MEX systems do share some common aspects. First, single screw extrusion (SSE) has been the basis for the development of all systems described in the publications. Second, given the size and weight constraints associated with MEX, the extruders are always miniaturized (even those used for large-scale applications). Third, a vertical arrangement was usually preferred. A typical extrusion screw (with compression profile), however, was not used in all systems.

From the methodological perspective, a general workflow for the development of SA-MEX equipment can be proposed. Shown in Figure 41, the workflow is composed by five stages: project planning, design of the print head, design of the positioning system, deposition control strategy, and performance assessment.

*Figure 41. General development workflow for SA-MEX equipment.*

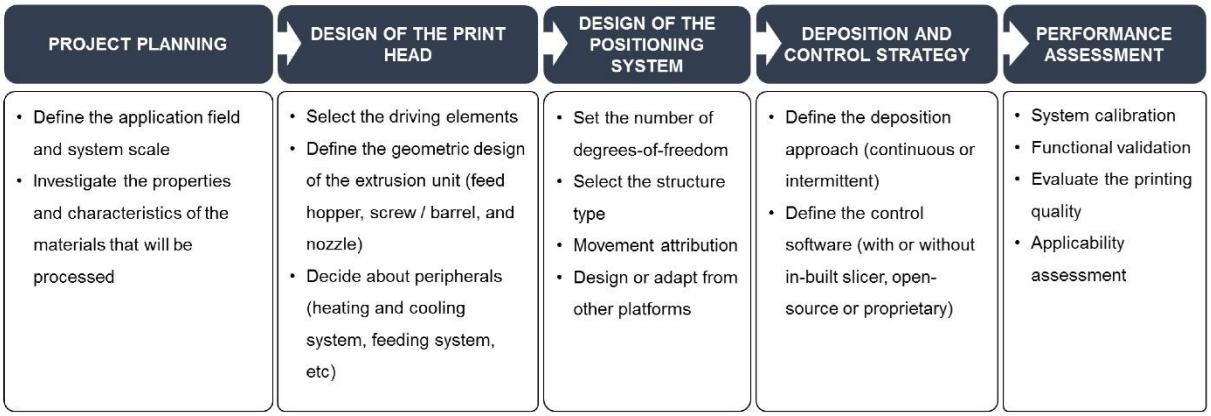


*Source: the author*

Many publications describing experimental systems showed that the development workflow starts by the definition of the application field and system scale [64,67,71,76,85,90,91,93,101]. Also, it is important to investigate the properties and characteristics of the feedstock materials (*e.g.* viscosity [79,81,88,99,107], thermal behavior [19,88,108,112], or particle size distribution [9,92,111-113].

Next, for the design of the print head, the authors had to choose which driving elements would be used, define the geometry of the main components of the extrusion unit [65,67,90,101,104], and decide about any peripherals such as feeders [65,86,112], additional cooling elements [9,87,100], heaters [85], or other mechanisms to improve the state of the deposited layer [85, 98,99,105].

During the design of the positioning system, the number of degrees-of-freedom and type of structure must be defined. Some authors used robotic arms [98-100,102,104] with multiple degrees of freedom or CNC systems [50,101], depending on the intended application. When the design of the print head limits its movements, the positioning system should enable 3D printing with a moveable build platform [65,69,85,97,100,104]. The overall frame of the 3D printers can be adapted from pre-existing systems [68,70,76] or custom-made to meet specific requirements [64,69,71,84,100,106].

SA-MEX can be performed by continuous [10,50,68,75,84,100] or intermittent deposition [70,101,114]. The problem of unwanted extrusion, referred to as “over deposition” [62], “bleeding” [76], “leakage” [10], or “salivation” [101] was reported and could be circumvented with a continuous deposition approach, control of the volumetric flow [69,70], or material retraction [100,101,114]. A software is necessary to control the screw rotation speed, temperature, and machine movements. Proprietary [15,90,113,114] or open-source options that can include or not slicing tools can be used [86,91,92,103,112].

Finally, when the machine is ready, experiments for performance assessment must be performed. This involves initial tests for the system’s calibration, usually to correlate the screw rotation speed with the material output at different temperatures [77,81,8591,101,104]. Knowing the volumetric output is critical to estimate speed range of the build platform. Functional validation involves actual 3D printing and is often followed by a quality assessment. This often involves mechanical testing [10,16,50,65,68,71,76,83,85,86-91,93, 98,101,104,105], microscopic [16,19,63,64,66,68,69,74,85,86,88,89,93,94,96,105], and surface analysis [65,85,89]. Depending on the intended application, applicability assessment through biological tests [10-12,63,66,96], and physic-chemical characterization [11,19,68,73,88, 94,96,97] might be needed. Comparison with the performance achieved by other machines and/or technologies (*i.e.* benchmarking) may also be valuable [9,15,92,112].

# 4 DEVELOPMENT OF THE CO-TSE AM SYSTEM

In the previous chapter, the potential of using single screw extrusion in MEX was discussed. Besides allowing to circumvent filament manufacturing and, thus, expand the range of applicable materials, SA-MEX can offer enhanced control over the plastication process, enable multimaterial printing, and lead to higher deposition rates. Despite the mentioned capabilities, the output of the miniaturized extruders is not solely dictated by the screw speed but also depends on nozzle geometry and polymer rheology. Moreover, their mixing ability is limited [22].

The possibility of developing a twin screw extrusion unit for 3D printing was first mentioned by Inforçatti Neto in 2013. Although it was not developed at the time, the idea of using one or two screws was pointed as potential solutions to address specific users` requirements related to the mixing capacity of a custom-made MEX bioprinter [124].

As described in the Section 2.2, the co-rotating twin screw extruders have been widely used for compounding operations, offering great process flexibility due to its modular assembly, with the capacity to operate in higher speeds and yield higher throughputs. The initial concept for an innovative 3D printer based on twin screw extrusion was proposed by Justino Netto [125], integrating Co-TSE and MEX in a benchtop research platform. The objective of the original concept is to offer high operational flexibility and improved mixing capacity to further address the same research demands indentified by Inforçatti Neto [124]: allow small processing studies and 3D printing, using powdered or granulated polymers, in a single equipment.

The system-level design of the Co-TSE 3D printer is presented and discussed in this chapter. The following sections present the successive iterations carried out to detail the equipment and specify its key components. As required in the development of complex systems, the major subsystems were prototyped and tested at the end of each iteration. After three iterations, the design was completed and all components were considered apt for the final integration and experimental validation.

## 4.1 First design iteration

Similar to any other MEX 3D printer, the Co-TSE AM system can be thought of as a machine composed by a material dispensing unit and a positioning system. At the beginning of

the project, it was presumed that the design of the material dispenser (*i.e.* the co-rotating twin screw extrusion unit) would be more demanding and, therefore, should be prioritized.

The initial layout of the print head was defined in the first design iteration. The functional diagram outlined for the first version of the print head is shown in Fig. 42, in which the arrows indicate the flows of energy (E), material (M), and information (i) through the function boxes. The main design constraints are also represented.

*Figure 42. Functional diagram of the Co-TSE printhead during the first design iteration along with the main design constraints.*

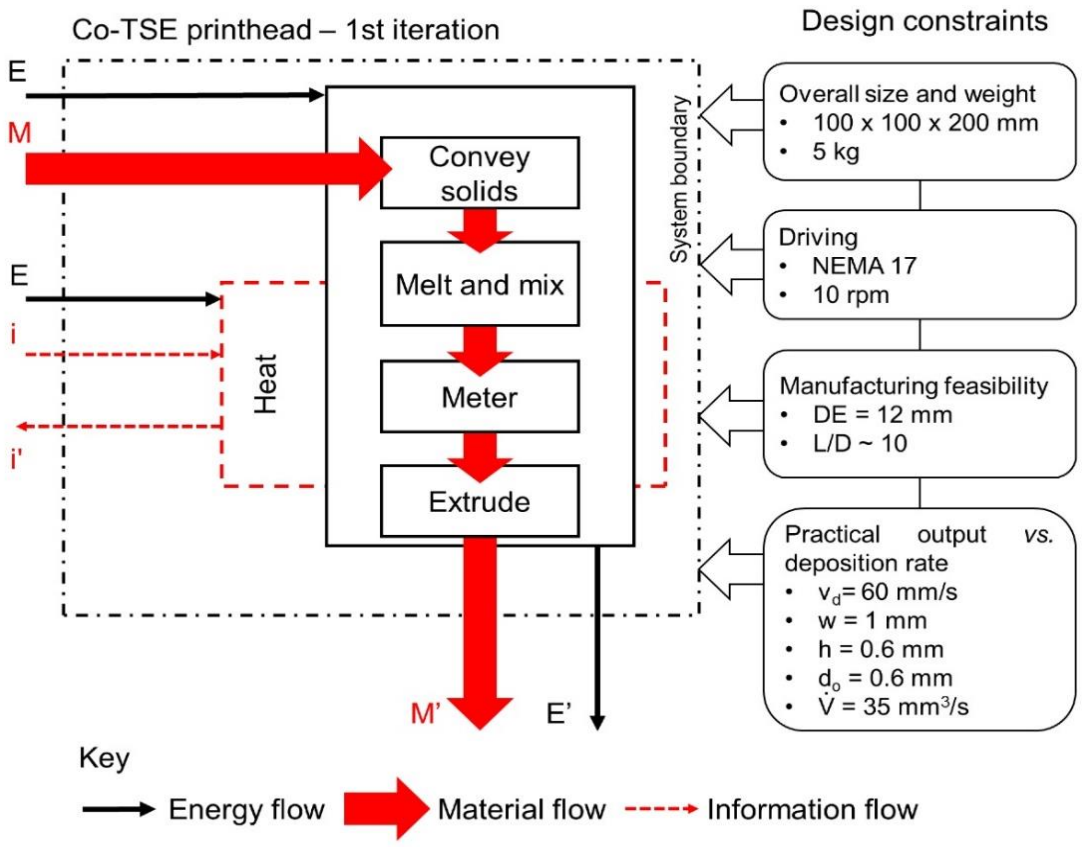


*Source: the author*

Energy is supplied to drive the screws and subject the material to the required processing tasks. Material enters the system as solid granules, is conveyed, melted, mixed, metered and extruded out the system in the molten state. Another energy flow is required to heat the barrel and aid in the melting process. The latter should be accompanied by a flow of information to control the process temperature. Part of the supplied energy leaves the system as heat and noise.

The limits imposed by the constraints helped to define the system. In the first iteration, the print head was assumed to move in the XY plan. Therefore, the overall size and weight were not supposed to exceed 100 x 100 x 200 mm and 5 kg, respectively. Due to its easy control and

low cost, it was decided to use a stepper motor to drive the screws. A Nema 17 motor was initially assumed capable to provide the required processing torque at 10 rpm. The external diameter (DE) of the screws should be 12 mm, and the L/D ratio close to 10 to facilitate manufacturing. The volumetric flow rate ($\dot{V}$) through the extruder was stipulated considering 3D printing with a 0.8 mm nozzle. For a deposition speed around 60 mm/s, road width (w) and layer height (h) equal to 1 and 0.6 mm, respectively, the resulting output would be approximately 35 $mm^3/s$.

The free cross-sectional area ($A_{free}$) of the twin screw was estimated using the Eq. 32, assuming the volumetric throughput ($\dot{V}$) of a half-filled conveying element with pitch (T) and rotating with speed (N) [37].

$$A_{free} = \frac{4\dot{V}}{NT} \tag{32}$$

For the stipulated output of 35 $mm^3/s$ at 10 rpm, and considering a square-pitched element (T = DE) with external diameter (DE) equal to 12 mm, the resulting $A_{free}$ is 70 $mm^2$. With the ratio between the free cross-sectional area to the squared screw diameter ($A_{free}/DE^2$), it was possible to use the graph from Section 2.2.1 and determine the ratio between the centerline distance and screw diameter (A/DE). Therefore, for a double-flighted screw with $A_{free}/DE^2 = 0.48$, A/DE is approximately 0.85. Thus, the centerline distance is equal to 10.2 mm.

The calculated A/DE complies with the condition expressed by Ineq. 11 (A/DE > 0.707) and, therefore, Eq. 12-14 could be used to calculate the remaining dimensions of the screws. Figure 43 shows the resulting self-wiping profile, indicating the external and internal diameters (DE = 12 mm, DI = 8.4 mm) and the distance between the screws (A = 10.2 mm).

*Figure 43. Self-wiping profile obtained for double-flighted twin screws with A/DE = 0.85 and A = 10.2 mm.*

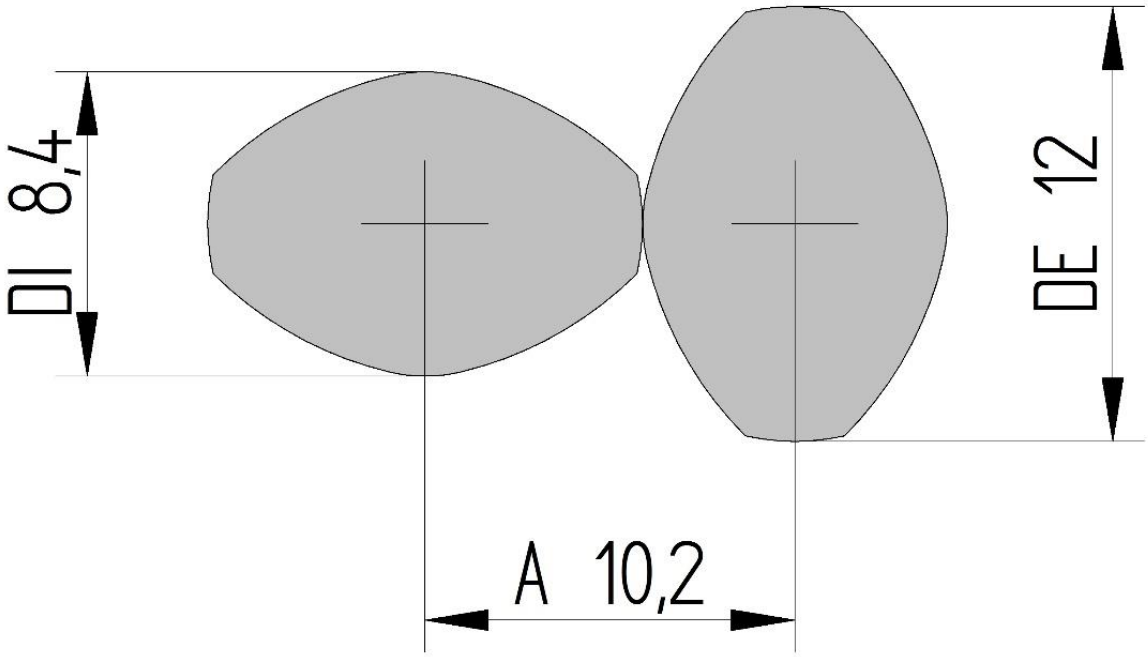


*Source: the author*

The dimensions of the actual screw profile, reduced by both the screw/screw (s) and screw/barrel (δ) clearances, were calculated according to the planar offset method. The MatLab® script used for this is transcribed in the Appendix A. The calculations were performed for conveying elements with pitch (T) of 18, 12, and 6 mm, based on the typical proportion to the diameter used for the feeding, solids conveying, and metering zones (1.5 DE, 1DE, 0.5 DE, respectively). All clearances were considered equal to 0.2 mm. The resulting dimensions of the offset screw profile, *i.e.* the actual external and internal diameters (DA and DK, respectively), as well as the actual tip width, tip angle and flank angle (KB1, KW1, and FW1, respectively) are summarized in Table 4.

*Table 4. Geometric input parameters and output data from the planar offset calculation procedure.*

| Input | | | | | | Output | | | | |
|---|---|---|---|---|---|---|---|---|---|---|
| DE (mm) | A (mm) | Z | T (mm) | s (mm) | δ (mm) | DA (mm) | DK (mm) | KB1 (mm) | KW1 (rad) | FW1 (rad) |
| | | | 18.0 | | | | | 1.22 | 0.42 | 1.15 |
| 12.0 | 10.2 | 2 | 12.0 | 0.2 | 0.2 | 11.8 | 8.2 | 0.76 | 0.40 | 1.17 |
| | | | 6.0 | | | | | 0.29 | 0.30 | 1.27 |

*Source: the author*

The stipulated length for the feeding, solids conveying, and metering zones were 18, 24, and 18 mm, respectively. The initial screw configuration also presented two kneading blocks

positioned between the solids conveying and metering zones. Eight 3.5 mm thick discs staggered by 45º in relation to one another formed the upstream kneading block (KB). The downstream KB was formed by twelve 2 mm thick discs staggered by -45º in relation to one another. The length of the screw summed 112 mm, therefore L/D = 10. The initial screw configuration is schematized in Fig. 44.

*Figure 44. Representation of the first screw configuration proposed to the Co-TSE print head.*

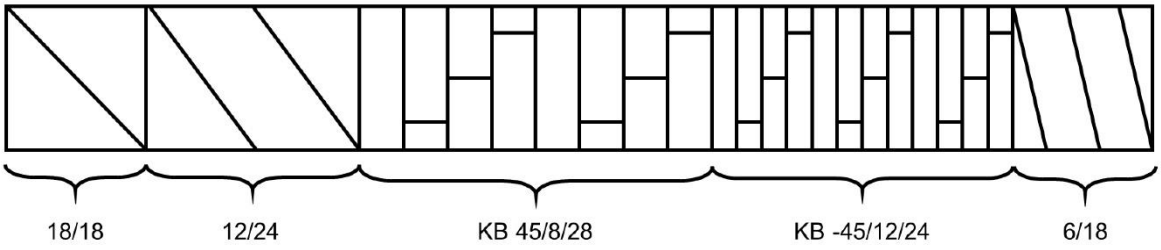


*Source: the author*

The embodiment design of the first version of the Co-TSE unit is presented in Fig. 45. Besides the twin screw, construction details for the feed hopper, barrel, and die are shown. The screw segments slide in hexagonal shafts and are fixed by end cap nuts. A single-part barrel with flanged extremities was proposed. The hopper and die are fixed to the barrel flanges; the first consisting simply of a tapered reservoir, and the latter formed by a convergent channel with interchangeable nozzle. For simplicity, the extruder was assumed to work under flood feeding regime.

*Figure 45. Embodiment design of the Co-TSE unit.*

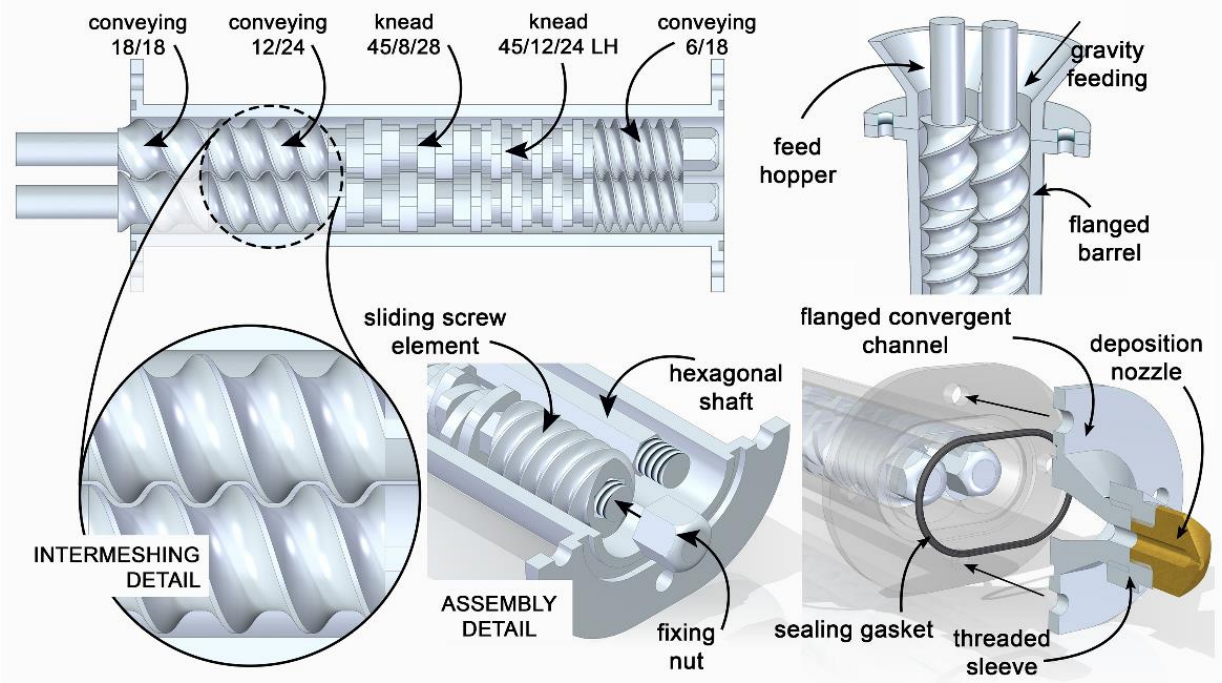


*Source: the author*

The preliminary design of Co-TSE AM system is shown in Fig. 46, with the first version of the print head featured in the detail. A Cartesian positioning system supported by a cubic frame was proposed. The print head moves on the XY plan, while the build platform moves in the vertical direction. A gearbox formed by four helical gears is also shown. The stepper motor and speed reducer are indicated as the black and green boxes on the figure, but were not detailed.

*Figure 46. Preliminary design of the complete Co-TSE AM system.*

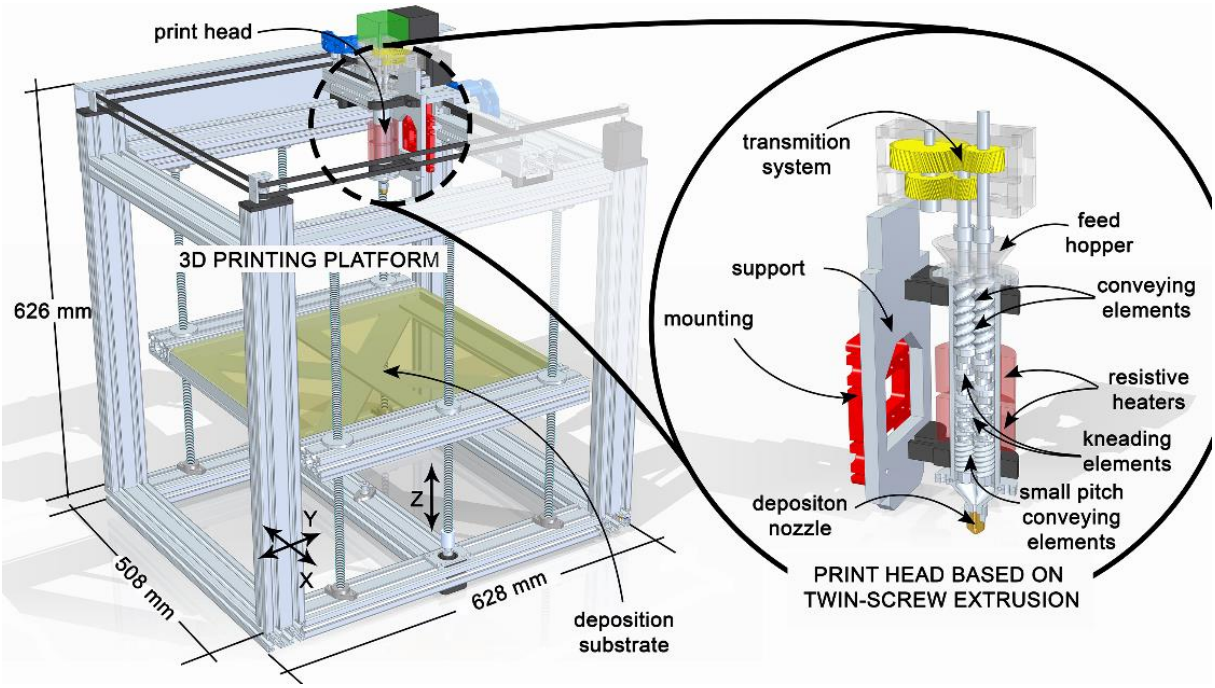


*Source: the author*

Figure 47 shows the prototypes made during the first design iteration. A complete mock-up of the print head was built using a desktop FFF 3D printer (GTMax3D, Brazil), to give the real notion on the size of its components and check the regularity of the clearance between the co-rotating screws. The parts were 3D printed in acrylonitrile-butadiene-styrene (ABS). Some screw elements were also made by selective laser melting (SLM) in an MLab 200R machine (Concept Laser GmbH, Germany), using cobalt-chromium-tungsten alloy, to assess the feasibility of the process. The measured hardness of the metal 3D prints was about 38 HRC (Rockwell C).

*Figure 47. Prototypes made by the end of the first design iteration: (a) sectioned view of the extrusion unit with hand crank, (b) main components of the extrusion unit, (c) first metal 3D printed screw elements.*

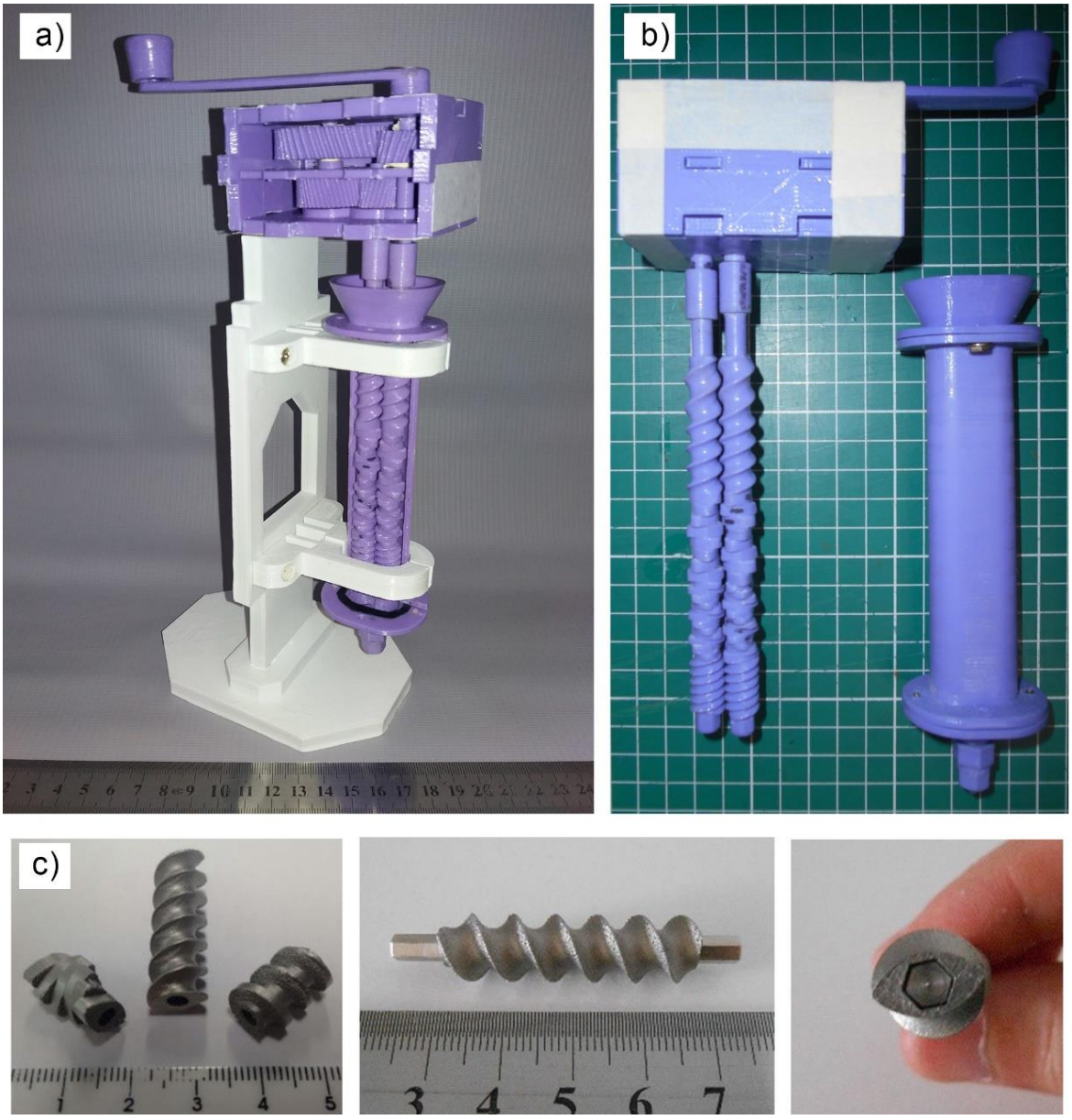


*Source: the author*

## 4.2 Second design iteration

During the second iteration, significant modifications were made considering the mixing performance. These include the use of a volumetric feeder and increasing the speed of the screws. The geometry of screw elements was also modified with regard to manufacturing aspects. As the system became sufficiently detailed, analytical calculations were performed to estimate the average shear rate, processing torque, mean residence time, and pressure drop at the die section. The driving components were detailed. The updated functional diagram of the print head and the main design considerations mentioned are shown in Fig. 48.

*Figure 48. Functional diagram of the Co-TSE print head during the second design iteration along with the main design considerations.*

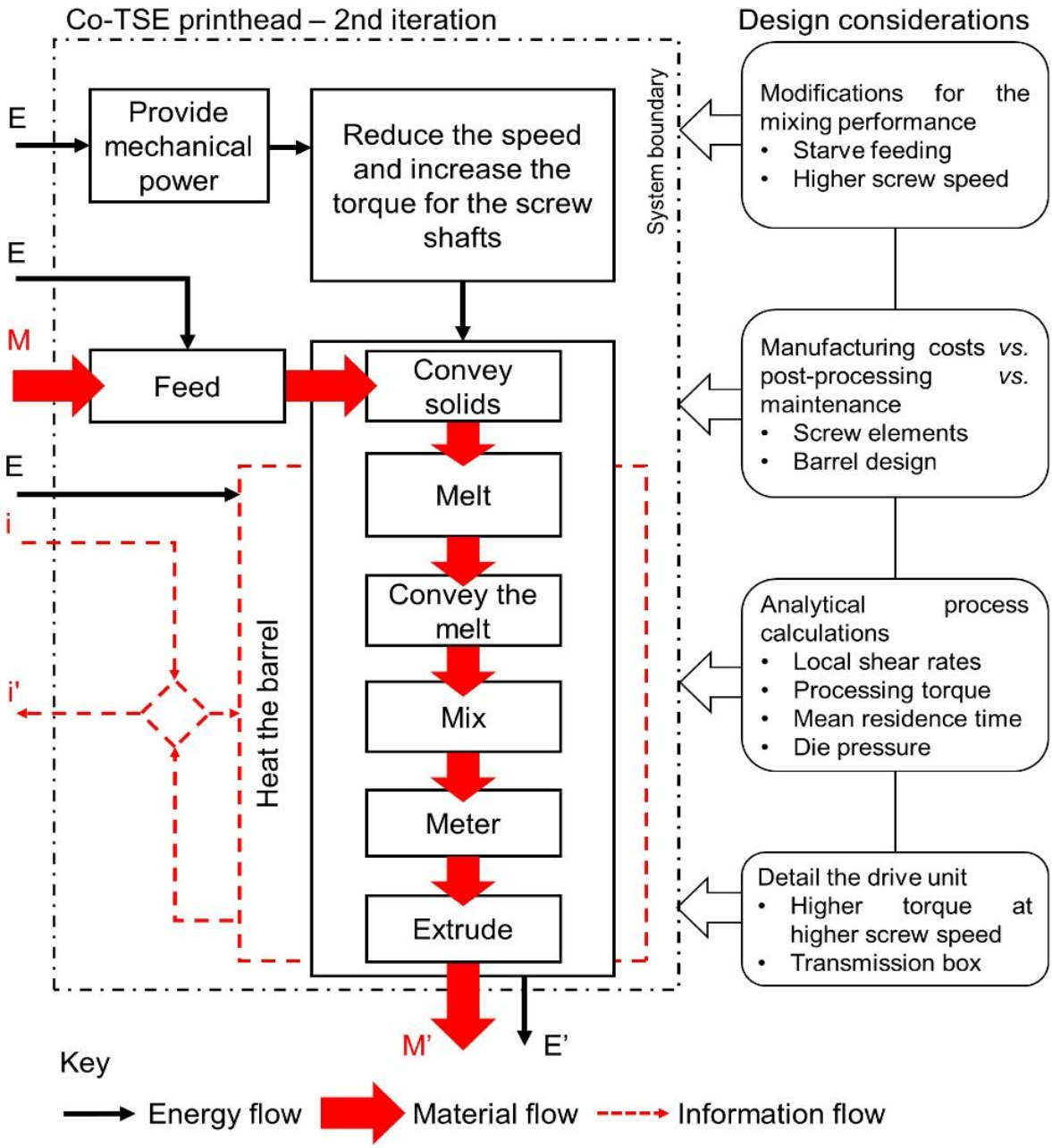


*Source: the author*

The first important modification was the inclusion of a volumetric feeder to operate the print head under the starve feeding regime. Despite being simpler to implement, flood feeding tends to generate high pressures in the solids conveying and melting zones, which agglomerate the components that should be dispersed and distributed [22]. Moreover, the torque consumed by the extruder under the flood feeding regime is higher.

Figure 49 illustrates the basic components of the volumetric feeder. The granular material is stored in a conical hopper, and flows into the feeder barrel by gravity. A single-flighted, square-pitched Archimedean screw conveys the granules from the feed throat to the discharge.

*Figure 49. Basic components of the volumetric feeder.*

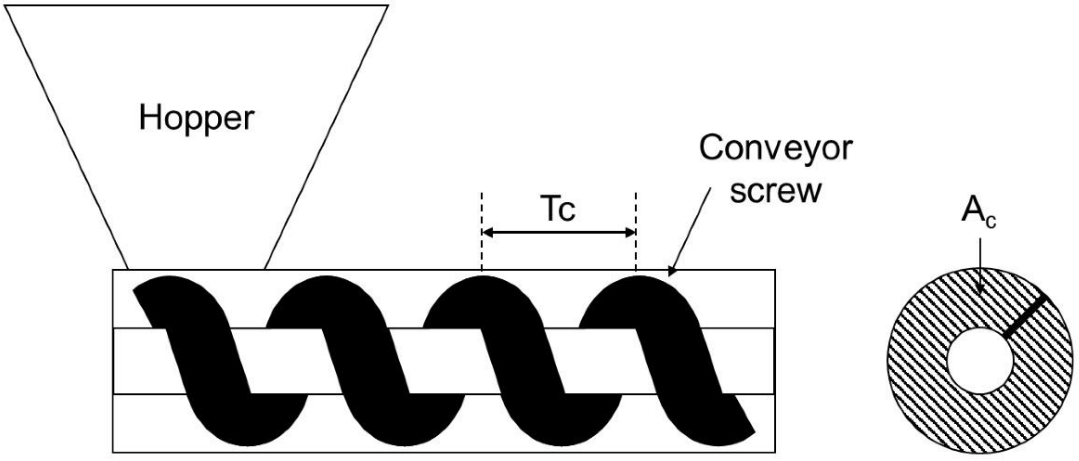


*Source: the author*

The operating speed of the feeder was estimated using Eq. 33, in function of the volumetric feed rate ($\dot{V}$), pitch ($T_c$), cross-section area of the conveyor screw ($A_c$), as well as correction factors for the loading efficiency of the section ($\psi$) and for the angle of the feeder (C) [126].

$$N_f = \dot{V}/T_c A_c \psi C \quad (33)$$

The cross-section area of the feeder screw with one helicoidal flight was approximated to the area of a 15 mm diameter circle. The loading efficiency factor was assumed 0.4 (for free-flowing and nonabrasive materials), and the correction factor (C) was assumed 1 (for horizontal feeders). The feeder operating speed ($N_f$) for starve feeding with 17.5 $mm^3/s$ to 35 $mm^3/s$ of material was estimated to range from 1 to 2 rpm.

To guarantee better mixing performance for the print head, the intended speed range for the twin screw was increased. The screw speed is paramount to the shear rates developed. Moreover, the higher speeds would also help to reduce the filling ratio of the screw channels, which is positive to further reduce the overall torque requirements. Since the extruder will be partially filled, increasing the screw rotation speed will not affect the final output. The rotation speed of twin screw was updated to range from 50 rpm and 100 rpm.

With respect to the fabrication of the prototype, the SLM process tested in the first iteration was considered more suitable for the project budget compared to any other machining process. However, the resulting parts could not be used as printed: the roughness of some surfaces, mainly those facing downwards during 3D printing, was considered inapropriate for the extrusion process. It could be noticed that the surface quality also became worse as the pitch of the screw elements was reduced, which is probably related to the steeper (almost horizontal) overhanging surfaces. To facilitate polishing the 3D printed screw segments, the pitch and length of the conveying elements were updated to 20/40, 15/40, and 10/20, and the single-piece design used for the kneading blocks was updated by a modular design formed by individual 3 mm thick kneading discs. The discs were designed so that thet could be staggered at 60º or -60º with relation to one another.

Since the variation of the actual tip and flank angles (KW1 and FW1, respectively) with the different pitch values was very small, the planar offset method was implemented only for the 15/40 element. The clearance values were kept the same as in the first iteration (*i.e.* 0.2 mm). The resulting profile, with KW1 = 0.41 rad and FW1 = 1.16 rad, was used for the other screw segments. After modifying the individual screw elements, the total screw length was increased to 130 mm (L/D ~ 11). Apart from the first and final conveying elements corresponding to the feeding and metering zones, respectively, the updated screw configuration was formed by two kneading blocks separated by another conveying element (see Fig. 50). The first resctrictive zone upstream was intended to promote melting, and the second dispersive mixing.

*Figure 50. Updated screw configuration.*

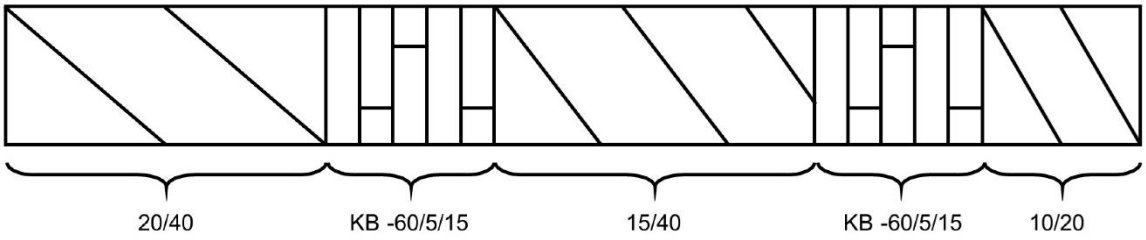


*Source: the author*

The average shear rate developed in the conveying elements of a co-rotating twin screw extruder was estimated by the approximate method presented by Vergnes [127]. The method is based on the flat plate screw geometry, neglects the intermeshing area, and considers a Newtonian isothermal flow. The global average shear rate ($\bar{\dot{\gamma}}$) is given by Eq. 34, as the sum of the flow components developed downchannel ($\bar{\dot{\gamma}}_{yz}$) and cross-channel ($\bar{\dot{\gamma}}_{xy}$).

$$\bar{\dot{\gamma}} = \sqrt{\bar{\dot{\gamma}}_{xy}^{\ 2} + \bar{\dot{\gamma}}_{yz}^{\ 2}} \tag{34}$$

The cross-channel flow rate is zero (no leakage flows hypothesis) and, therefore, the average shear rate in this direction ($\bar{\dot{\gamma}}_{xy}$) can be simplified as in Eq. 35, in function of the tangential velocity at tip of the screw (v), the flight angle (φ) and the channel height ($h_c$) [127].

$$\bar{\dot{\gamma}}_{xy} = \frac{5}{3}\frac{v \sin\varphi}{h_c} \tag{35}$$

The tangential velocity (v) and the flight angle (φ) are calculated by Eq. 36 and Eq. 37 [127].

$$v = \pi N D E \tag{36}$$

$$\tan\varphi = {}^{T}/_{\pi D E} \tag{37}$$

In the longitudinal direction, *i.e.* downchannel, the total shear rate presents a pressure term and a drag term. When a right-handed conveying element is fully filled, the average shear rate in the longitudinal direction ($\bar{\dot{\gamma}}_{yz}$) can be expressed by Equation 38. The pressure term depends on the partial volumetric flow rate of the screw channels ($\dot{V}_{ch}$), channel width (B), and channel height ($h_c$). For half filled positive conveying elements, the average shear rate is calculated as in Eq. 39 [127].

$$\bar{\dot{\gamma}}_{yz(fully\ filled)} = \begin{cases} \frac{5}{2}\frac{v\cos\varphi}{h_c} - \frac{3\dot{V}_{ch}}{Bh_c^2}, & if\ \dot{V}_{ch} < v\cos\varphi\ \frac{Bh_c}{2} \\ -\frac{1}{2}\frac{v\cos\varphi}{h_c} + \frac{3\dot{V}_{ch}}{Bh_c^2}, & if\ \dot{V}_{ch} > v\cos\varphi\ \frac{Bh_c}{2} \end{cases} \tag{38}$$

$$\bar{\dot{\gamma}}_{yz\,(half\ filled)} = \frac{v\cos\varphi}{h_c} \tag{39}$$

The semi-circular screw channel can be simplified to a rectangle, with width (B) calculated by Eq. 40 (Potente et al., 1994), and height ($h_c$) equal to half the maximum semi-circular channel height [25]. The partial volumetric flow rate is obtained by Eq. 41 [127].

$$B = \frac{T\cos\varphi}{Z} - \frac{T\left(\frac{\pi}{Z} - \Omega\right)\cos\varphi}{2\pi} \tag{40}$$

$$\dot{V}_{ch} = \frac{\dot{V}}{2Z - 1} \tag{41}$$

The average shear rate was estimated for the extruder operating at 50 rpm and 100 rpm, with feed rate (throughput) of 17.5 $mm^3/s$ and 35 $mm^3/s$. The estimates were made for the 20/40,

15/40, and 10/20 conveying elements. Since the former two segments (*i.e.* 20/40, and 15/40) are positioned upstream to kneading blocks, they are expected to operate fully filled to some extent. The 10/20 elements are expected to operate only partially filled. The results are presented in Table 5.

*Table 5. Estimated shear rate for the conveying elements operating under different conditions.*

| Conveying element | Throughput ($mm^3/s$) | Screw speed (rpm) | Average shear rate ($s^{-1}$) |
|---|---|---|---|
| 20/40 | 17.5 | 50 | 79.1 |
| | | 100 | 160.8 |
| | 35 | 50 | 76.4 |
| | | 100 | 158.1 |
| 15/40 | 17.5 | 50 | 80.4 |
| | | 100 | 164.2 |
| | 35 | 50 | 76.9 |
| | | 100 | 160.5 |
| 10/20 | 17.5 | 50 | 42 |
| | | 100 | 84.1 |
| | 35 | 50 | 42 |
| | | 100 | 84.1 |

*Source: the author*

The torque required to turn the screws against the molten polymer is a key factor in the motor sizing calculations. A rough estimate of the processing torque ($M_T$) can be made based on the co-axial cylinder rheometer, as expressed by Eq. 42 in terms of the screw diameter (DE), length of the element (L), viscosity (η), and shear rate ($\dot{\gamma}$) [22].

$$M_T = \frac{\pi D E^2 L \eta \dot{\gamma}}{2} \tag{42}$$

The torque per screw was estimated considering only the conveying elements, using the average shear rates calculated at 50 rpm and 100 rpm for the 17.5 $mm^3/s$ and 35 $mm^3/s$ output. Since it was not possible to know the exact length of the segments that were fully filled, the total length of the elements was used. Although this would overestimate the required torque, it could compensate the unkown contribution of the kneading blocks. The viscosity was calculated based on the power-law model for a generic polypropylene (PP) grade with consistency factor (k) equal to 18250 $Pa \cdot s^{0.33}$ and pseudoplasticity index (n) equal to 0.33. The results are presented in Table 6.

*Table 6. Estimated local torque required by the conveying elements and total torque per screw under different conditions.*

| Screw element | N (rpm) | $\dot{V}$ (mm$^3$/s) | $M_T$ (N·m) |
|---|---|---|---|
| 20/40 | 50 | 17.5 | 0.7 |
| | | 35 | |
| | 100 | 17.5 | 0.9 |
| | | 35 | |
| 15/40 | 50 | 17.5 | 0.7 |
| | | 35 | |
| | 100 | 17.5 | 0.9 |
| | | 35 | |
| 10/20 | 50 | 17.5 | 0.3 |
| | | 35 | |
| | 100 | 17.5 | |
| | | 35 | |
| Total torque per screw (N·m) | 50 | 1.7 | |
| | 100 | 2.1 | |

*Source: the author*

The mean residence time ($\bar{t}_v$) was estimated by Eq. 43, in terms of the free volume of the screw ($V_{free}$), degree of fill (f), and operational throughput ($\dot{V}$). According to Kohlgrüber [35], the value of $V_{free}$ can be approximated by the squared screw diameter ($DE^2$) multiplied by the length of the element (L) as expressed in Eq. 44.

$$\bar{t}_v = f\frac{V_{free}}{\dot{V}} \tag{43}$$

$$V_{free} = DE^2L \tag{44}$$

The degree of fill (f), Eq. 45, is the relation between the throughput and the maximum volumetric flow rate ($\dot{V}_{max}$). The latter is calculated by Eq. 46 [37].

$$f = \frac{\dot{V}}{\dot{V}_{max}} \tag{45}$$

$$\dot{V}_{max} = \frac{1}{2}NTA_{free} \tag{46}$$

The maximum volumetric flow rate ($\dot{V}_{max}$) was calculated for the 20/40, 15/40 and 10/20 conveying elements at 50 rpm and 100 rpm, with throughput ranging from 17.5 mm$^3$/s and 35 mm$^3$/s. For the kneading blocks, which are expected to operate fully filled (f = 1), only the free volume and throughput were considered. Table 7 presents the approximate free volume, maximum volumetric flow rate, degree of fill, and estimated mean residence times for each screw element.

*Table 7. Estimated local fill ratios and residence times under different operating conditions.*

| Screw element | Operating conditions N (rpm) | $\dot{V}$ (mm³/s) | $V_{free}$ (mm³) | $\dot{V}_{max}$ (mm³/s) | f | $\bar{t}_v$ (s) |
|---|---|---|---|---|---|---|
| 20/40 | 50 | 17.5 | 5760 | 559 | 0.03 | 10.3 |
| | | 35 | | | 0.06 | |
| | 100 | 17.5 | | 1118 | 0.02 | 5.2 |
| | | 35 | | | 0.03 | |
| KB -60/5/15 | Any | 17.5 | 2160 | - | 1 | 123.4 |
| | | 35 | | | | 61.7 |
| 15/40 | 50 | 17.5 | 5760 | 419.2 | 0.04 | 13.7 |
| | | 35 | | | 0.08 | |
| | 100 | 17.5 | | 838.5 | 0.02 | 6.9 |
| | | 35 | | | 0.04 | |
| KB -60/5/15 | Any | 17.5 | 2160 | - | 1 | 123.4 |
| | | 35 | | | | 61.7 |
| 10/20 | 50 | 17.5 | 2880 | 279.5 | 0.06 | 10.3 |
| | | 35 | | | 0.13 | |
| | 100 | 17.5 | | 559 | 0.03 | 5.2 |
| | | 35 | | | 0.06 | |

*Source: the author*

The cumulative residence times were obtained by summing the contribution of the individual elements. The estimated results are presented in Table 8.

*Table 8. Estimated cumulative residence times under different operating conditions.*

| Screw speed (rpm) | Throughput (mm³/s) | Cumulative residence time (s) |
|---|---|---|
| 50 | 17.5 | 281.10 |
| | 35 | 157.70 |
| 100 | 17.5 | 264.10 |
| | 35 | 140.70 |

*Source: the author*

The pressure drop at the die section (Δp) was estimated by the Ostwald-deWaele power law expressed in Eq. 47, in which K' is the die conductance, Φ is the fluidity factor (reciprocal to the consistency factor), and m is the flow exponent (reciprocal to the power-law index) [128].

$$\dot{V} = K'\Phi\Delta p^m \tag{47}$$

The fluidity (Φ) and flow exponent (m) can be calculated from the power-law parameters (k and n) using the Eq. 48 and Eq. 49, respectively [128].

$$k = \Phi^{-1/m} \quad (48)$$

$$m = {}^{1}/_{n} \quad (49)$$

The die pressure was estimated for a simplified geometry formed by conical bores and circular tubes, with longitudinal section represented in Fig. 51. The calculations were made considering four sections, from the 8-O transition to the nozzle outlet. An equivalent diameter of 16.7 mm was used for the 8-O transition inlet, based on the barrel cross-section area calculated according to the equations provided by Potente et al. [40]. The length of the 8-O transition was estipulated as 10 mm. The remaining dimensions were based on the typical geometry of a 0.8 mm 3D printing nozzle.

*Figure 51. Schematic die geometry used to estimate the die pressure drop.*

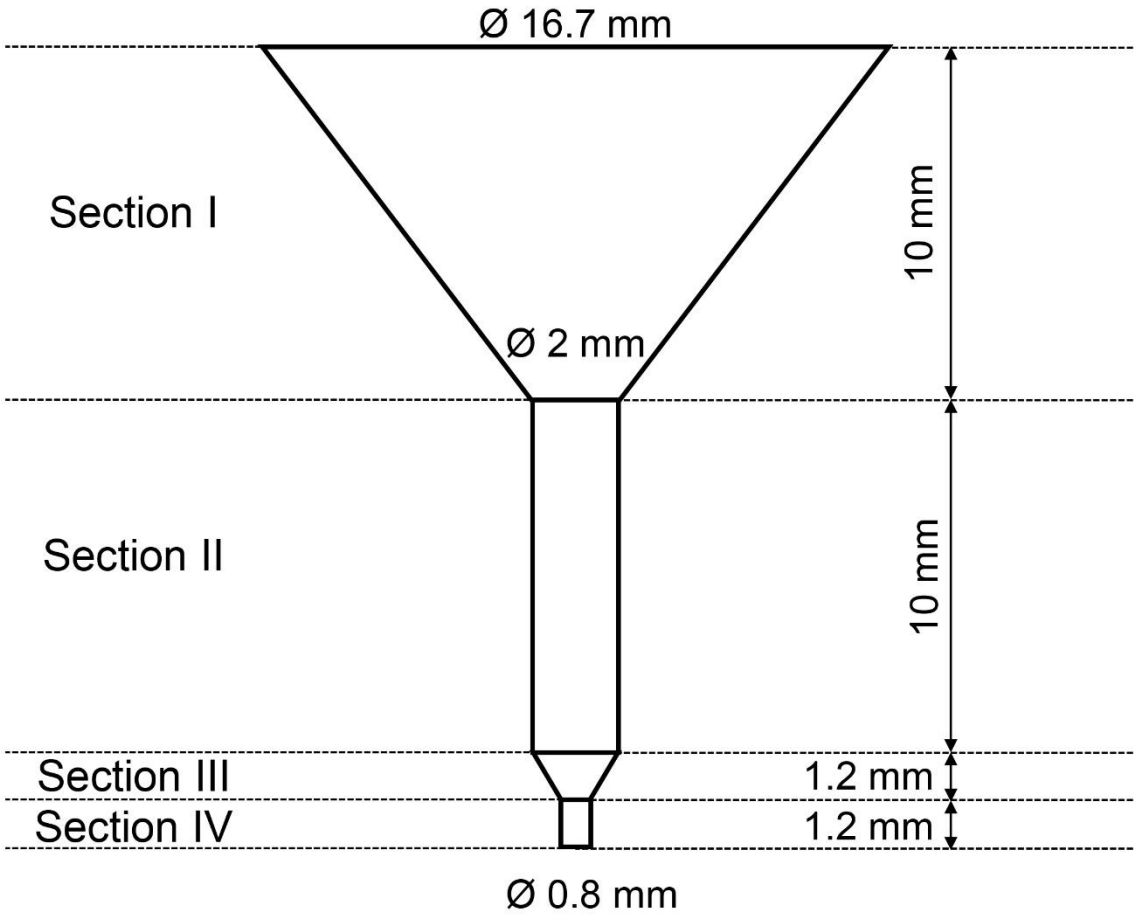


*Source: the author*

The die conductance factors (K') were calculated using Eq. 50 and Eq. 51, where R refers to radius of the circular tube, $R_o$ and $r_o$ refers to the larger and smaller radii of the cone, respectively, and l refers to the length of the section [128].

$$K'_{circular\ tube} = \frac{\pi R^{m+3}}{2^m(m+3)}\left(\frac{1}{l}\right)^m \quad (50)$$

$$K'_{conical\ bore} = \frac{\pi}{2^m(m+3)}\left(\frac{3\left(\frac{R_o}{r_o}-1\right)}{ml\left(1-\left(\frac{r_o}{R_o}\right)^{3/m}\right)}\right)^m r_o^{m+3} \quad (51)$$

The fluidity (Φ) and flow exponent (m) were calculated using Eq. 48 and Eq. 49, for the same PP grade considered in the torque calculations. Finally, the pressure drop (Δp) could be estimated by applying Eq. 47 for each section, considering the volumetric feed rate between 17.5 $mm^3/s$ and 35 $mm^3/s$. The die conductance factors and estimated values of the pressure drop are shown in Table 9.

*Table 9. Die conductance factors and estimated die pressure drop according to the volumetric throughput.*

| Die section | K' ($m^3$) | Δp (MPa) | |
|---|---|---|---|
| | | $\dot{V}$ = 17.5 $mm^3/s$ | $\dot{V}$ = 35 $mm^3/s$ |
| I | 3.61 x $10^{-11}$ | 0.14 | 0.18 |
| II | 5.94 x $10^{-14}$ | 1.16 | 1.46 |
| III | 9.76 x $10^{-13}$ | 0.35 | 0.44 |
| IV | 2.58 x $10^{-14}$ | 0.87 | 1.09 |
| Total pressure drop (MPa) | | 2.52 | 3.16 |

*Source: the author*

As mentioned, a Nema 17 stepper motor had been initially considered to drive the twin screw at 10 rpm. However, due to the estimated value for the total processing torque (ranging from 3.4 N·m to 4.2 N·m at 50 rpm and 100 rpm, respectively), it was decided to use a Nema 23 stepper motor, model KTC-HT23-401 (Kalatec Automation, Brazil), and a 10:1 speed reducer (model PEII 050 – 010, Apex Dynamics Inc., USA) supporting a maximum torque of 18 N·m.

One of the main challenges of designing a small Co-TSE is the short distance between the screw shafts (A = 10.2 mm), which considerably limits the size of the driving components. In industrial Co-TSE machines, one screw shaft can be directly coupled to the motor, while two torsion shafts are used to drive the second screw. If the necessary torque is not achieved in a single reduction stage, two additional torsion shafts can be used on the first screw shaft [37]. Although the torsion shafts allow relatively small gears to withstand high torque levels, this technical solution would result in a complex and too large transmission system. In fact, any solution based solely on gear transmission seemed unfeasible due to the insufficient strength of the small teeth of at least one of the pinions.

An alternative transmission solution based on belt driving was proposed. Figure 52 shows the general design, in which a third shaft is used to drive both screws. For the sake of simplicity, the transmission ratios are the same in the upper and lower stage. Therefore, the driven and driver pulleys have the same pitch diameter ($PD_1$ for the driven pulleys, and $PD_2$ for the driver pulleys).

*Figure 52. Schematic view of the transmission system design based on belt driving.*

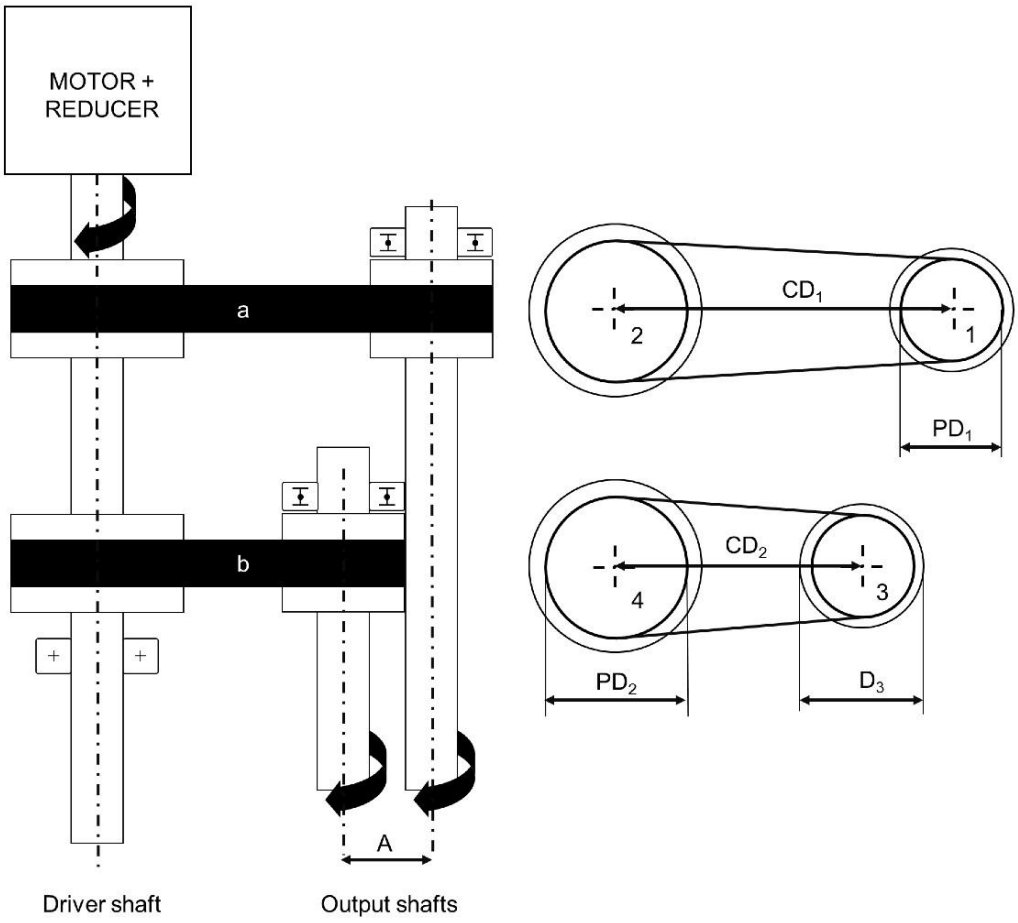


*Source: the author*

For any pair of pulleys, the belt perimeter ($L_p$) is determined by Eq. 52 in function of the center distance (CD) and pitch diameters (PD) [129].

$$L_p = 2CD + 1.57(PD_2 + PD_1) + \frac{(PD_2 - PD_1)^2}{4CD} \quad (52)$$

The maximum hub diameter of the lower driven pulley ($D_3$) is limited by the centerline distance between the screws (A = 10.2 mm) and by the diameter of the output shaft on the right. Considering 7 mm diameter output shafts, $D_3$ should be smaller than 13.4 mm. Therefore, 12-MXL-025 timing pulley ($PD_1$ = 7.8 mm) with 12.2 mm hub diameter was selected. For the driver shaft, the 24-MXL-025 timing pulley ($PD_2$ = 15.5 mm) was selected. For the pre-selected 520-

MXL-K timing belt ($L_{p,b}$ = 132.1 mm), Eq. 52 was applied to calculate the center distance between the pulleys of the lower transmission stage ($CD_2$ = 47.6 mm). The center distance between the pulleys of the upper transmission stage ($CD_1$) is equal the distance between the pulleys of the lower stage plus the distance between the output shafts ($CD_2$ + A). Once the distance between the upper pulleys was known ($CD_2$ = 57.8 mm), it was possible to calculate the perimeter of the remaining belt ($L_{p,a}$) by applying Eq. 52 again. Thus, the belt selected was the 600-MXL-K ($L_{p,a}$ = 152.4 mm).

The second version of the Co-TSE AM system is shown in Fig. 53a. A gantry structure is used to support the print head, which is now fixed due to weigth and inertia considerations. The positioning system (not shown) would move the build platform in the three axes. The embodiment also presents a lateral cooling fan to help control the feeding zone's temperature. The updated design of the Co-TSE print head is featured in Fig. 53b. It shows the drive unit formed by the Nema 23 stepper motor, planetary speed reducer, and belt transmission box. The material would be poured laterally into the barrel by the volumetric feeder. The single-part barrel was also modified to a clamshell design, to facilitate screw removal and cleaning.

*Figure 53. Second version of the Co-TSE AM system: (a) overall design and (b) detailed view of the print head.*

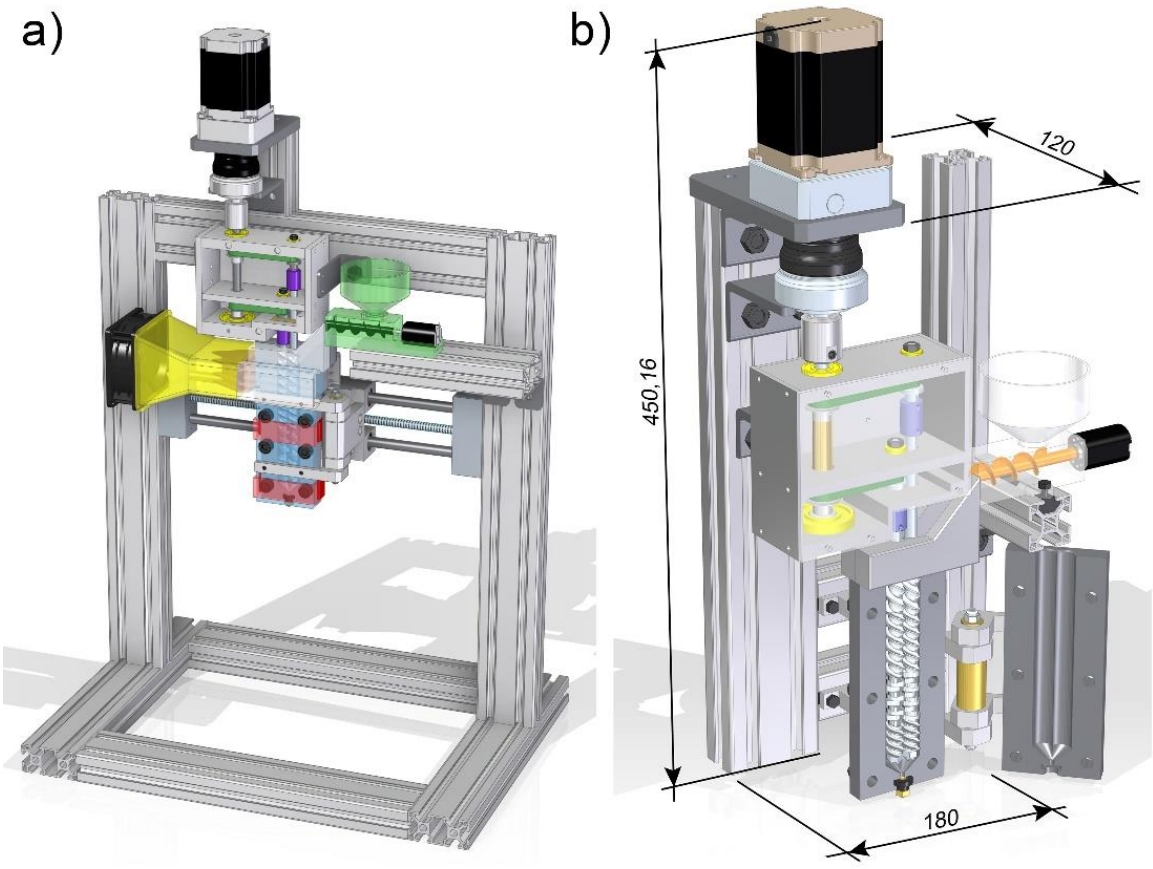


*Source: the author*

The updated screw elements were made by the SLM machine mentioned in the previous section, using the same Co-Cr-W alloy. The parts were made with excellent geometric fidelity in a very short time (around 9 hours). After printing, the screw modules were sanded and polished with the aid of a Dremel rotary tool. The best surface quality was obtained using aluminum oxide mounted points. Figure 54 displays the various fabrication stages of the screws elements.

*Figure 54. Fabrication stages of the screw elements: (a) SLM printing, (b) set of printed conveying elements, (c) close view of the rough surface of the printed elements, (d) conveying elements after post-processing.*

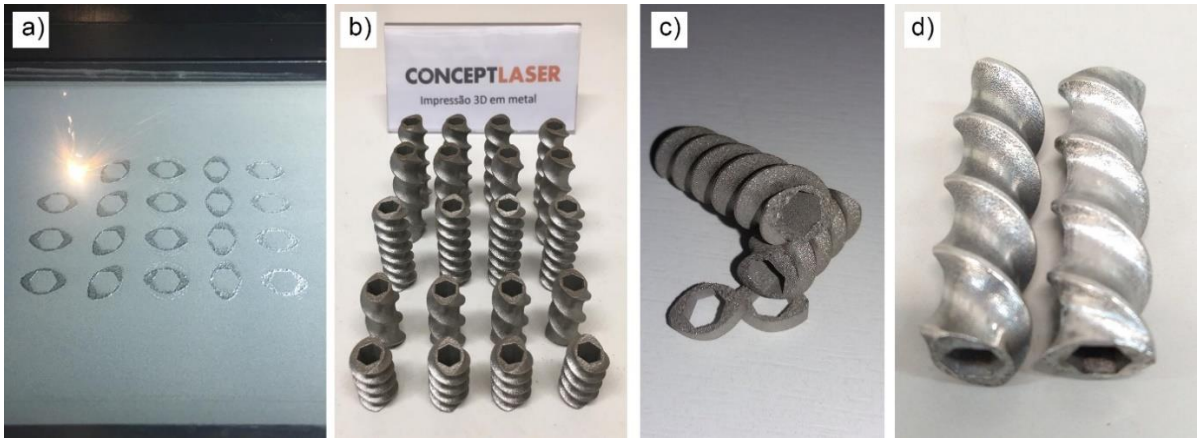


*Source: the author*

FFF was used to produce a first prototype with the transmission solution (see Fig. 55a) and barrel (Fig. 55b), for kinematic validation. The actual barrel was made by die-sink electrical discharge machining (EDM), in partnership with the Faculty of Engineering of the University of Porto (FEUP). The complete prototype is shown in Fig. 55c, and was tested with silicone oil to simulate the behavior of a molten polymer. A transparent copy of the barrel was also made (see Fig. 55d), to better visualize the rotating screws.

*Figure 55. Prototype building stages at the end of the second design iteration: (a) transmission box housing made by FFF, (b) barrel made by FFF, (c) clam-shell barrel made by die sink EDM, (d) transparent barrel made by resin casting.*

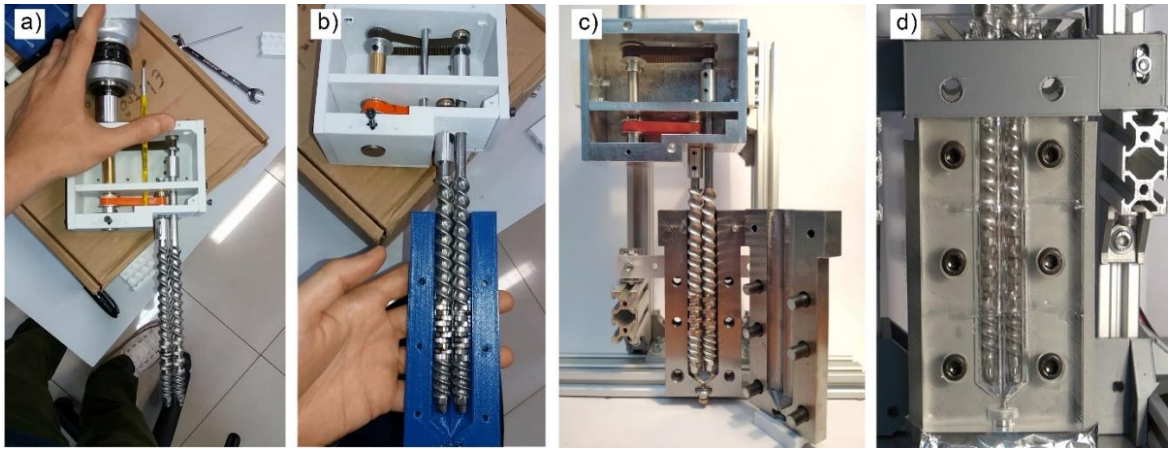


*Source: the author*

Altough the belt transmission was able to drive the twin screw, it failed to provide the torque necessary to transport the silicone oil when the barrel was filled. The failure was attributed to the tendency of the MXL belt slip in the pulleys, as well as to the lack of/or poor support of the screw shafts.

## 4.3 Third design iteration

A third iteration was necessary to correct the problems observed in the preliminary processing tests and update the frame and positioning system of the 3D printer. The functional diagram (Fig. 56) shows a prospect of the design activities for the print head, which included redesigning the transmission system, estimating the available torque per screw, and performing numerical calculations to ascertain whether the appropriate thermomechanical environment for polymer processing could be created. The frame was designed considering the overall size of a benchtop 3D printer, and the positioning system was developed to maximize the print area and provide fast XY displacement. The electronics were set up from open-source hardware and softwares, adapted from free desktop FFF 3D printers.

*Figure 56. Functional diagram of the complete Co-TSE AM system showing the main design tasks carried on the third iteration.*

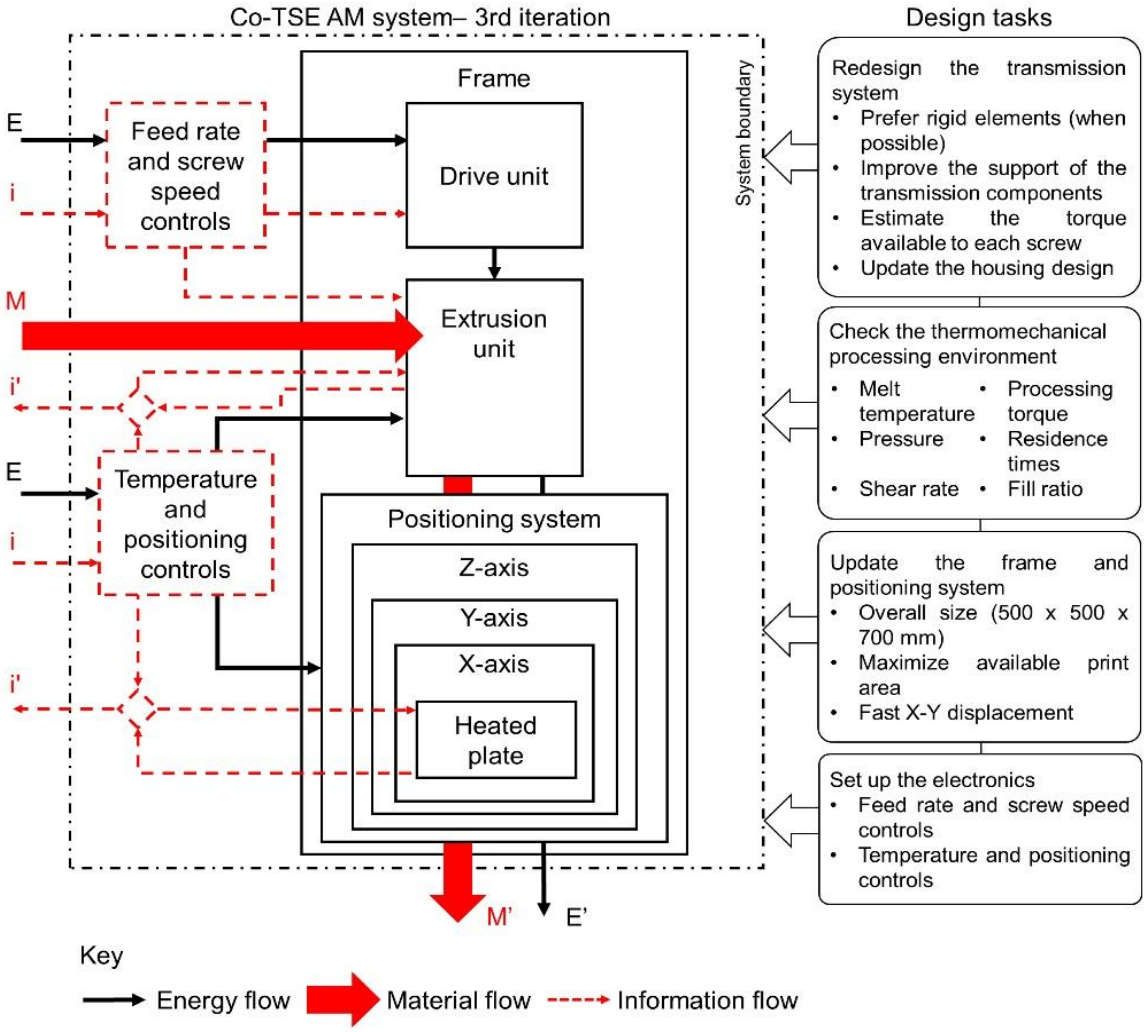


*Source: the author*

The new transmission system was composed of a simple gear train followed by a belt transmission stage. In this way, power could be transmitted from a middle driving gear to two adjacent shafts, one of which is the first output screw shaft. The remaining shaft had an attached pulley to transmit power to the second output screw shaft (see Fig. 57).

*Figure 57. Schematic view of the transmission formed by a simple gear train and a belt transmission stage.*

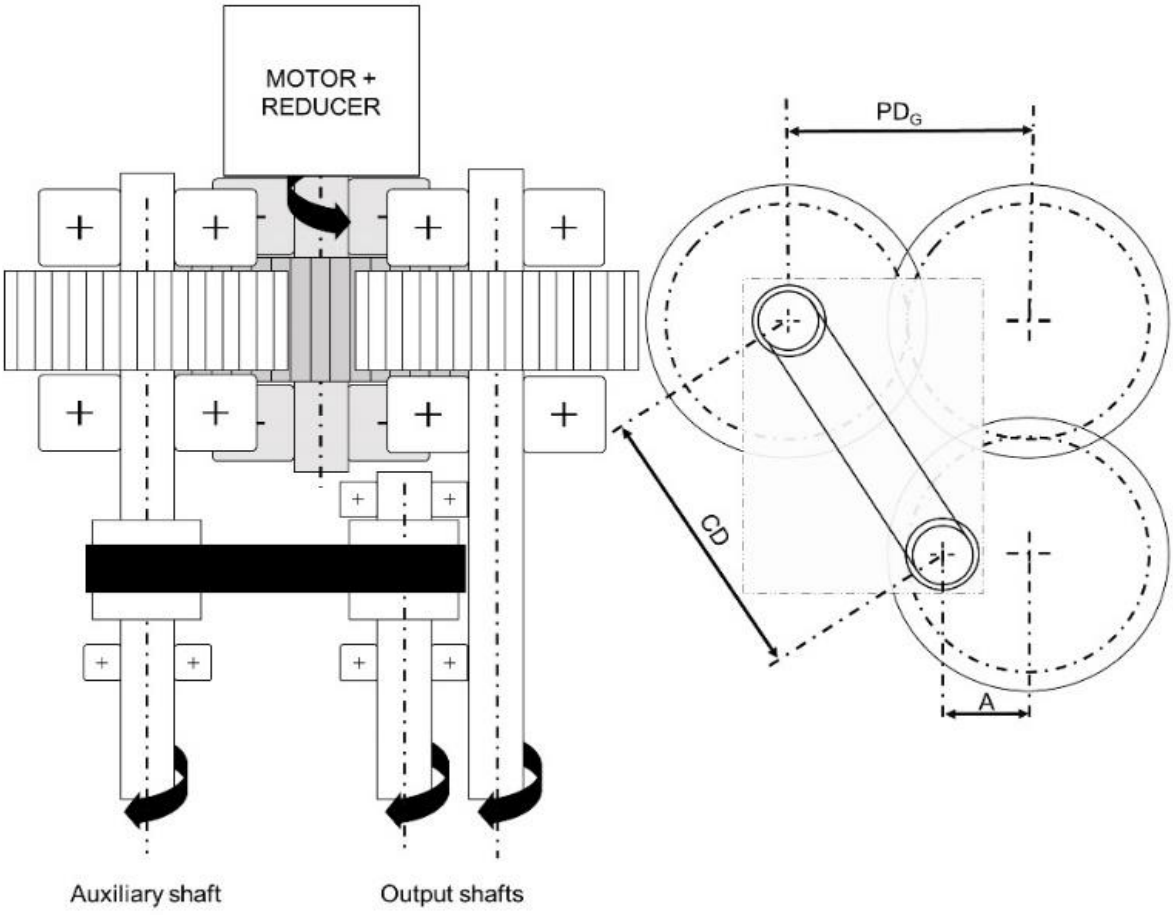


*Source: the author*

Based on the proposed disposition of the transmission elements, the distance between the pulleys (CD) was calculated in function of the pitch diameter of the gears ($PD_G$) and distance between the screws (A), as expressed by Eq. 53.

$$CD = \sqrt{\left(2PD_G \cos\left(\pi/4\right) - A\cos\left(\pi/4\right)\right)^2 + \left(A\cos\left(\pi/4\right)\right)^2} \quad (53)$$

The spur gears were designed with 25 teeth and 1.75 mm module ($PD_G$ = 43.75 mm). For the belt transmission stage, it was decided to use the GT tooth profile, which offers a better grip compared to the MXL type. Again, the external diameter of the pulley to the right is limited, so a pulley with 20 teeth and pitch diameter equal to 12.7 mm (20-GT2-6) was selected. Once the distance between the pulleys was known (CD = 55.1 mm), the new belt length could be calculated using Eq. 52. Although the resulting belt length was 150.1 mm, a slightly smaller belt (74-GT2-6, with $L_p$ =148 mm) was chosen for additional tensioning.

The torque available to each screw was estimated with the measuments made by Ito [130], who used a Prony brake apparatus. The torque values measured at the motor shaft were

multiplied by five, to account for the use of the speed reducer and the gearbox. The speed values were only divided by ten, since there is only one reduction stage. The estimated torque per screw (without considering transmission losses) is presented in Table 10.

*Table 10. Estimated torque available to each screw at different screw speeds.*

| | **Screw rotation speed (rpm)** | | | | | | | | | |
|---|---|---|---|---|---|---|---|---|---|---|
| | 10 | 20 | 30 | 40 | 50 | 60 | 70 | 80 | 90 | 100 |
| **Torque per screw (N·m)** | 9.0 | 7.5 | 6.5 | 4.5 | 4.0 | 3.5 | 3.5 | 2.5 | 1.5 | 1.0 |

*Source: the auhtor*

The numerical calculations were performed in partnership with the Department of Polymer Engineering (DEP) of the University of Minho, using the global plasticating modelling software for Co-TSE developed and validated by Teixeira et al. [25]. The simulations were used to predict the axial evolution, from feeding to the die outlet, of the main process parameters, assuming the extrusion of a generic grade of polypropylene (PP). The main physical, thermal and rheological properties of the PP grade used in the calculations are listed in Table 11.

*Table 11. Properties of the generic polypropylene grade used.*

| **Property** | | | **Value** | **Unit** |
|---|---|---|---|---|
| Density | Solids | $\rho_s$ | 560 | $Kg/m^3$ |
| | Melt | $\rho_m$ | 740 | |
| Thermal Conductivity | Solids | $k_s$ | 0.1 | W/m·ºC |
| | Melt | $k_m$ | 0.16 | |
| Specific Heat | Solids | $C_s$ | 2480 | J/kg |
| | Melt | $C_m$ | 2950 | |
| Melting | Heat | H | $60 \times 10^3$ | J/kg |
| | Temperature | $T_m$ | 170 | ºC |
| Viscosity (Carreau-Yasuda law) | | $\eta_0$ | 3500 | Pa·s |
| | | E/R | 7500 | K |
| | | $\lambda$ | 0.11 | s |
| | | a | 0.97 | |
| | | n | 0.33 | |
| | | $T_0$ | 260 | ºC |

*Source: the author*

The screw configuration tested (same as in Fig. 50) had two mixing zones, each one formed by five kneading discs staggered − 60°. 20/40, 15/40, and 10/20 conveying elements

were used for the feeding zone, melt conveying, and pressure generation upstream of the nozzle. The feed rate (Q) was stipulated as 20 g/h (Q20, 7.5 $mm^3/s$) or 40 g/h (Q40, 15 $mm^3/s$), the barrel temperature (Tb) was set to 220 °C and the screw rotation speed to 80 rpm (N80) or 100 rpm (N100).

Fig. 58 depicts depicts the evolution of (a) melt pressure and melt temperature, (b) average shear rate and cumulative torque per screw, (c) local and cumulative residence times, and (d) fill ratio along the screw axis at various operating conditions.

*Figure 58. Evolution of a) melt pressure and melt temperature, b) average shear rate and cumulative torque per screw, c) local residence time and cumulative residence time, and d) fill ratio along the screw axis under different operating conditions.*

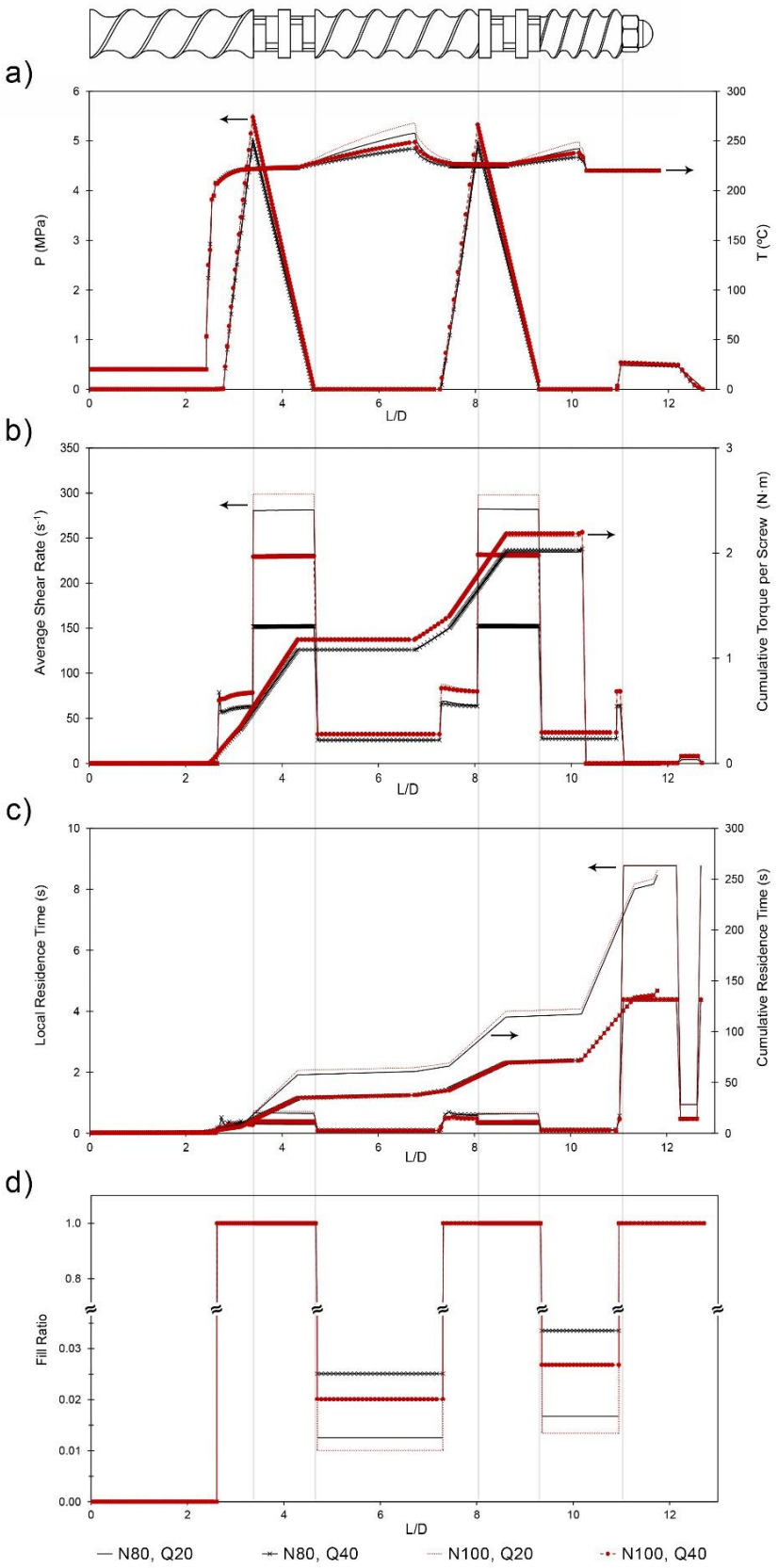


*Source: the author*

Polymer melting takes place through a combination of heat transfer and mechanical dissipation. The presence of restrictive kneading elements causes the screws to work fully filled immediately upstream, which facilitates these mechanisms. Thus, it is clear from Fig. 58a that the material melts just before attaining the first kneading block. The initial temperature increase is sharper than that observed in practice, as it is a consequence of the melting mechanism implemented in the overall plasticating model. The melt temperature tends to increase due to viscous dissipation associated with shearing. As expected, higher shear rates are produced at higher screw speeds. The shear rate is about two times higher in fully filled regions. Therefore, the melt temperature increase is more pronounced at the end of the intermediary conveying element. In addition, changes in the shape of the velocity profile cause the maximum shear rates to decrease when the feed rate increases [25]. That is why the melt temperature can reach 268 °C (for a set value of 220 °C) for the highest screw speed and lowest feed rate. Despite the temperature-dependent melt viscosity, the pressure peaks tend to increase at higher screw speeds due to the increased rate at which material is conveyed backward in the kneading blocks. The effect of the feed rate on the pressure is less marked due to the non-Newtonian character of the melt. The maximum pressures are developed upstream of the kneading blocks, and can reach 5.5 MPa when the screws rotate at 100 rpm. As expected, between the two kneading blocks, the screws work mostly partially filled, and the pressure in these regions is nil. Obviously, flow through the nozzle requires pressure generation upstream, however the value of about 1 MPa was obtained for a generic die geometry that differs from the proposed design.

Fig. 58b confirms that the shear rates in conveying zones are much lower than those in kneading blocks, not only because in the first case flow develops mostly in partially filled channels (with exception of a few downstream screw turns) but also due to the restrictive nature of the kneading elements. As their conveying capacity is limited, the melt is forced through very narrow gaps between the discs. As discussed before, shear increases with increasing screw speeds, but decreases with increasing feed rates. The shear rates range from about 150 - 300 $s^{-1}$, matching well the range of rates created in a larger Co-TSE [25]. The figure also demonstrates the crucial importance of the restrictive zones to the overall required torque (the value attaining 2.2 N·m with the screws at 100 rpm). The behavior of the cumulative torque follows the same trends as the pressure.

Obviously, the higher the feed rate and the higher the screw speed, the lower the residence time (Fig. 58c). Again, the contribution of restrictive zones to this parameter is paramount. The results show that doubling the output leads to a decrease in the residence time

of about 45 %. In turn, the effect of the screw speed is much less pronounced due to the proximity of the values simulated. Besides the feed rate and screw speed, the residence times are related to the extruder L/D. Typical Co-TSE have L/D ranging from 30 to 40, and operate at accordingly much higher feed rates and screw speeds. Considering the proposed L/D ratio and the operating conditions, the cumulative residence times range from 140 to 260 s, which fall within the range observed in larger extruders.

As shown in Fig. 58d, the screws work fully filled (fill ratio of 1) in restrictive sections (where pressure and average shear rate rise), while the fill ratio is actually low in the conveying sections within the experimental range of outputs and screw speeds utilized. This promotes local distributive mixing and short residence times.

The positioning system was designed with all movements attributed to the build platform. A coreXY design was used for the displacement in the XY plan (Fig. 59), as it allows the positioning system to be more compact and easily adjusted to the gantry structure. Besides, rapid accelerations are favoured [131]. For the vertical motion, a mechanism with two lead screws (THSL-500-2D) guided by linear ball bearings (LM8UU) and 8 mm diameter shafts positioned at the four corners of the CoreXY frame was proposed. Again, 20-GT2-6 pulleys were selected, together with open GT2-6 timing belts. The Nema 17 stepper motors (model US17H4401, Usongshine Inc., China) were selected to drive the positioning system.

*Figure 59. Representation of the CoreXY mechanism.*

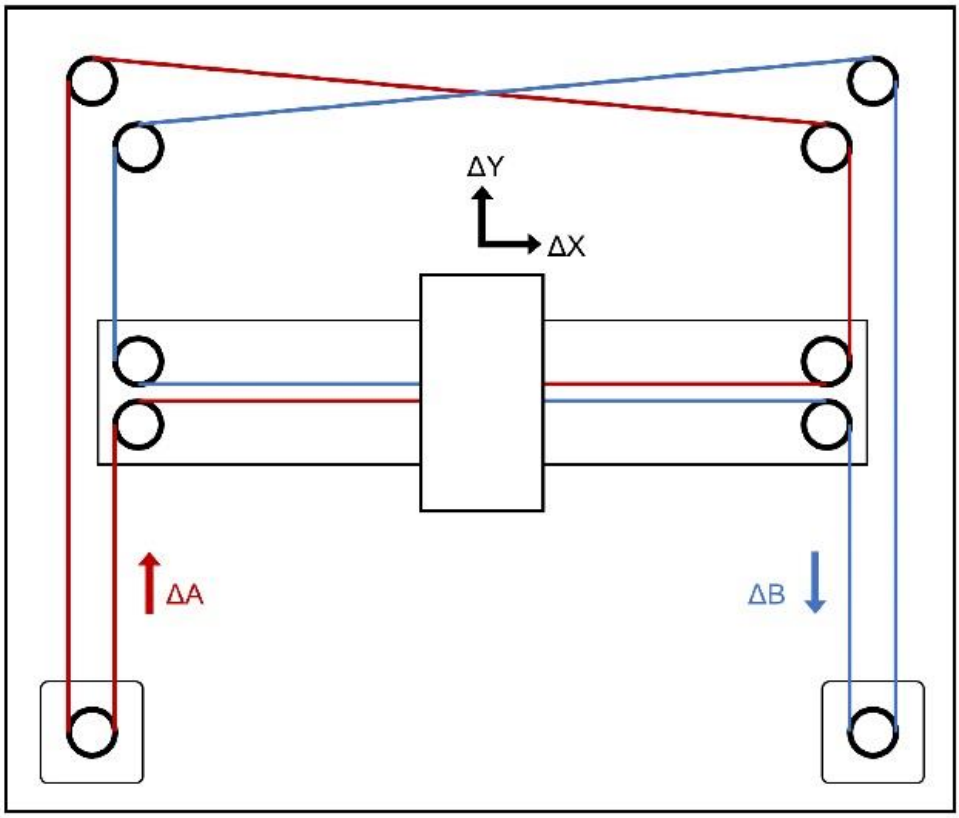


*Source: adapted from [129]*

Figure 60 presents final version of the Co-TSE AM system, with detailed views of its three major subsystems: the extrusion unit, drive unit, and frame and positioning system. The barrel of the extrusion unit was modified to a segmented design to facilitate manufacturing and assembly. The segment upstream contains a feeding ramp that directs the material from the feeder into one screw. The bottom side is separated from the adjacent barrel segment by a PTFE insulating barrier, in order to prevent premature polymer melting, whereas the top part allows fixing the barrel assembly to the structure. The interchangeable extrusion nozzle is threaded to the barrel segment downstream. The volumetric feeder was also updated to a more compact design, with a 45 mm long screw (12 mm diameter), tubular barrel, and a hopper with 75 $cm^3$ storage capacity. The feeder screw is driven by a Nema 17 stepper motor (US17H4401, Usongshine Inc., China). The drive unit was designed with an open housing, to allow better visualization upon testing. A 165 x 165 mm heated plate (manufactured by Prelo3D LTDA, Santa Catarina, Brazil) was acquired for the build platform. The resulting available print volume was 55 x 80 x 43 mm, which is enough for the intended benchtop applications of the Co-TSE AM system.

*Figure 60. The Co-TSE AM system: (a) the complete 3D printer and (b) its major subsystems.*

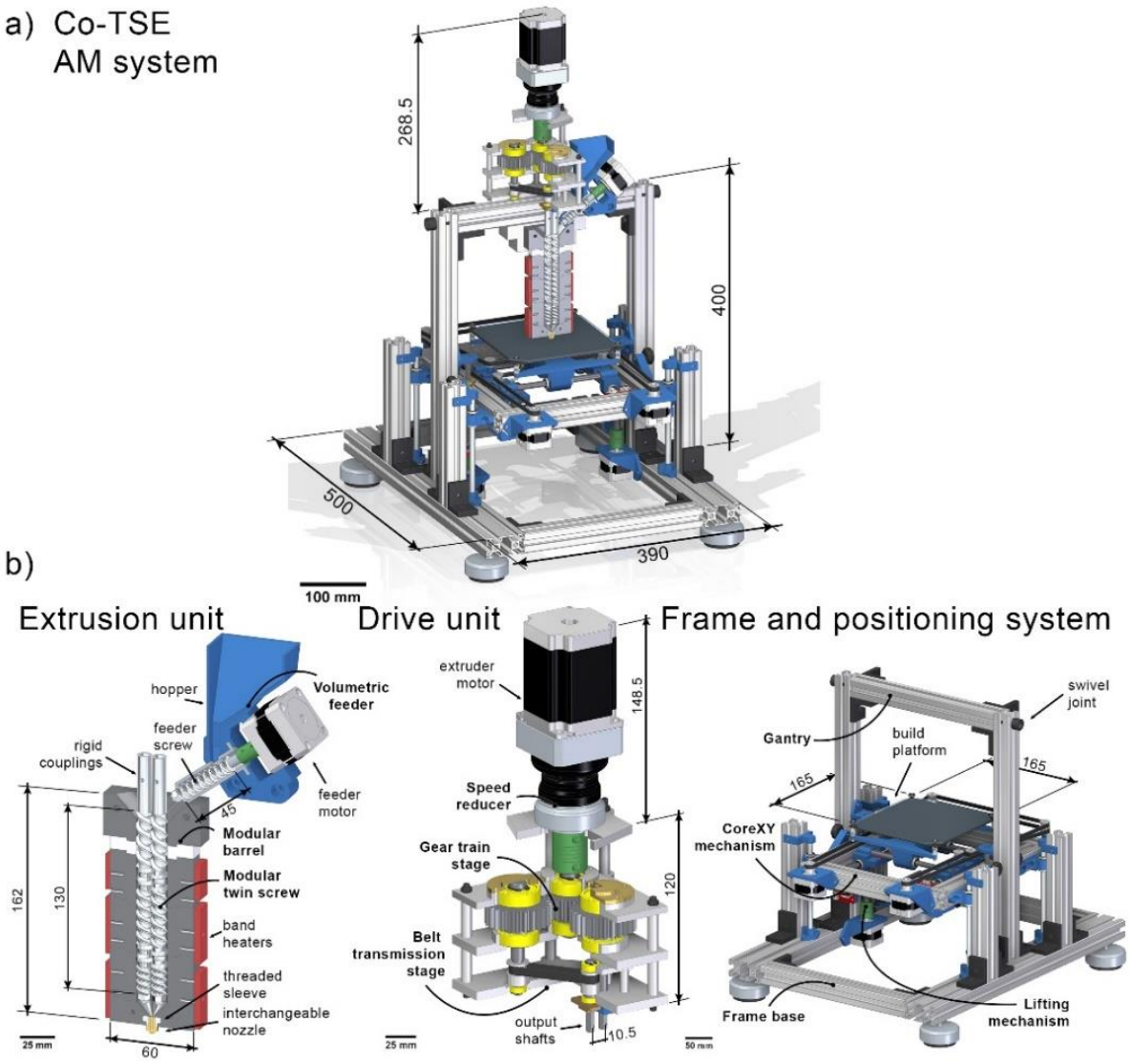


*Source: the author*

Instead of machining the screw shafts as in the second iteration, two long allen wrenches were acquired and cut into the required length. The rigid sleeves, specially designed to facilitate coupling with the drive unit as well as to guarantee the correct relative positioning of the screws, were made by direct metal laser sintering (DMLS) in an EOSINT M280 machine (EOS GmbH, Germany) using maraging steel. After polishing, the sleeves were glued to the hexagonal shafts using a permanent adhesive (TekBond 120, Tekbond, Brazil). Figure 61 shows the rigid couplings as 3D printed, after post-processing and glued to the Allen wrenches.

*Figure 61. Fabrication stages of the rigid couplings: a) parts as obtained from the DMLS process b) polished coupling, c) couplings mounted to the screw shafts.*

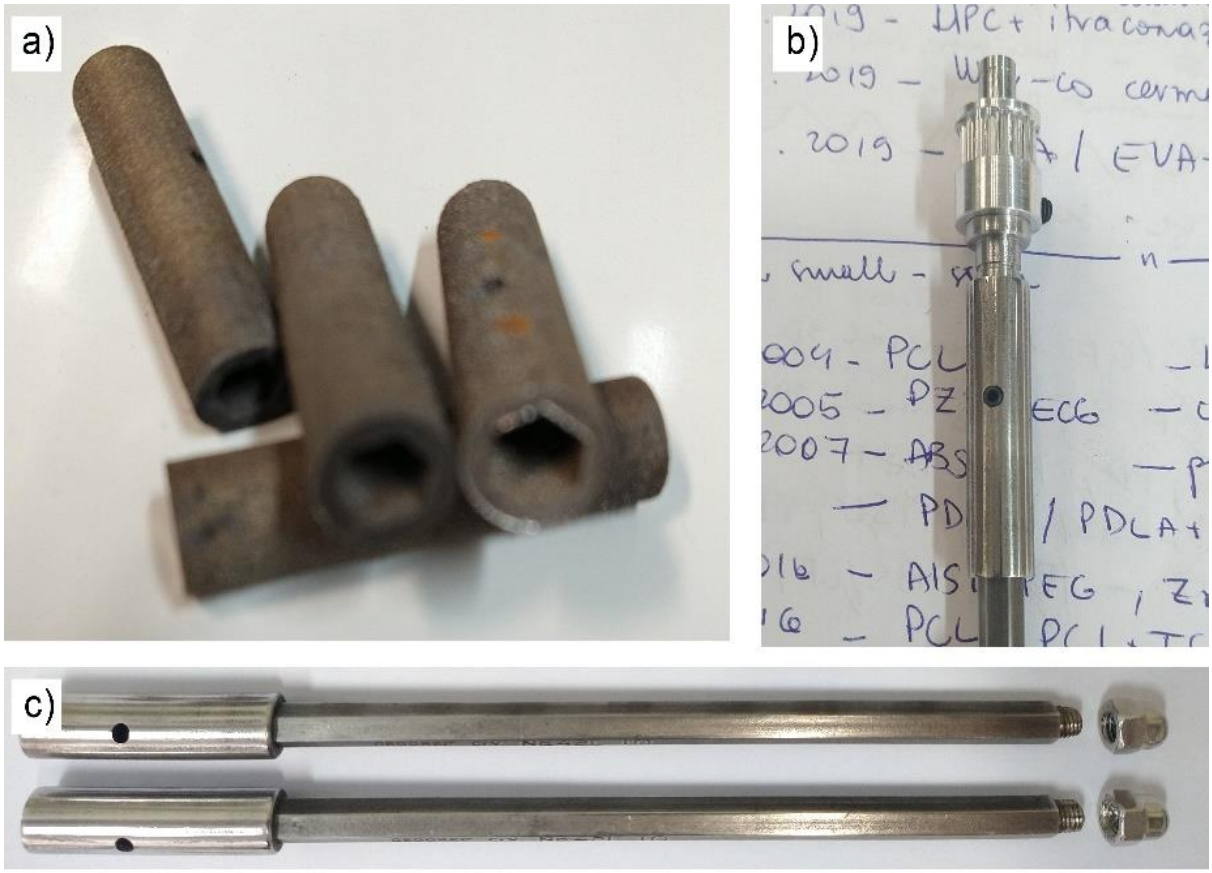


*Source: the author*

The cavities of the the barrel segments (shown in Fig. 62) were made by wire-cut EDM. The remaining components of the print head were obtained by conventional machining processes. The main frame and positioning system were put together from commercially available parts, with some specific components obtained by FFF. The gantry was made with a manual swivel mechanism to position the print head assembly in the horizontal, facilitating screw and barrel removal. The assembly sequence of the platform and final aspect of the Co-TSE AM system (shown in two positions to evidence the use of the swivel mechanism) are presented in Fig. 63.

*Figure 62. Barrel modules, insulating PTFE segment and threaded sleed with the deposition nozzle.*

*Source: the author*

*Figure 63. Platform assembly sequence: (a) frame components, (b) gantry, (c) coreXY mechanism, (d) platform without the print head, (e) Co-TSE AM system in operation position, (f) Co-TSE AM system in maintenance position.*

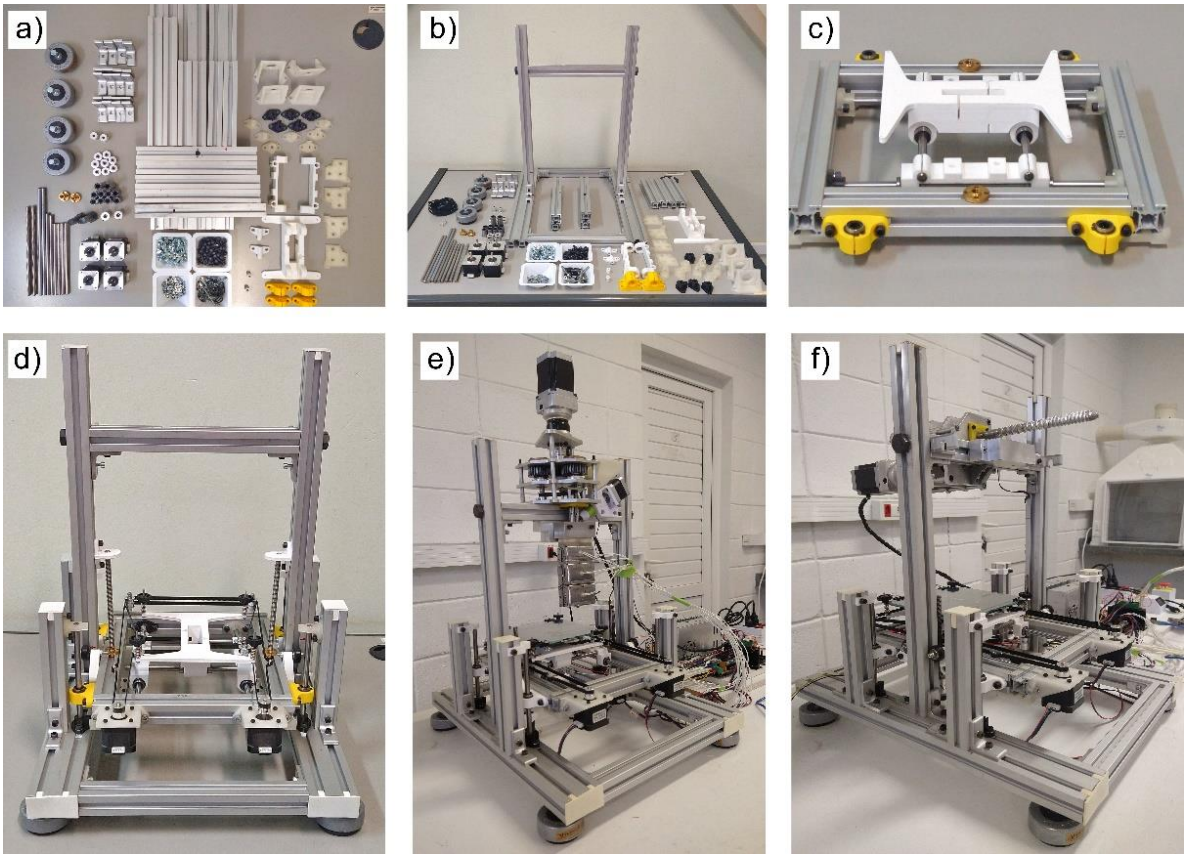


*Source: the author*

The circuit used to control the drive unit and volumetric feeder (Fig. 64a) comprised a direct current (DC) power supply, an Arduino Uno (Arduino, Massachusetts, USA), and stepper motor drivers. The WD-2404 driver (manufactured by Wotiom, Brazil), is used for the Nema 23 motor, which operates in 1/16 microstepping mode, and the DRV8825 driver (Pololu, Nevada, USA) is used for the Nema 17 motor, operating in 1/2 microstepping mode. The Arduino IDE code used to set the speed of the motors is transcribed in Appendix B. Figure 64b shows the circuit used to control the positioning system and the temperature of the build platform and extruder heaters. The setup consists of a RAMPS 1.4 shield, which was adapted to the project. The first heating zone of the extruder (close to the feeding zone) uses a pair of 60 W power band heaters associated to thermistor T2. The second heating zone uses two pairs of 100 W heaters, associated to thermistor T1. Thermistor T0 is used to control the heated build platform. A modified version of the Marlin firmware was loaded to the RAMPS, so that g-code commands generated by a commercial slicing program (Repetier-Host) could be used to control the position and temperature of the build platform as well as the temperature of the heating zones.

*Figure 64. Electrical circuits used to control a) the drive unit and feeder, b) the position and temperature of the build platform and of the extruder heating zones.*

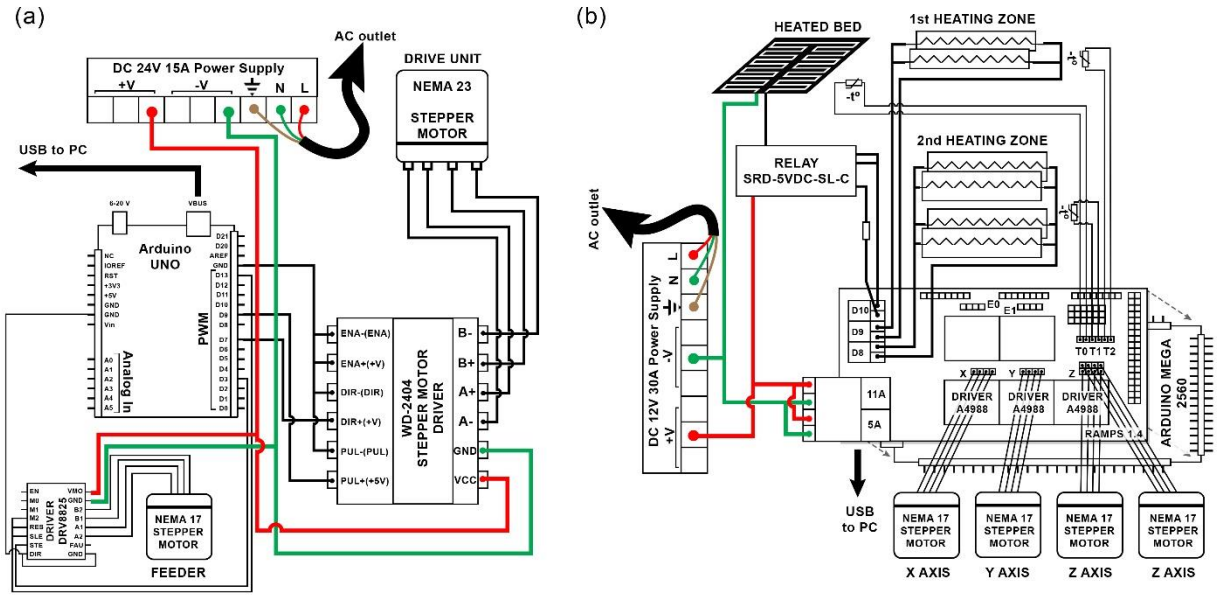


*Source: the author*

# 5 EXPERIMENTAL VALIDATION

Before testing the equipment, the volumetric feeder was calibrated with the material used. Polypropylene copolymer (grade RP141 manufactured by Braskem, Brazil, for injection molding applications), was ground in a Mikro Bantam hammer mill (Hosokawa Micron Powder Systems, USA) after immersion in liquid nitrogen, to yield powder with particle size ranging from 300 to 600 μm. The differential thermogram and the flow curves at low shear rates obtained for the PP grade used are presented in the Appendix C. Fig. 65 shows the linear correlation obtained between feed rate (g/h) and the feeder screw speed (rpm).

*Figure 65. Feed rate versus feeder speed for the PP micro-pellets.*

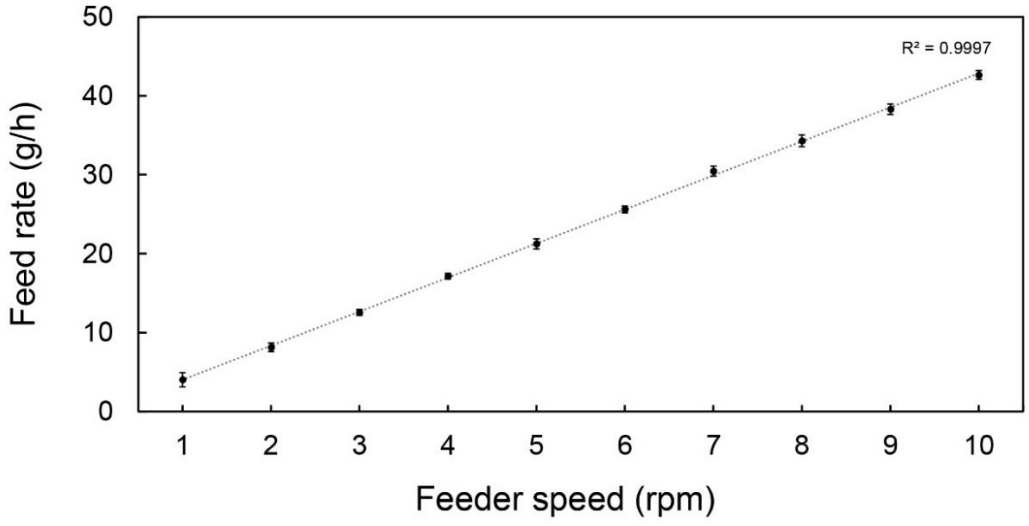


*Source: the author*

Extrusion tests were performed to assess the response of the extrusion unit in terms of flow characteristics and mixing performance. Besides the screw geometry simulated in Section 4.3 (configuration 1), an alternative conveying screw without kneading discs (configuration 2) was also used. The screw configurations are presented in Table 12. The temperatures of the first and second heating zones were set to 180 ºC and 210 ºC, respectively. The tests were performed with a 0.6 mm diameter brass 3D printing nozzle.

*Table 12. Screw configurations tested.*

| Screw configuration | Element | | | | |
|---|---|---|---|---|---|
| 1 | 20/40 | KB -60/5/15* | 15/40 | KB -60/5/15* | 10/20 |
| 2 | 20/40 | 15/40 | 10/30 | 10/20 | |

*The kneading blocks (KB) are identified as stagger angle/number of discs/total length

*Source: the author*

The capacity to set output and screw speed independently and operate under steady state was demonstrated simply by weighing the extruded material collected at one-minute intervals, at different processing conditions (screws rotating at 40 rpm and 80 rpm, feed rates of 20 g/h and 40 g/h). Based on the numerical calculations for screw 1, the maximum screw speed tested was 80 rpm to avoid stalling due to insufficient torque at 100 rpm. The feed rates were stipulated so that the average shear rate at the kneading blocks could reach at least 100 $s^{-1}$. The linear relationships depicted in Fig. 66 and the virtual overlapping of the graphs for the two screw configurations demonstrate the validity of the assumption.

*Figure 66. Mass output at different screw rotation speeds and feed rates for a) configuration 1 and b) configuration 2.*

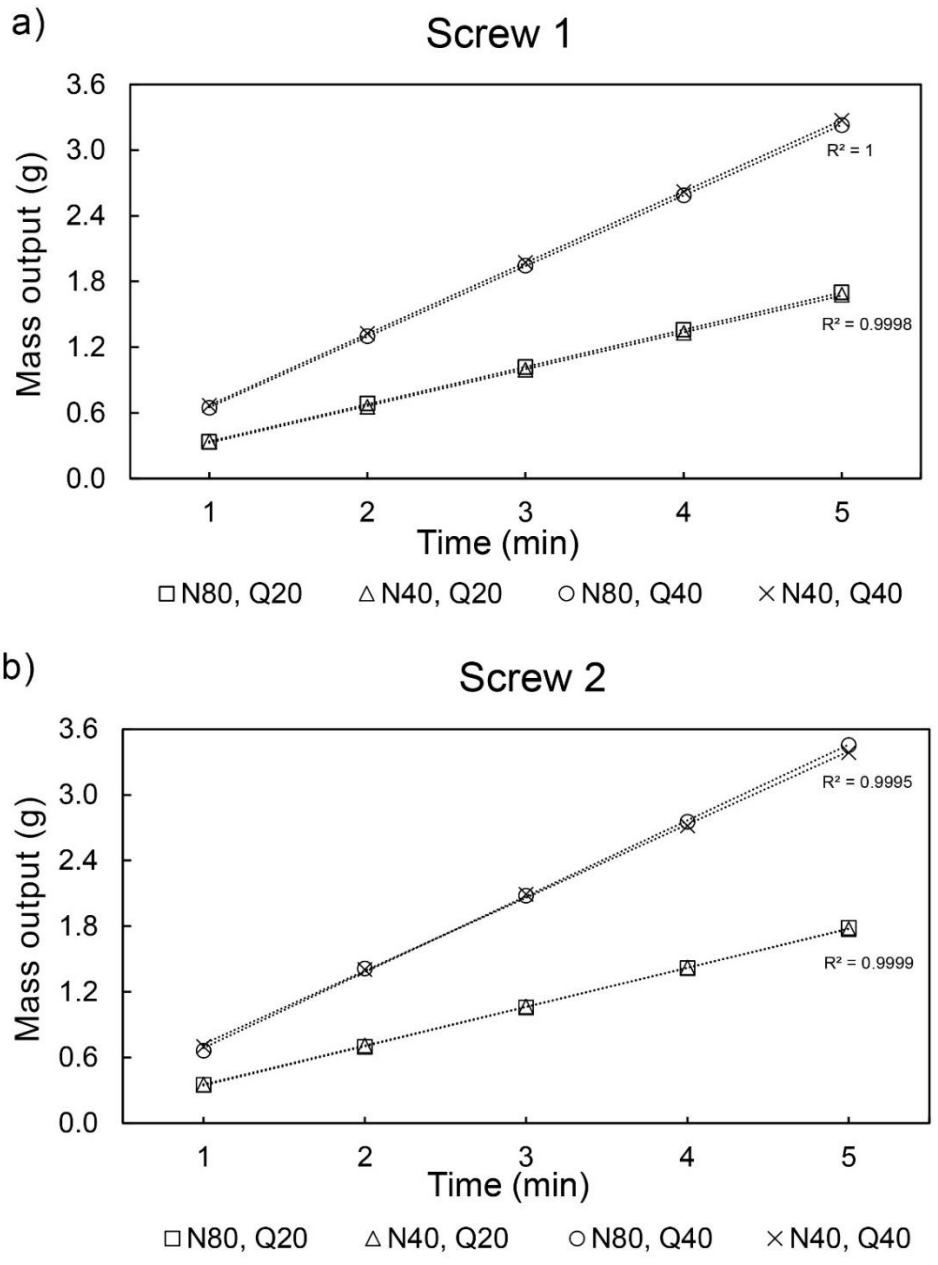


*Source: the author*

Figure 67 shows the results of pull-out experiments performed with the two screw configurations. They consisted in interrupting steady state extrusion by stopping the feeder and screw rotation and removing the barrel as quickly as possible. As seen in Fig. 67a, solid particles survived only up to the start of the kneading zone upstream, as predicted numerically in Section 4.3. As the restriction to flow created by the discs forced the screw channels to become fully filled, heat transfer became more efficient, promoting melting. In the case of configuration 2, *i.e.*, in the absence of kneading discs (Fig. 67b), the degree of screw filling increased progressively downstream due to the geometry of the conveying elements. When the screw finally became fully filled, melting took place, but much later than for configuration 1. The figure also shows that the screw length available for mixing the molten material before flow through the nozzle is much higher for configuration 1 (and will be further promoted by the presence of a second kneading zone).

*Figure 67. Screw pull-out experiments evidencing the influence of the screw configuration on the melting location: (a) configuration 1; (b) configuration 2.*


*Source: the author*

The cumulative residence times were estimated by feeding a small amount of a red tracer directly to the co-rotating screws during steady state extrusion, and measuring the time elapsed until a color change could be visually detected in the extrudate. In fact, this procedure identifies the minimum residence time. However, given the typical shape of residence time distribution curves for Co-TSE, the values obtained should not be too different from average residence times [132]. As expected, the experimental residence times for screw configuration 1 are higher than for the non-restrictive configuration 2 for all processing conditions. Although a direct comparison with the numerical predictions made in Section 4.3 cannot be made as different residence times are involved, Table 13 shows the same dependency of residence time on the operating conditions for screw configuration 1.

*Table 13. Influence of operating conditions on the residence times in the extruder.*

| Screw configuration | Screw speed (rpm) | Feed rate (g/h) | Minimum residence time (s) |
|---|---|---|---|
| 1 | 40 | 20 | 355 |
| | | 40 | 265 |
| | 80 | 20 | 264 |
| | | 40 | 198 |
| 2 | 40 | 20 | 256 |
| | | 40 | 197 |
| | 80 | 20 | 189 |
| | | 40 | 139 |

*Source: the author*

The dispersive mixing capacity of the extruder and its dependence on the operating conditions were investigated by processing an immiscible blend of polypropylene and polystyrene (PS). The same PP used above was pre-mixed with 10 wt% of PS N1921 (Innova, Brazil), and fed to the extruder at 20 g/h using screw configurations 1 and 2. Samples of the extruded filaments along their length were collected and fractured after immersion in liquid nitrogen. The fractured surface of the samples was etched in acetone at room temperature for 3 h to remove the PS phase. The samples were sputter coated with gold and subjected to scanning electron microscopy (SEM) analysis, using a Leo 440 instrument (Zeiss, Germany). Figure 68 shows the morphologies observed by SEM, where the dark holes and circular contours correspond to the PS domains that were dispersed in the PP matrix.

*Figure 68. Morphology of PP/PS 90/10 blends obtained by different processing conditions: (a) screw 1, 40 rpm; (b) screw 1, 80 rpm; (c) screw 2, 40 rpm; (d) screw 2, 80 rpm.*

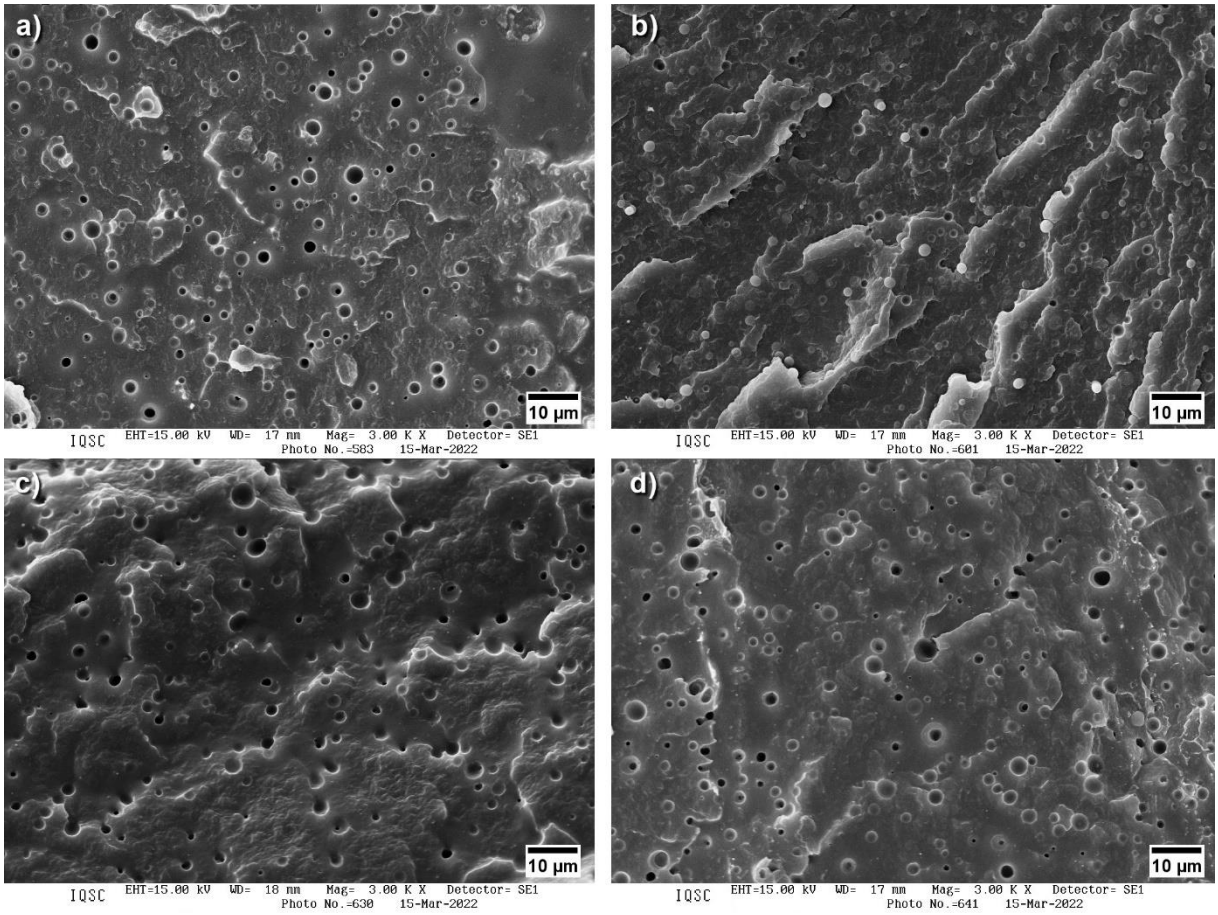


*Source: the author*

The size of the PS droplets was analysed using the software Image J. The analysis was made with 4–5 SEM images for each processing condition, allowing to identify at least 500 particles per treatment. The diameter of each droplet ($d_i$) was calculated from the corresponding area identified by the software and registered in histograms. The number-average diameter ($d_n$), volume-average diameter ($d_v$), and polydispersity (P) were calculated by the Eq. 54-56 [133]:

$$d_n = \frac{\sum_{i=1}^{N} n_i \times d_i}{\sum_{i=1}^{N} n_i} \tag{54}$$

$$d_v = \frac{\sum_{i=1}^{N} n_i \times d_i^4}{\sum_{i=1}^{N} n_i \times d_i^3} \tag{55}$$

$$P = \frac{d_v}{d_n} \tag{56}$$

The resulting histograms of PS droplet diameter distribution together with the calculated $d_n$, $d_v$ and P are shown in Fig. 69. For screw configuration 1, it is clear from Fig. 69a and b that increasing the screw speed from 40 to 80 rpm caused a general reduction of the droplet diameter

and a narrower size distribution, evidencing the improved dispersive mixing that can be achieved with the kneading discs. Screw configuration 2 produced a size distribution only marginally coarser than that observed for configuration 1 at 40 rpm, but there was no improvement with increasing screw speed.

*Figure 69. Histograms of the PS droplet diameters in the PP/PS 90/10 blends processed with a) screw 1 at 40 rpm, b) screw 1 at 80 rpm, c) screw 2 at 40 rpm, d) screw 2 at 80 rpm.*

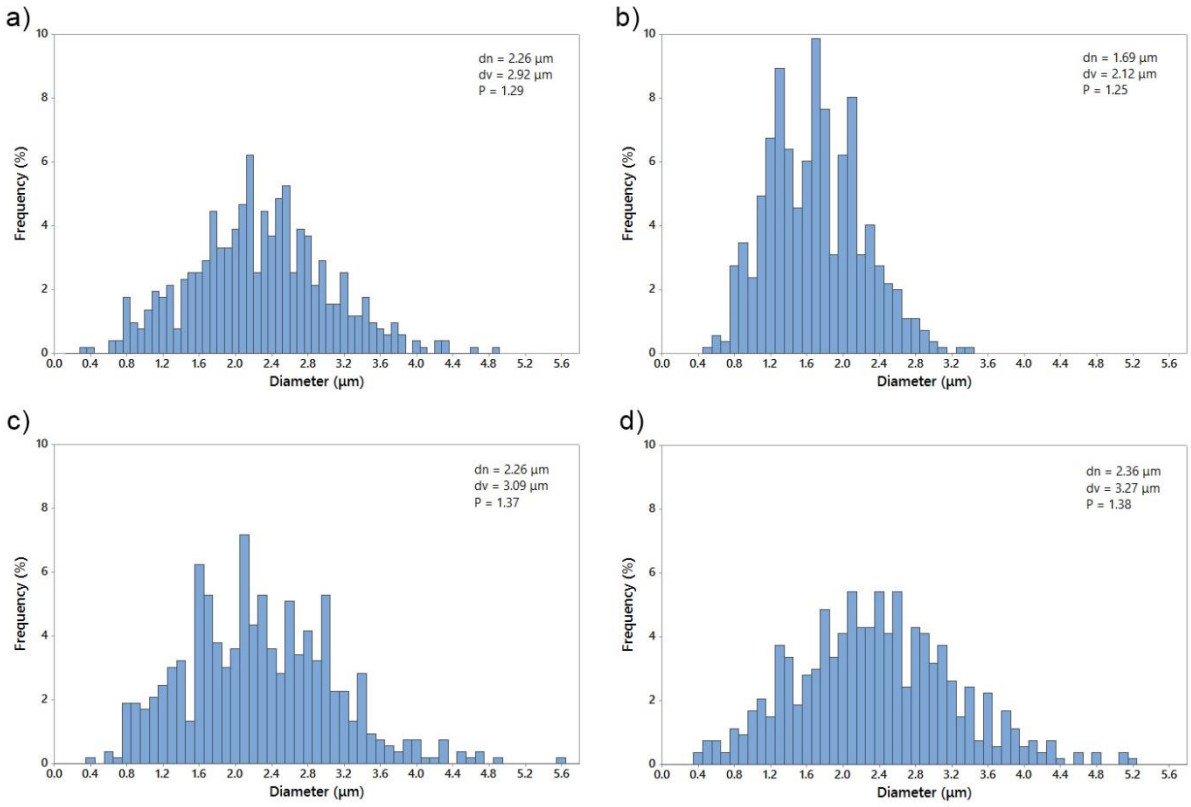


*Source: the author*

Finer dispersion was achieved with configuration 1 at 80 rpm due to the capacity of the downstream kneading element to force the melt through the gap between the edge of the discs and the barrel wall. The negative staggering angle increases such effect as material recirculates around the discs. The kneading blocks create intense shear and elongational flows, the latter being particularly effective in breaking liquid droplets [22,37]. It is worth noting that, since a minimum shear stress must be exceeded to break the PS droplets, the role of screw speed was crucial. Therefore, for mixing/dispersion purposes, configuration 1 is better. Without the restrictive elements, processing with configuration 2 not only shifts melting downstream the screws, but also fails to induce the flow forces necessary to disperse the second phase component. The configuration 2, however, can be used when dispersion is not critical. Besides

its low mixing capacity, the minimum residence times achieved with screw 2 are generally smaller, which can be positive when processing heat and/or shear sensitive materials.

Overall, the results from the extrusion tests demonstrate that the Co-TSE print head is potentially much more versatile than similar-sized single screw extrusion units developed for 3D printing. Thanks to the starve-feeding regime and screw modularity, its output is decoupled from the screw speed, and the effective screw length, residence times and mixing intensity can be tailored according to the intended application.

Besides, as widely recognized in the extrusion-related literature, the co-rotating twin screw extrusion offers much better mixing performance than equivalent single screw extruders (with similar diameter and length, operating in analogous conditions). As discussed, this is mostly attributed to the elongational flows created in the kneading zones, which are difficult to be achieved even with specialized mixing sections in single screws extruders [22,37].

Deposition tests were performed to determine the feasible speed range of the build platform ($v_b$) and characterize the uncompressed geometry of the roads. A simple G-code routine for line depositions was created and executed under various speeds with the extrusion output at 20 g/h. Screw configuration 1 was used, operating at 80 rpm. For better adhesion, the build platform was covered with PP adhesive tape and heated to 80 ◦C. The nozzle was kept 1 mm above the printing surface to avoid contact with the deposited roads. The resulting line depositions are shown in Fig. 70.

*Figure 70. Line depositions obtained at different build platform speeds, with 20 g/h output, 80 rpm, screw configuration 1.*

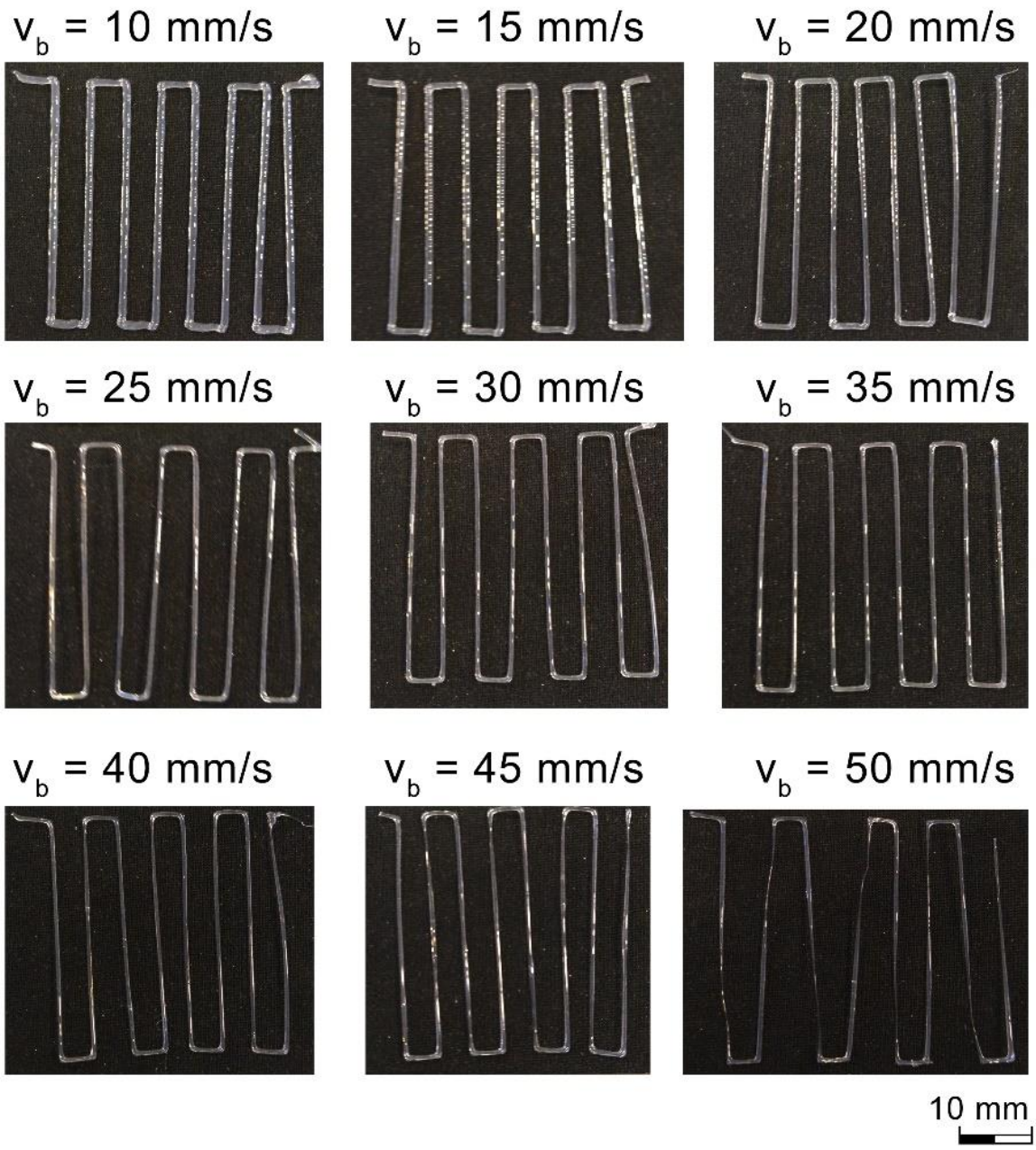


*Source: the author*

As expected, for a given extrusion output the lines become progressively narrower due to the stretching of the melt. Under the conditions tested, 3D printing can be considered feasible for deposition speeds up to 45 mm/s. After that, excessive stretching and the eventual rupture of the roads can occur. The width of the roads was measured at multiple points using the ImageJ software, and the height was measured using an analog micrometer. The influence of the valid deposition speeds on the bead geometry is shown in Fig. 71.

*Figure 71. Influence of the build platform speed on the width and height of the deposited lines*

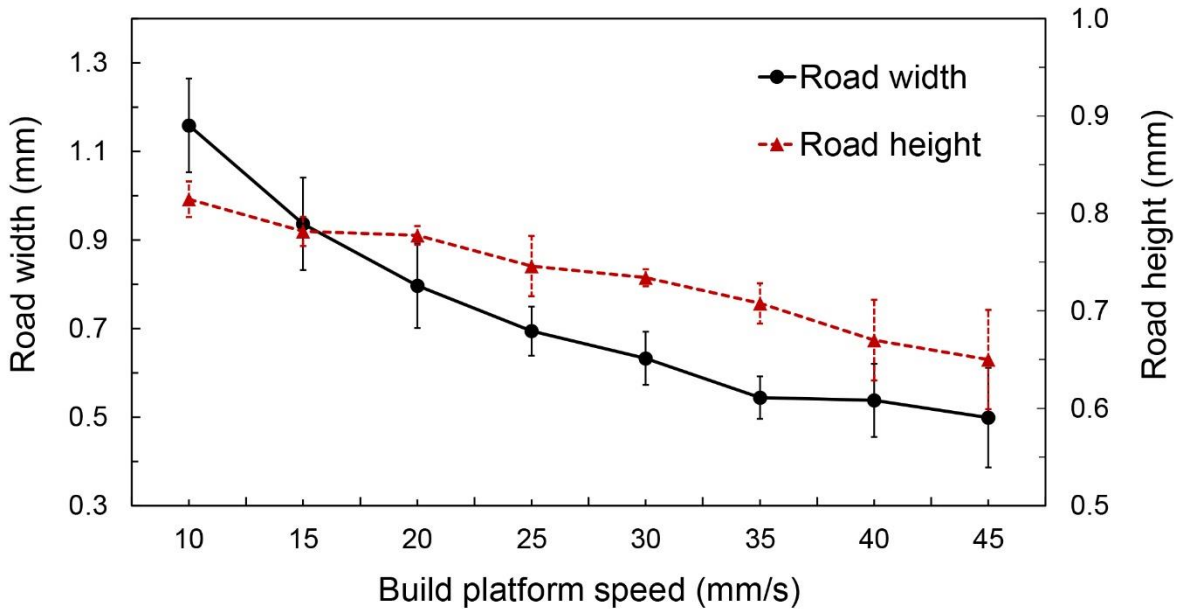


*Source: the author*

3D printing is possible in the whole range of depositions speeds, as long as the printing conditions are adjusted to the measured road width and height. For example, printing at lower speeds requires setting larger line widths, in contrast to the narrower roads obtained at higher speeds. Nonetheless, the measurements show that the deposition is steadier in the range 20–40 mm/s. Outside that range, the printing parameters should be set to compensate for the observed variability, *e.g.* by increasing the overlapping between adjacent roads to avoid unfilled regions.

The data obtained from the line deposition tests were used to set up the 3D printing parameters for two type V tensile test specimens (ASTM D638 [134]) with 90/45º and 90º raster angle, respectively, a square scaffold, and a rectangular box with a spiralized contour (vase mode). The tensile specimens and scaffold were printed with screw 1, while the box was printed with screw 2. In all cases, the screw speed and feed rate were kept at 80 rpm and 20 g/h, respectively. The platform speed was set to 20 mm/s for all parts, with the exception of the walls of the box, which were printed at 15 mm/s. All parts were printed with a line width set to 0.8 mm. The layer height was 0.6 mm for the tensile specimens, and 0.4 mm for the scaffold and box. During printing of the latter, a few particles of red and yellow PP masterbatches were added to the PP at different times, to obtain a multicoloured pattern, and to demonstrate the mixing capability of the extruder. The printed parts (Fig. 72) exhibited the quality expected from this 3D printing technique.

*Figure 72. 3D printed PP structures: (a) 90º/45º tensile specimen, (b) 90º tensile specimen, c) scaffold, d) box with a coloured pattern.*

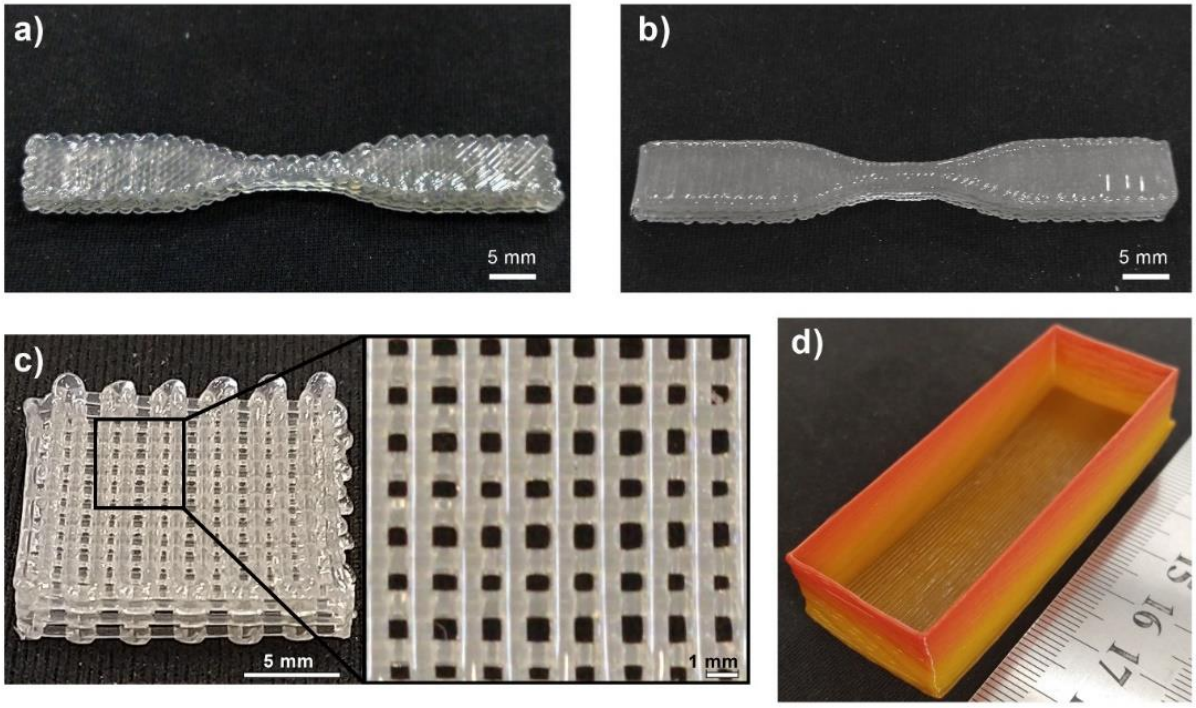


*Source: the author*

As shown in Fig. 71, for the 20 g/h output and using a 0.6 mm diameter nozzle, the width and height of the lines deposited at 45 mm/s can reach 0.49 ± 0.11 mm and 0.66 ± 0.05 mm, respectively. Similar to any other MEX system, the geometry of the deposited lines (*i.e.* road width and height) results from the interplay between output and printing parameters (*e.g.* build platform speed, nozzle diameter, and standoff distance). Therefore, by changing the nozzle diameter, finer strands can be obtained. This is demonstrated in Fig. 73, which compares the diameter of the extruded filament and the aspect of a scaffold generated with a 0.6 mm nozzle (same as in Fig. 72), and a 0.4 mm nozzle. The scaffold shown in Fig. 73b was printed with 0.4 mm raster width and 0.2 mm layer height, at 65 mm/s and 20 g/h output.

*Figure 73. Comparison of the extrudate diameter and achievable strand fineness with a a) 0.6 mm bozzle and b) a 0.4 mm nozzle.*

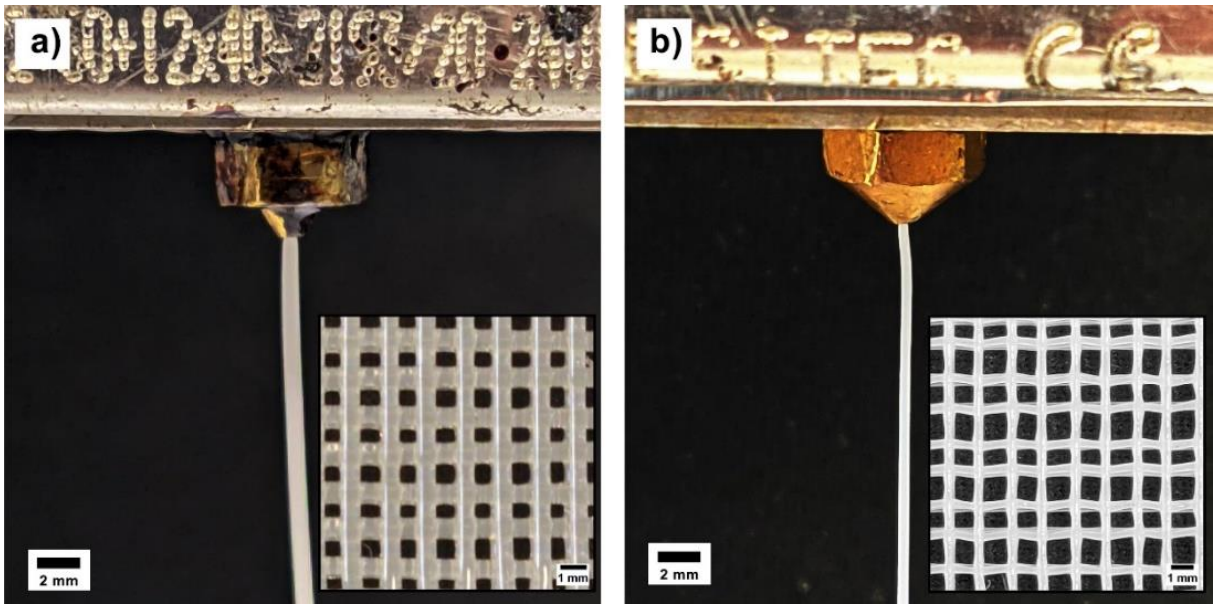


*Source: the author*

Uniaxial type V tensile specimens (with 90º raster angle) were 3D printed from the PP/PS 90/10 blend and the neat PP micro-pellets, using screw configuration 1 at 80 rpm and 20 g/h output (see Fig. 74). The barrel temperature was set to 180 ºC and 210 ºC for the first and second heating zones, respectively. The specimens were printed in the YX orientation (ASTM F2971–13 [135]). A 0.6 mm nozzle was used to print at 20 mm/s with 0.8 mm raster width, and 0.6 mm layer height (100 % infill).

*Figure 74. 3D printed tensile test specimens from a) PP/PS 90/10 blend and b) neat PP.*

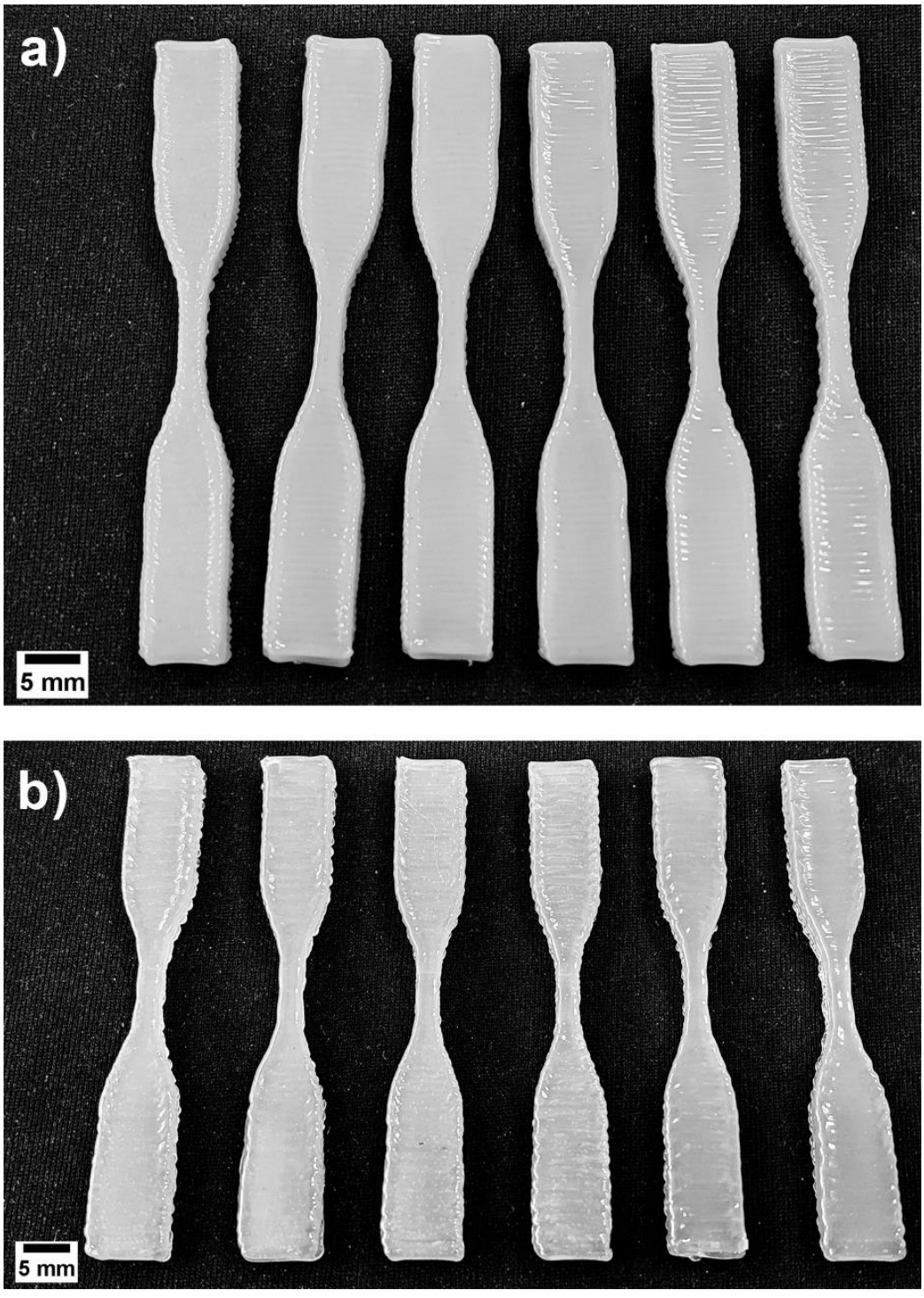


*Source: the author*

Tensile tests were performed on an Instron 5969 universal testing machine, with an initial gauge length of 30 mm, at 10 mm/min and room temperature (25 ºC). The measured values for the Young's modulus, ultimate tensile strength (UTS), and elongation at break are depicted in Fig. 75.

*Figure 75. Tensile testing results for PP/PS and PP: a) Young`s modulus, b) ultimate tensile strength, and c) elongation at break.*

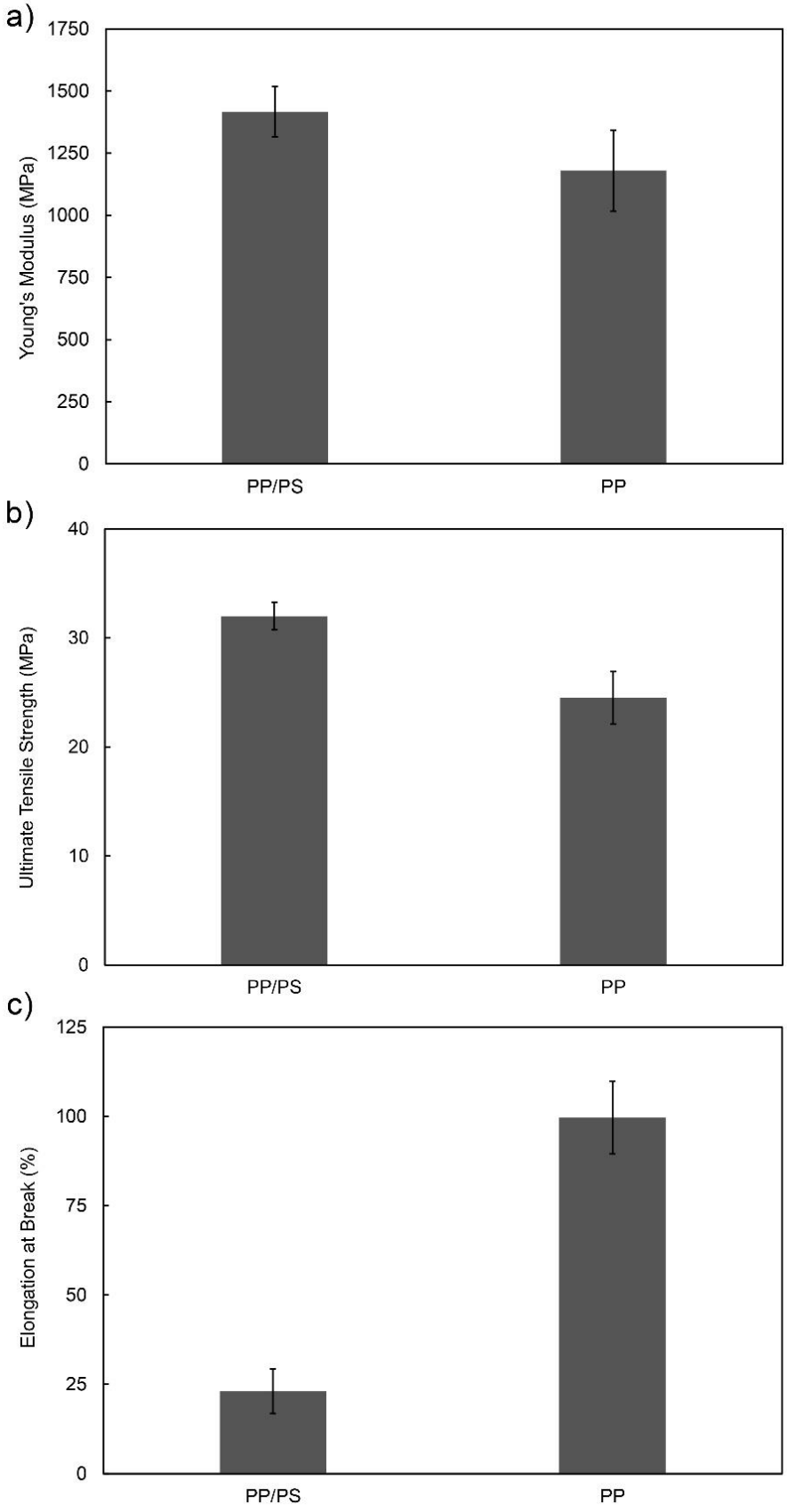


*Source: the author*

The values measured for the modulus and strength of the neat PP specimens (1179 ± 163 MPa and 25 ± 2 MPa, respectively) agree well with those reported by Carneiro et al. [136], who evaluated the mechanical properties of PP bars prepared by FDM. The PP specimens have also shown considerable ductility (100 ± 10 % elongation at break). As expected, the blend specimens showed an increase in the Young's modulus and UTS (1417 ± 101 MPa and 32 ± 1 MPa, respectively), accompanied by a significant decrease in the elongation at break (23 ± 6 %) due to the presence of the PS phase.

# 6 CONCLUSIONS AND FUTURE WORKS

A benchtop material extrusion additive manufacturing equipment based on a co-rotating twin screw extruder was designed and validated. The Co-TSE AM system comprises three major subsystems: the extrusion unit, the drive unit, and the positioning system. The extrusion unit was designed with modular construction for improved geometrical flexibility. It includes a volumetric feeder that enables better control over the thermomechanical environment inside the extruder and reduces the required mechanical power. The design of the drive unit was particularly challenging, given the short distance between the screw shafts. The positioning system is responsible for the motion in the three Cartesian axes, a robust configuration considering the dimensions and inertia of the print head. With the presented embodiment, processing and printing can be performed with up to 75 $cm^3$ of powdered material, without the need to refill the feeder, and the maximum build is 55 × 80 × 43 mm.

Extrusion tests demonstrated that the Co-TSE print head is able to accept materials in powder or micro-pellet form, plasticize and extrude them through the nozzle under steady and controllable flow rate. Since the output and the screw speed are controlled independently, distributive and dispersive mixing intensity and residence time can be varied without affecting the extrusion/deposition rate. Two screw configurations were used, with and without kneading discs, to assess the response of the extrusion unit in terms of flow characteristics and mixing performance. The screw with kneading elements (configuration 1) is particularly effective for mixing/dispersion purposes. In addition, based on the literature, the mixing performance offered by the Co-TSE is expected to be superior to what is achievable with similar-sized single screw extruders developed for 3D printing.

Deposition tests were performed to find the feasible printing conditions, including the deposition speed, road width, and layer height. Since the screw profile and speed did not affect the output, the extrusion conditions were not varied thoroughly. The resulting insights from the initial single layer depositions were used to set the printing conditions for more complex parts. Tensile test specimens, a square scaffold, and a rectangular box with multicolored walls were printed with the expected quality, demonstrating the global feasibility of the design. The specimens were pulled, showing good agreement with the expected results.

The Co-TSE AM system not only eliminates the dependency on filamentary feedstock but combines polymer compounding and 3D printing in a single processing route. This

represents a significant step towards the availability of a more versatile equipment that can be customized according to the required processing tasks and/or intended application. Future research avenues include using this printer to integrate into a single step the manufacture and printing of polymer blends, biocomposites, and bio-nanocomposites for personalised medical applications.

Overall, this thesis addresses the system-level design stage of the development process of an innovative 3D printer. As a typical case of complex system development process, the system-level design is a critical phase in which a pre-defined concept is decomposed into a series of subsystems that can be detailed, tested and validated in parallel to be thereafter integrated, tested and validated as a whole product [137].

Different from the previous product development stages (*i.e.* product planning and concept design), which have relatively well-defined tools and methods, the system-level design usually tackles project-specific challenges that bring together various fields of knowledge and, therefore, lacks specific design tools but follows general rules or principles to fulfil the required functions with a given layout, components and materials [139].

To name a few, the development of the Co-TSE AM system encompassed concepts from machine design, electromechanics, material processing and manufacturing. Thus, similar projects would benefit from a multidisciplinary engineering team to efficiently cope with the following bottlenecks identified for SA-MEX in general:

- Limited torque *versus* speed characteristics of the drive units: most SA-MEX systems are driven by stepper motors only, which work fine for precision positioning but can not offer a good compromise between torque and screw speed for more demanding applications;
- Difficult feeding: material feeding to the screw channels can become quite problematic with the vertical extrusion units. This depends on the characteristics of the material to be processed (*e.g.* granulometry, flowability), as well as on the type of feeding regime (flood feeding or starve feeding). When feeders are used, additional challenges must be overcome to guarantee feed rate regularity and reliability;
- Difficult thermal control: it is difficult to control the temperature of the different functional zones (particularly the feeding zone) with small L/D values. Besides, due to the usually reduce size of the extrusion units, heating by conduction becomes more prominent than viscous heat dissipation which might alter the processing behaviour;

- Need for manufacturing precision: precise fabrication is paramount to the miniature extruders, both from the mechanical and material processing perspective. Even though some designs can be mechanically more forgiving, innapropriate clearances can lead to important alterations on the flow characteristics of the extruder;
- Continuous extrusion: different from filament-fed print heads, interrupting the flow of material is more difficult with SA-MEX. This limits the complexity of the parts that can be 3D printed. Unwanted deposition should be circumvented by imitating filament retraction or developing alternative deposition strategies.

Lastly, the independent treatment given to the main functions of a MEX 3D printer (*i.e.* material dispensing and 3D deposition) has proven adequate to the development of the Co-TSE print head with fewer design constraints, even if some size and weight restrictions were considered to some extent.

Some suggestions for future works:

- Identify the processing limits of the extrusion unit in terms of feed rate and screw speed;
- Determine the feasible build platform speed range for a 0.4 mm nozzle;
- Analyse the performance of the extrusion unit processing materials with different viscosity levels;
- Compare the mixing quality achieved with the Co-TSE print head and a single screw print head under equivalent shearing conditions;
- Perform a benchmark analysis between the Co-TSE AM system and a FFF 3D printer in terms of print quality, speed and mechanical properties;
- Explore the potential applicability of the equipment for polymer recycling and production of personalised medices;
- Design and fabricate alternative conveying elements and/or kneading discs to have more screw configuration options;
- Improve the drive unit to offer higher torque at higher speeds;
- Improve the temperature controls by using dedicated electronics.

## REFERENCES

[1] CHEN, L. et al. The Research Status and Development Trend of Additive Manufacturing Technology, **Int. J. Adv. Manuf. Technol.**, v. 89 (9–12), p. 3651–3660, 2016.

[2] ISO/ASTM. **ASTM 52900:2017-02:** Additive manufacturing - general principles terminology. 2017.

[3] LEARY, M. **Design for additive manufacturing**. Amsterdam: Elsevier, 2020.

[4] NURHUDAN A. I. et al. Additive manufacturing of metallic based on extrusion process: a review, **J Manuf Process.**, v. 66, p. 228–237, 2021.

[5] GIBSON, I. et al. **Additive Manufacturing Technologies**. 3rd ed. Switzerland: Springer Nature, 2021.

[6] GONZALEZ- GUTIERREZ, J. et al. Additive Manufacturing of Metallic and Ceramic Components by Material Extrusion of Highly-Filled Polymers: A Review and Future Perspectives, **Materials**, v. 11 (5), pp. 840, 2018.

[7] ZHANG, P. et al. From materials to devices using fused deposition modeling: A state-of-art review, **Nanotechnol Rev.**, v 9 (1), p. 1594–1609, 2020.

[8] BYARD, D. J. et al. Green fab lab applications of large-area waste polymer-based additive manufacturing, **Addit. Manuf.**, v. 27, p. 515–525, 2019.

[9] REICH, M. J. et al. Mechanical properties and applications of recycled polycarbonate particle material extrusion-based additive manufacturing, **Materials**, v. 12 (10), pp. 1642, 2019.

[10] WANG, C. et al. Design, characterization, and 3D printing of cardiovascular stents with zero poisson's ratio in longitudinal deformation, **Engineering**, v. 7 (7), p. 979–990, 2020.

[11] WIBOW, A. et al. 3D Printing of polycaprolactone–polyaniline electroactive scaffolds for bone tissue engineering, **Materials**, v. 13 (3), pp. 512, 2020.

[12] HUANG, B. et al. Aligned multi-walled carbon nanotubes with nanohydroxyapatite in a 3D printed polycaprolactone scaffold stimulates osteogenic differentiation, **Mater. Sci. Eng. C**, v. 108, pp. 110374, 2020.

[13] TIAN, J. et al. Ding, Additive manufacturing of wood flour/PHA composites using micro-screw extrusion: effect of device and process parameters on performance, **Polymers**, v. 13 (7), pp. 1107, 2021.

[14] VYAS, C. et al. 3D printing of silk microparticle reinforced polycaprolactone scaffolds for tissue engineering applications, **Mater. Sci. Eng. C**, v. 118, pp. 111433, 2021.

[15] LENGAUER, W. et al. Fabrication and properties of extrusion-based 3Dprinted hardmetal and cermet components, **Int. J. Refract Met. Hard Mater.**, v. 82, p. 141–149, 2019.

[16] KIM, H., LEE, S. Printability and physical properties of iron slag powder composites using material extrusion-based 3D printing, **J. Iron Steel Res. Int.**, v. 28, p. 111–121, 2020.

[17] SINGH, G. et al. Additive manufacturing of 17–4 PH steel using metal injection molding feedstock: analysis of 3D extrusion printing, debinding and sintering, **Addit. Manuf.**, v. 47 pp. 102287, 2021.

[18] HE, Q. et al. Additive manufacturing of dense zirconia ceramics by fused deposition modeling via screw extrusion, **J. Eur. Ceram. Soc.**, v. 41 (1), p. 1033–1040, 2021.

[19] GOYANES, A. et al. Direct powder extrusion 3D printing: fabrication of drug products using a novel single-step process, **Int. J. Pharm.**, v. 567, pp. 118471, 2019.

[20] ONG, J. J. et al. 3D printed opioid medicines with alcohol-resistant and abuse-deterrent properties, **Int. J. Pharm.**, v. 579, pp. 119169, 2020.

[21] SAMARO, A. et al. Can filaments, pellets and powder be used as feedstock to produce highly drug-loaded ethylene-vinyl acetate 3D printed tablets using extrusion-based additive manufacturing, **Int. J. Pharm.**, v. 607, pp. 120922, 2021.

[22] RAUWENDAAL, C. **Polymer Extrusion**. 5th ed. Munich: Carl Hanser Verlag, 2014.

[23] BHATTACHARYYA, A. et al. Bioink homogeneity control during 3D bioprinting of multicomponent micro/nanocomposite hydrogel for even tissue regeneration using novel twin screw extrusion system, **Chem. Eng. J.**, v. 415, pp. 128971, 2021.

[24] BAI, H. et al. A new type of 3D printing molding equipment: overall structural design and the numerical simulation for the flow field characteristics of its screw module, **Int. J. Precis. Eng. Manuf.**, v. 22, p. 1639–1656, 2021.

[25] TEIXEIRA, C., GASPAR-CUNHA, A., COVAS, J. A. Flow and heat transfer along the length of a co-rotating twin screw extruder, **Polym.-Plast. Technol. Eng.**, v. 51 (15), p. 1567–1577, 2012.

[26] GOGOS, C. G., TADMOR, Z. **Principles of polymer processing**. John Wiley & Sons, 2013.

[27] FRANCIS, L. **Materials processing: a unified approach to processing of metals, ceramics and polymers**. Academic Press, 2015.

[28] THOMAS, S., WEIMIN, Y. **Advances in polymer processing: from macro to nano scales**. CRC Press, 2009.

[29] BAIRD, D. G., COLLIAS, D. I. **Polymer processing: principles and design**. 2nd. Ed. John Wiley & Sons Inc., 2014.

[30] DAE HAN, C. **Rheology and processing of polymeric materials: volume 2 polymer processing**. Oxford University Press, 2007.

[31] DAE HAN, C. **Rheology and processing of polymeric materials: volume 1 polymer rheology**. Oxford University Press, 2007.

[32] MORRISON, F.A. **Understanding rheology**. Oxford University Press, 2001.

[33] HARNBY, N., EDWARDS, M. F., NIENOW, A.W. **Mixing in the process industries**. 2nd ed. Woburn: Butterworth Heinemann, 1997.

[34] STEVENS, M. J., COVAS, J. A**. Extruder principles and operation**. 2nd ed. Springer-Science, 1995.

[35] KOHLGRÜBER, K. **Co-rotating twin-screw extruders: fundamentals**. Munich: Carl Hanser Verlag, 2020.

[36] OSSWALD, T. A., HERNÁNDEZ-ORTIZ, J. P. **Polymer processing: modelling and simulation**. Munich: Carl Hanser Verlag, 2006.

[37] KOHLGRÜBER, K. **Co-rotating twin-screw extruders: fundamentals, technology, and applications**. Munich: Carl Hanser Verlag, 2007.

[38] LIMPER, A. **Mixing of rubber compounds**. Munich: Carl Hanser Verlag, 2007.

[39] THOMAS, S., GROHENS, Y., JYOTISHKUMAR, P. **Characterization of polymer blends: miscibility, morphology and interfaces**.Weinheim: Wiley-VCH Verlag, 2015.

[40] POTENTE, H., ANSAHL, J., KLARHOLZ, B. Design of tightly intermeshing co-rotating twin screw extruders, **International Polymer Processing**, v. 9 (1), p. 11-25, 1994.

[41] GILES, H. F. J.; WAGNER, J. R. J.; MOUNT, E. M. **Extrusion: the definitive processing guide and handbook**. New York: William Andrew, 2004.

[42] WANG, N. H., SAKAI, T., HASHIMOTO, N. Modeling of polymer devolatilization in a multi-vent screw extruder, **Intern. Polymer Processing**, v. X (4), 1995.

[43] EITZLMAYR, A. et al. Mechanistic modeling of modular co-rotating twin-screw extruders, **Intern. Journal of Pharmaceutics**, v. 474, p. 157-176, 2014.

[44] JUNG, H., WHITE, J. L. Investigation of melting phenomena in modular co-rotating twin screw extrusion, **Intern Polymer Processing**, v. 18 (2), p. 127-132, 2003.

[45] DAMINABO, S. C. et al. Fused deposition modeling-based additive manufacturing (3D printing): techniques for polymer material systems, **Materials Today Chemistry**, v. 16, pp. 100248, 2020.

[46] CRUMP, S. S. **Apparatus and method for creating threedimensional objects**. US5121329. Filled 30 Oct. 1989, Granted 9 Jun 1992.

[47] BOULAALA, M. et al. Towards design of mechanical part and electronic control of multi-material/multicolor fused deposition modeling 3D printing, **Intern. Journal of Advanced Manufacturing Technology**, v. 110, p. 45-55, 2020.

[48] CHAUNIER, L. et al. Material extrusion of plant biopolymers: Opportunities & challenges for 3D printing, **Additive Manufacturing**, v. 21, p. 220-233, 2018.

[49] DUTY, C. et al. What makes a material printable? A viscoelastic model for extrusion-based 3D printing of polymers, **Journal of Manufacturing Processes**, v. 35, p. 526-537, 2018.

[50] KUMAR, N. et al. The effect of process parameters on tensile behavior of 3D printed flexible parts of ethylene vinyl acetate (EVA), **J Manuf Process**, v. 35, p. 317–326, 2018

[51] SIEMIŃSKI, P. Introduction to fused deposition modeling. In: POU, J. , RIVEIRO, A., DAVIM, J. P. (Ed.), **Handbooks in Advanced Manufacturing**, Additive Manufacturing, Elsevier, 2021, p. 217-275.

[52] REPRAP. G-code. https://reprap.org/wiki/G-code. Acessed 10/15/2022.

[53] CZYŻEWSKI, P. et al. Influence of Extruder's Nozzle Diameter on the Improvement of Functional Properties of 3D-Printed PLA Products, **Polymers**, v. 14, pp. 356, 2022.

[54] RAVI, P. Understanding the relationship between slicing and measured fill density in material extrusion 3D printing towards precision porosity constructs for biomedical and pharmaceutical applications, **3D Print Med.**, v.6 (10), 2020.

[55] GOH, G. D. et al. Process-Structure-Properties in Polymer Additive Manufacturing via Material Extrusion: A Review, **Critical Reviews in Solid State and Materials Sciences**, v. 45 (2), p. 113-133, 2020.

[56] ROSCHLI, A. et al. Designing for Big Area Additive Manufacturing, **Addit Manuf.**, v. 25, p. 275–285, 2019.

[57] CANO-VICENT, A. et al. Fused deposition modelling: Current status, methodology, applications and future prospects, **Additive Manufacturing**, v. 47, pp. 102378, 2021.

[58] KAMPKER, A. et al. Review on Machine Designs of Material Extrusion based Additive Manufacturing (AM) Systems - Status-Quo and Potential Analysis for Future AM Systems, **Procedia CIRP**, v. 81, p. 815-819, 2019.

[59] PEARCE, J. M. **Open-source lab: how to build your own hardware and reduce research costs**. Amsterdam: Elsevier, 2014.

[60] LA GALA, A. et al. Theoretical Evaluation of the Melting Efficiency for the Single-Screw Micro-Extrusion Process: The Case of 3D Printing of ABS, **Processes**, v. 8, pp. 1522, 2020.

[61] SIDDAWAY, A. P.,WOOD, A. M., HEDGES, L. V. How to do a systematic review: a best practice guide for conducting and reporting narrative reviews, meta-analyses, and meta-syntheses, **Annu Rev Psychol.**, v. 70 (1), p. 747–770, 2018.

[62] BELLINI, A. **Fused deposition of ceramics: a comprehensive experimental, analytical and omputational study of material behavior, fabrication process and equipment design**. 2002. PhD thesis, Drexel University, USA, 2002.

[63] WANG, F. et al. Precision extruding deposition and characterization of cellular poly-ε-caprolactone tissue scaffolds, **Rapid Prototyp J.**, v. 10 (1), p. 42–49, 2004.

[64] BELLINI, A., SHOR, L., GUÇERI, S. I. New developments in fused deposition modeling of ceramics, **Rapid Prototyp J.**, v. 11 (4), p. 214–220, 2005.

[65] REDDY, B. V., REDDY, N. V., GHOSH, A. Fused deposition modelling using direct extrusion, **Virtual Phys Prototyp.**, v. 2 (1), p. 51–60, 2007.

[66] LAM, C. X. F. et al. Mechanical and in vitro evaluations of composite PLDLLA/TCP scaffolds for bone engineering, **Virtual Phys Prototyp.**, v. 3 (4), p. 193–197, 2008.

[67] SILVEIRA, Z. C. et al. Design development and functional validation of an interchangeable head based on mini screw extrusion applied in an experimental desktop 3-D printer, **Int J Rapid Manuf.**, v. 4 (1), p. 49–65, 2014.

[68] DÁVILA, J. L. et al. Fabrication of PCL/β-TCP scaffolds by 3D mini-screw extrusion printing, **J Appl Polym Sci.**, v. 133 (15), pp. 43031, 2016.

[69] ANNONI, M., GIBERTI, H., STRANO, M. Feasibility study of an extrusion-based direct metal additive manufacturing technique, **Procedia Manuf.**, v.5, p. 916–927, 2016.

[70] CANESSA, E., BARUZZO, M., FONDA, C. Study of Moineau-based pumps for the volumetric extrusion of pellets, **Addit Manuf.**, v. 17, p. 143–150, 2017.

[71] LIU, F., HINDUJA, S., BARTOLO, P. Design, fabrication and initial evaluation of a novel hybrid system for tissue engineering applications, **Proc CIRP.**, v. 65, p. 213–218, 2017.

[72] LIU, F. et al. A plasma-assisted bioextrusion system for tissue engineering, **CIRP Ann.**, v. 67 (1), p. 229–232, 2018.

[73] LIU, F. et al. Process-driven microstructure control in melt-extrusion-based 3D printing for tailorable mechanical properties in a polycaprolactone filament, **Macromol Mater Eng.**, v. 303 (8), pp. 1800173, 2018.

[74] LIU, F. et al. Structural evolution of PCL during melt extrusion 3D printing, **Macromol Mater Eng.**, v. 303 (2), pp. 1700494, 2018.

[75] LIU, F., HINDUJA, S., BARTOLO, P.J. User interface tool for a novel plasma-assisted bio-additive extrusion system, **Rapid Prototyp J.**, v. 24 (2), p. 368–378, 2018.

[76] JACKSON, R. J.,WOJCIK, A., MIODOWNIK, M. 3Dprinting of asphalt and its effect on mechanical properties, **Mater Des.**, v. 160, p. 468–474, 2018.

[77] KUMAR, N. et al. Investigation on the effects of process parameters in CNC assisted pellet based fused layer modeling process, **J Manuf Process.**, v. 35, p. 428–436, 2018.

[78] KUMAR, N. et al. Extrusion-based additive manufacturing process for producing flexible parts, **J Braz Soc Mech Sci Eng.**, v. 40 (3), pp. 143, 2018.

[79] KUMAR, N. et al. Experimental investigations on suitability of polypropylene (PP) and ethylene vinyl acetate (EVA) in additive manufacturing, **Mater Today Proc.**, v. 5 (2), p. 4118–4127, 2018.

[80] KUMAR, N. et al. 3D printing of flexible parts using eva material, **Mater Phys Mech.**, v. 37 (2), p. 124–132, 2018.

[81] KUMAR, N. et al. Investigations on the melt flow behaviour of aluminiumfilled ABS polymer composite for the extrusion-based additive manufacturing process, **Int J Mater Prod Technol.**, v. 59 (3), p. 194–211, 2019.

[82] KUMAR, N., JAIN, P. K. Analysing the influence of raster angle, layer thickness and infill rate on the compressive behaviour of EVA through CNC-assisted fused layer modelling process, **Proc Inst Mech Eng Part C: J Mech Eng Sci**, v. 235 (10), p. 1731-1740, 2019.

[83] SINGAMNENI, S. et al. Extrusion 3D printing of polybutyrate-adipate-terephthalate-polymer composites in the pellet form, **Polymers**, v. 10 (8), pp. 922, 2018.

[84] SINGAMNENI, S. et al. Biopolymer alternatives in pellet form for 3D printing by extrusion. **3D Print Addit Manuf.**, v. 6 (4), p. 217–226, 2018.

[85] TSENG, J. W. et al. Screw extrusion-based additive manufacturing of PEEK, **Mater Des.**, v. 140, p. 209–221, 2018.

[86] WHYMAN, S., ARIF, K. M., POTGIETER, J. Design and development of an extrusion systemfor 3D printing biopolymer pellets., **Int J Adv Manuf Technol.**, v. 96, p. 3417–3428, 2018.

[87] HARRIS, M. et al. Acrylonitrile butadiene styrene and polypropylene blend with enhanced thermal and mechanical properties for fused filament fabrication, **Materials**, v. 12 (24), pp. 4167, 2019.

[88] ZHOU, Z. et al. Additive manufacturing of heat-sensitive polymer melt using a pellet-fed material extrusion, **Addit Manuf.**, v. 24, p. 552–559, 2018.

[89] BOYLE, B. M. et al. 3D printing using powder melt extrusion, **Addit Manuf.**, v. 29., pp. 100811, 2019.

[90] LENG, J. et al. The development of a conical screw-based extrusion deposition system and its application in fused deposition modeling with thermoplastic polyurethane, **Rapid Prototyp J.**, v. 26 (2), p. 409–417, 2019.

[91] KHONDOKER, M. A. H, SAMEOTO, D. Direct coupling of fixed screw extruders using flexible heated hoses for FDM printing of extremely soft thermoplastic elastomers, **Prog Addit Manuf.**, v. 4 (3), p. 197–209, 2019.

[92] ALEXANDRE, A. et al. Mechanical properties of direct waste printing of polylactic acid with universal pellets extruder: comparison to fused filament fabrication on open-source desktop three-dimensional printers, **3D Print Addit Manuf.**, v. 7 (5), p. 237–247, 2020.

[93] LIU, T. et al. High-pressure interfacial impregnation by micro-screw in-situ extrusion for 3D printed continuous carbon fiber reinforced nylon composites, **Compos Part A Appl Sci Manuf.**, v. 130, pp. 105770, 2020.

[94] WANG, W. et al. Morphological, mechanical and biological assessment of PCL/pristine graphene scaffolds for bone regeneration, **Int J Bioprint.**, v.2 (2), p. 95–104, 2016.

[95] WANG, W. et al. Enhancing the hydrophilicity and cell attachment of 3D printed PCL/graphene scaffolds for bone tissue engineering, **Materials**, v. 9 (12), p. 1–11, 2016.

[96] HUANG, B. et al. Polymer-ceramic composite scaffolds: the effect of hydroxyapatite and β-tri-calcium phosphate, **Materials**, v. 11 (1), pp. 129., 2018.

[97] GEOFFROY, L. et al. Additivemanufacturing of fire-retardant ethylene-vinyl acetate, **Polym Adv Technol.**, v. 30 (7), p. 1878–1890, 2019.

[98] HERTLE, S., DREXLER, M., DRUMMER, D. Additive manufacturing ofpoly(propylene) by means of melt extrusion, **Macromol Mater Eng.**, v. 301 (12), p. 1482–1493, 2016.

[99] HERTLE, S. et al. Production of polymer-metal hybrids using extrusion-based additive manufacturing and electrochemically treated aluminum, **Addit Manuf.**, v. 33, pp. 101135, 2020.

[100] BROOKS, B. J. et al. Robot-assisted3D printing of biopolymer thin shells, **Int J Adv Manuf Technol.**, v. 89, p. 957–968, 2017.

[101] LIU, X. et al. A large-scale double-stage-screw 3D printer for fused deposition of plastic pellets, **J Appl Polym Sci.**, v. 134 (31), pp. 45147, 2017.

[102] MAGNONI, P. et al. Robotic AM System for Plastic Materials: Tuning and On-line Adjustment of Process Parameters, **Procedia Manuf.**, v. 11, p. 346–354, 2017.

[103] REBAIOLI, L. et al. Process parameters tuning and online re-slicing for robotized additive manufacturing of big plastic objects, **Robot Comput Integr Manuf.**, v. 55 (A), p. 55–64, 2019.

[104] SCHMIDT, L. et al. Characterization of a granulate-based strand deposition process in the FLM-method for definition of material-dependent process strategies, **Rapid Prototyp J.**, v. 25 (1), p. 104–116, 2018.

[105] DUTY, C. E. et al. Structure and mechanical behavior of BigArea Additive Manufacturing (BAAM) materials, **Rapid Prototyp J.**, v. 23 (1), p. 181–189, 2017.

[106] COMPTON, B. et al. Thermal analysis of additive manufacturing of large-scale thermoplastic polymer composites, **Addit Manuf.**, v. 17, p. 77–86, 2017.

[107] AJINJERU, C. et al. Rheological survey of carbon fiberreinforced high-temperature thermoplastics for big area additive manufacturing tooling applications, **J Thermoplast Compos Mater.**, 2019.

[108] BILLAH, K. M. M. et al. Thermomechanical characterization of short carbon fiber and short glass fiber-reinforced ABS used in large format additive manufacturing, **Addit Manuf.**, v. 35, pp. 101299, 2020.

[109] MERAZ TREJO, E. et al. Compressive deformation analysis of large area pellet-fed material extrusion 3D printed parts in relation to in situ thermal imaging, **Addit Manuf.**, v. 33, pp. 101099, 2020.

[110] YEOLE, P. et al. Mechanical characterization of high-temperature carbon fiber-polyphenylene sulfide composites for large area extrusion deposition additive manufacturing, **Addit Manuf.**, v. 34, pp. 101255, 2020.

[111] WOERN, A. L. et al. Fused particle fabrication 3-D printing: recycled materials' optimization and mechanical properties, **Materials**, v. 11 (8), pp. 1413, 2018.

[112] DERTINGER, S. C. et al. Technical pathways for distributed recycling of polymer composites for distributed manufacturing: windshield wiper blades, **Resour Conserv Recycl.**, v. 157, pp. 104810, 2020.

[113] LITTLE, H. A. et al. Towards distributed recycling with additive manufacturing of PET flake feedstocks, **Materials**, v. 13 (19), pp. 4273, 2020.

[114] MORENO NIETO, D., LÓPEZ, V. C., MOLINA, S. I. Large-format polymeric pellet-based additive manufacturing for the naval industry, **Addit Manuf.**, v. 23, p. 79–85, 2018.

[115] FERRARI, A. et al. Additive bio-manufacturing: 3D printing for medical recovery and human enhancement, **STOA European Parliament**, PE614.571, 2018.

[116] MALONE, E., LIPSON, H. Fab@Home: the personal desktop fabricator kit, **Rapid Prototyp J**., v. 13 (4), p. 245–255, 2007.

[117] RANE, K., STRANO, M. A comprehensive review of extrusionbased additive manufacturing processes for rapid production of metallic and ceramic parts, **Adv Manuf.**, v. 7, p. 155–173, 2019.

[118] ANIWAA. RegenHU 3DDiscovery review. https://www.aniwaa.com/product/3d-printers/regenhu-3ddiscovery/. 2021. Accessed 16 Oct 2022.

[119] ANIWAA. Pollen AM Pam review. https://www.aniwaa.com/product/3d-printers/pollen-pam/. 2021. Accessed 16 Oct 2022.

[120] FABRX. FabRx's pharmaceutical 3D printer for personalised medicines, M3DIMAKER™, is now available! https://www.fabrx.co.uk/2020/04/06/fabrxs-pharmaceutical-3d-printer-forpersonalised-medicines-m3dimaker-is-now-available/. 2021. Accessed 16 Oct 2022.

[121] ANIWAA. AIM3D Exam255 review. https://www.aniwaa.com/product/3d-printers/aim3d-exam-255/. 2021. Accessed 16 Oct 2022.

[122] E-CI. BAAM – Big Area Additive Manufacturing. https://www.e-ci.com/baam. 2021. Accessed 16 Oct 2022.

[123] ANIWAA. CNC Barcenas Super Discovery review. https://www.aniwaa.com/product/3d-printers/cnc-barcenas-superdiscovery/. 2021. Accessed 16 Oct 2022.

[124] INFORÇATTI NETO, P. **Estudo da viabilidade técnica e projeto de um mini-cabeçote de extrusão com rosca para impressoras tridimensionais portáteis**. 2013. Dissertação (Engenharia Mecânica) – Escola de Engenharia de São Carlos, Universidade de São Paulo, 2013.

[125] JUSTINO NETTO, J. M. **Projeto de uma miniextrusora dupla rosca corrotativa vertical para aplicação em Manufatura Aditiva.** 2017. Dissertação (Engenharia Mecânica) – Escola de Engenharia de São Carlos, Universidade de São Paulo, 2017.

[126] SPIVAKOVSKY, A., DYACHKOV, V. **Conveyors and related equipment**. Moscow: Peace Publishers, 1966.

[127] VERGNES, B. Average shear rates in the screw elements of a corotating twin-screw extruder, **Polymers**, v.13, pp. 304, 2021.

[128] MICHAELI, W. **Extrusion dies for plastics and rubber**. 3rd ed. Munich: Hanser Publications, 2003.

[129] MOTT, R. L., VAVREK, E. M., WANG, J. **Machine Elements in Mechanical Design**. 6th ed. New York: Pearson, 2018.

[130] ITO, M. M. **Calibração do sistema de acionamento para um cabeçote intercambiável de extrusão vertical baseado em monorrosca**. 2020. Monografia (Engenharia Elétrica) – Escola de Engenharia de São Carlos, Universidade de São Paulo, 2020.

[131] COREXY. https://corexy.com/theory.html. Acessed 16 Oct 2022.

[132] CARNEIRO, O. S. et al. On-line monitoring of the residence time distribution along a kneading block of a twin-screw extruder, **Polym. Test.**, v. 23, p. 925–937, 2004.

[133] CANTO, L. B. On the coarsening of the phase morphology of PP/EVA blends during compounding in a twin screw extruder, **Polym. Test.**, v. 34, p. 175–182, 2014.

[134] ISO/ASTM. **ASTM D638-14:** Standard test method for tensile properties of plastics. 2014.

[135] ISO/ASTM. **ASTM F2971-13:** Standard practice for reporting data for test specimens prepared by Additive Manufacturing. 2013.

[136] CARNEIRO, O. S., SILVA, A. F., GOMES, R. Fused deposition modeling with polypropylene, **Mater. Des.**, v. 83, p. 768–776, 2015.

[137] ULRICH, K. T., EPPINGER, S. D. **Product Design and Development**. 5th . Irwin/McGraw-Hill, 2011.

[138] PAHL, G. et al. **Engineering Design**. 3rd ed. London: Springer-Verlag, 2007.

## APPENDIX A – MatLab script for the planar offset clearance method

```
clear all ;
close all ;
clc ;
syms RE KBO T A x ;
Y = -RE*cos(2*pi*(x - (KBO/2))/T) + sqrt ((A.^2) - (RE.^2)*(sin(2*pi*(x - (KBO/2))/T)).^2 ) ;
Q = diff (Y,x) ;
DG = input ('DG = ') ;
Z = input ('Z = ') ;
A = input ('A = ') ;
T = input ('T = ') ;
s = input ('s = ') ;
d = input ('delta = ') ;
DA = DG - 2*d ;
RA = DA/ 2 ;
DK = 2*A - DA - 2*s ;
RK = DK/2 ;
DE = DA + s ;
RE = DE/ 2 ;
DI = 2*A - DE;
RI = DI/2 ;
FWO = 2* acosd (A/DE) ;
KWO = 180/Z - FWO;
NW = KWO;
KBO = KWO/(2*pi*T) ;
        if (A/DE) < cos (pi/(2*Z))
        DG = input ('DG = ') ;
        A = input ('A = ') ;
        s = input ('s = ') ;
        d = input ('delta = ') ;
else
p = (((T/4) - (KBO/2)) - (KBO/2) )/151;
```

```
32  x = (KBO/2 + p : p : ((T/4) - (KBO/2)) - p) ;
33  y = eval (Q) ;
34  Y = eval (Y) ;
35  plot (x ,Y) ;
36  hold ;
37  xa = x + ((s /2)*(y/sqrt((y.^2)+1))) ;
38  ya = Y - ((s/2)*(y/sqrt((y.^2)+1))) ;
39  plot (xa,ya) ;
40  end
41  yak = Y(1,length(Y)) - ((s/2)*(y(1,length(y))/sqrt((y(1,length(y)).^2)+1))) ;
42  xak = x(1,length(x)) + ((s/2)*(y(1,length(y))/sqrt((y(1,length(y)).^2)+1))) ;
43  KB1 = (T/Z) - 2*xak ;
44  if KB1 < 0
45          msgbox ('ERRO no filete')
46  e l s e
47  KW1 = KB1*(2*pi*T)
48  msgbox ('Perfil criado com sucesso !')
49  FW1 = (180/Z) - ((NW+KW1) /2) ;
50  End
```

# APPENDIX B – Arduino IDE code for the extruder motors

```
1  #include "PWM.h"
2  // no uno os pinos sao: STEP 9  DIR 7 STEPa 3
3  #define MICROSTEP 13 //define o pino de alimentacao do MICROSTEP da impressao
4  //#define DIR 3
5  #define STEP 9 //define o pino de pulso do motor das roscas
6  #define DIR 7 //define o pino de pulso do motor das roscas
7  //#define DIRa 2
8  #define STEPa 3 //define o pino de pulso do motor do alimentador
9
10 // Variaveis globais auxiliares
11 float freq;          //frequencia das roscas
12 float freqa;         //frequencia do alimentador
13 float  i;           //contador da frequencia pra aceleracao e desaceleracao
14 float aux = 1333.3;   //salva a frequencia atual das roscas
15 float rpm = 200;      //salva a velocidade das roscas
16 float auxa = 0;       //salva a frequencia atual do alimentador
17 float rpma = 0;       //salva a velocidade do alimentador
18 String cmd_string;    //salva o texto que foi inserido no
19 void ramp(float freq) //funcao de aceleracao e desaceleracao das roscas
20 {
21 if(aux < freq) //acelera as roscas
22 {
23 for(i=aux ; i<=freq ; i+=0.66) //3.33 em 1/2 microstep da precisao de 0,1
24 {
25 SetPinFrequencySafe(STEP,i);   //seta a frequencia das roscas
26 pwmWrite(STEP,128);          //envia o pwm setado pras roscas com 1/2 duty cicle
27 Serial.print("ROSCAS = ");    //escreve na serial
28 Serial.println(i*60/400, 1);  //escreve na serial o valor do rpm pra a frequencia
   instantanea
29 delay(20);                  //delay para controlar a aceleracao e o motor nao perder passo
30 }
31 }
```

```
32  if(aux > freq) //desacelera as roscas
33  {
34  for(i = aux ; i>=freq ; i-=0.66) //3.33 em 1/2 microstep da precisao de 0,1
35  {
36  SetPinFrequencySafe(STEP,i); //seta a frequencia das roscas
37  pwmWrite(STEP,128);          //envia o pwm setado pras roscas com 1/2 duty cicle
38  Serial.print("ROSCAS = ");   //escreve na serial
39  Serial.println(i*60/400, 1);  //escreve na serial o valor do rpm pra a frequencia
    instantanea
40  delay(20);                   //delay para controlar a desaceleracao e o motor nao perder passo
41  }
42  }
43  aux = freq;     //salva a frequncia atual das roscas
44  }
45  void ramp2(float freqa) //funcao de aceleracao e desaceleracao do alimentador
46  {
47  if(auxa < freqa) //acelera o alimentador
48  {
49  for(i=auxa ; i<=freqa ; i+=2.66) //2.66 em 1/16 microstep da precisao de 0,05
50  {
51  SetPinFrequencySafe(STEPa,i);   //seta a frequencia do alimentador
52  pwmWrite(STEPa,128);             //envia o pwm setado pro alimentador com 1/2 duty
    cicle
53  Serial.print("ALIMENTADOR = "); //escreve na serial
54  Serial.println(i*60/3200);       //escreve na serial o valor do rpm pra a frequencia
    instantanea
55  delay(10);                   //delay para controlar a aceleracao e o motor nao perder passo
56  }
57  }
58  if(auxa > freqa)
59  {
60  for(i = auxa ; i>=freqa ; i-=2.66) //2.66 em 1/16 microstep da precisao de 0,05
61  {
62  SetPinFrequencySafe(STEPa,i);   //seta a frequencia do alimentador
```

```
63  pwmWrite(STEPa,128);              //envia o pwm setado pro alimentador com 1/2 duty
    cicle
64  Serial.print("ALIMENTADOR = "); //escreve na serial
65  Serial.println(i*60/3200);        //escreve na serial o valor do rpm pra a frequencia
    instantanea
66  delay(5);                  //delay para controlar a aceleracao e o motor nao perder passo
67  }
68  }
69  auxa = freqa;  //salva a frequencia atual do alimentador
70  }
71  void setup() //funcao de setup das portas e roda 1 vez assim que o arduino e ligado
72  {
73  InitTimersSafe(); //inicializa os timers
74  pinMode(MICROSTEP,OUTPUT);   //seta a porta do MICROSTEP como saida
75  digitalWrite(MICROSTEP,HIGH); //seta 5V na saida do MICROSTEP
76  //SET das portas do Driver
77  pinMode(DIR,OUTPUT);   //seta a porta de dir como saida
78  pinMode(STEP,OUTPUT);    //seta a porta de step do motor das roscas como saida
79  // pinMode(DIRa,OUTPUT);
80  pinMode(STEPa,OUTPUT);    //seta a porta de step do motor do alimentador como
    saida
81  // Definindo os niveis logicos das portas do Driver
82  digitalWrite(DIR,HIGH);    //Direção do motor: HIGH = CW ; LOW = CCW (Mudar
    valor lógico dessa linha) --> depois apertar Ctrl+U para carregar o programa
83  // digitalWrite(DIRa,HIGH);
84  Serial.begin(9600);                //liga a porta serial
85  Serial.println("Inicializando...");    //escreve na serial
86  for(freq=0 ; freq<=1333.3 ; freq+=3.33)  //acelera as roscas ate 200 rpm
87  {
88  SetPinFrequencySafe(STEP,freq);   //seta a frequencia das roscas
89  pwmWrite(STEP,128);              //envia o pwm setado pras roscas com 1/2 duty cicle
90  delay(10);                 //delay para controlar a aceleracao e o motor nao perder passo
91  }
92  Serial.println("Pronto.");    //escreve na serial
```

```
93  }
94  void loop() //funcao de loop que o arduino ira rodar em loop infinitamente apos rodar a setup
95  {
96  if(Serial.available() > 0)   // Verifica e aguarda algum input na Serial
97  {
98  cmd_string = Serial.readString(); //salva o texto escrito na porta serial
99  if ((cmd_string[0] == 'R') || (cmd_string[0] == 'r')) //verifica se a primeira letra escrita na serial e "R" ou "r"
100 {
101 Serial.println("ROSCAS ROSCAS ROSCAS ROSCAS ROSCAS ROSCAS ROSCAS ROSCAS ROSCAS ROSCAS ROSCAS ROSCAS");    //escreve na serial
102 cmd_string.remove(0,1);    //apaga a letra da serial (para sobrar somente os numeros)
103 if(cmd_string.toInt() > 0) //verifica se o valor escrito foi maior que 0
104 {
105 freq = cmd_string.toFloat()*400/60;  // Conversao de valor RPM para frequenica para o Driver em 1/2 microstep
106 ramp(freq);   // Rotina de rampa de aceleração ou desaceleração do motor das roscas
107 }
108 else  //caso o valor escrito foi 0
109 {
110 digitalWrite(STEP, LOW); //seta a porta de pulso para 0V (portanto nao mandando nenhum pulso)
111 aux = 0;              //salva a frequencia pra 0 das roscas
112 freq = 0;
113 }
114 }
115 if ((cmd_string[0] == 'A') || (cmd_string[0] == 'a'))  //verifica se a primeira letra escrita na serial e "A" ou "a"
116 {
117 Serial.println("ALIMENTADOR ALIMENTADOR ALIMENTADOR ALIMENTADOR ALIMENTADOR ALIMENTADOR");    //escreve na serial
```

```
118 cmd_string.remove(0,1);    //apaga a letra da serial (para sobrar somente os numeros)
119 if(cmd_string.toInt() > 0) //verifica se o valor escrito foi maior que 0
120 {
121 freqa = cmd_string.toFloat()*3200/60;        // Conversão de valor RPM para frequenica
    para o Driver
122 ramp2(freqa);          // Rotina de rampa de aceleração ou desaceleração do motor
123 }
124 else   //caso o valor escrito foi 0
125 {
126 digitalWrite(STEPa, LOW);  //seta a porta de pulso para 0V (portanto nao mandando
    nenhum pulso)
127 auxa = 0;                 //salva a frequencia pra 0 do alimentador
128 freqa = 0;
129 }
130 }
131 }
132 rpm = freq*60/400; //calcula o rpm das roscas
133 rpma = freqa*60/3200; //calcula o rpm do alimentador
134 Serial.print("ROSCAS = ");    //escreve na serial
135 Serial.print(rpm, 1);        //escreve na serial o rpm das roscas com 1 casa decimal
136 Serial.print("    ALIMENTADOR = ");    //escreve na serial
137 Serial.println(rpma);                //escreve na serial o rpm do alimentador
138 }
```

# APPENDIX C – Differential thermogram and flow curves of the PP RP141

The PP RP141 pellets were subject to differential scanning calorimetry (DSC) using a Q2000 DSC (TA Instruments, Newcastle, UK). The sample (ca. 7 mg) was heated from 25 ºC to 400 ºC at 10 ºC/min. The resulting differential thermogram is shown in Fig. 76, evidencing the melting temperature of 146.47 ºC.

*Figure 76. Differential thermogram of the PP RP141.*

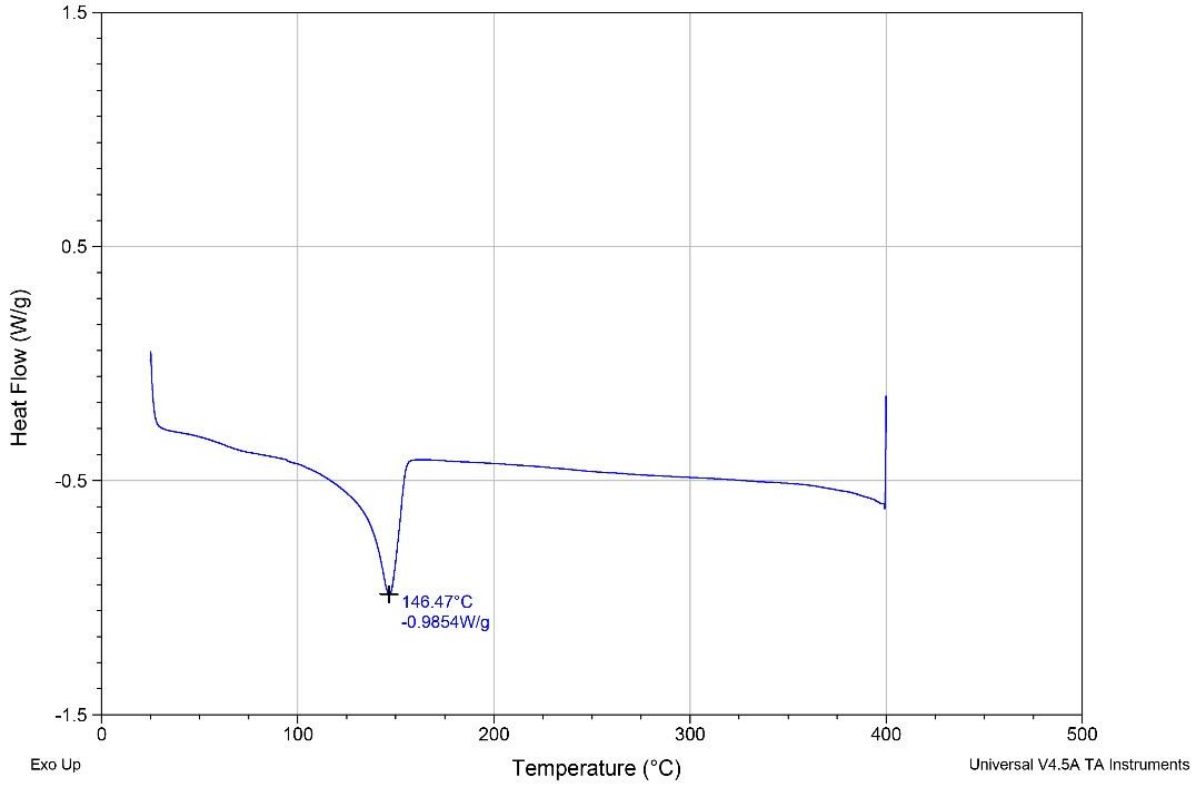


*Source: the author*

The PP RP 141 was also subject to rotational rheometry, using an ARES-G2 rheometer (TA Instruments, Newcastle, UK). The rheometer was equipped with 25 mm diameter parallel plates separated by 1 mm. The imposed shear rate ranged from 1 $s^{-1}$ to 300 $s^{-1}$ at 180, 200 and 220 °C, with $N_2$ purge. Before starting the tests, the samples were kept at the set temperature for 5 minutes. The resulting flow curves are presented in Fig. 77.

*Figure 77. Flow curves for the PP RP 141 at 180, 200 and 220 ºC.*

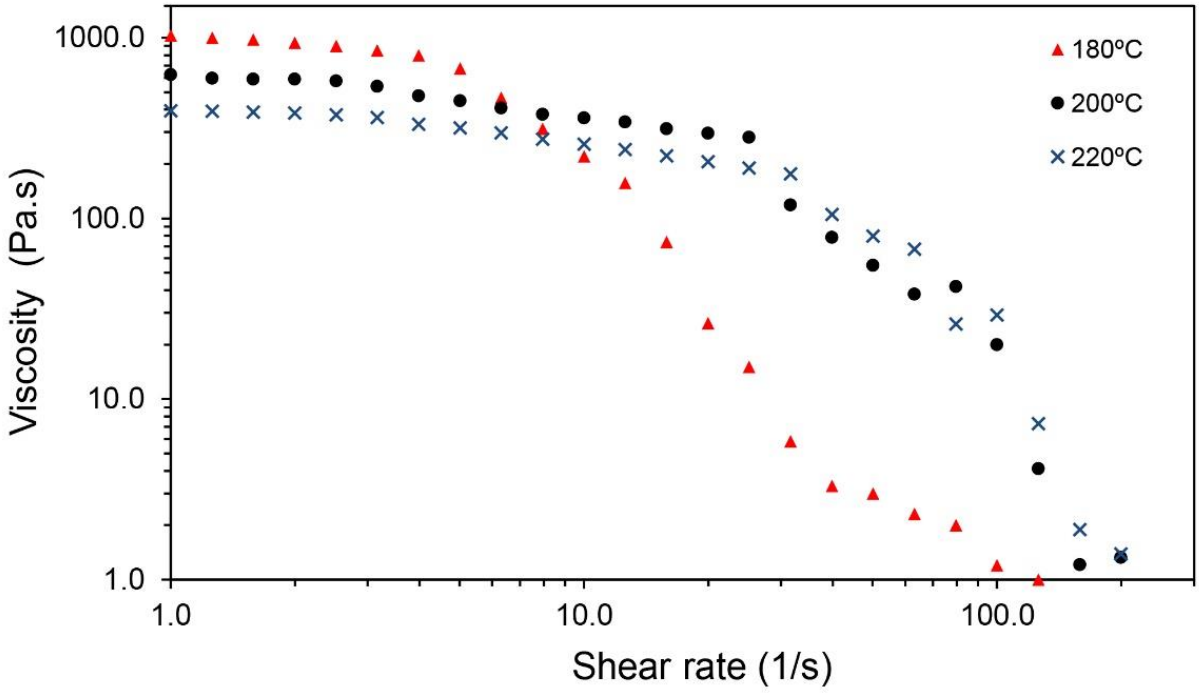


*Source: the author*